Best practices for the analyses of CO_2 fluids by Raman Spectroscopy

Penny E. Wieser[1*], Charlotte L DeVitre[1,2], Isabelle Susman[1]

[1] Earth and Planetary Sciences, University of California, Berkeley, CA 94270, USA

[2] Now at Department of Earth and Environmental Sciences, University of Ottawa, Ottawa, ON K1N 6N5, Canada

*penny_wieser@berkeley.edu

This paper was submitted on the 14th Aug 2025 to Volcanica for review.

This is a non-peer reviewed preprint submitted to EarthArxiv.

Please send any feedback to the lead author!

Abstract

Raman spectroscopy is a key method for determining CO_2 densities in geological fluids, yet acquisition, calibration, and processing methodologies vary widely between laboratories. This study evaluates how these parameters affect precision and accuracy. We show that spectral non-linearity can cause a single instrument to show variable relationships between CO_2 density and spectral parameters as the spectral center and drift correction routine is varied, explaining some of the diversity in published densimeters. We show that when the calibration methodology is applied to unknowns, the Raman method is robust. For example, 240 repeat measurements of a natural fluid inclusion (FI) over ~2 years gives a 1σ variation of only ~0.008 g/cm³. We also assess the influence of variations in sample and room temperature on measurements to help inform analytical strategies. We show that high laser powers in fluid and melt inclusions causes heating of the CO_2 fluid, and unacceptable drops in CO_2 density. We offer practical strategies to optimize signal without raising laser power, noting that small changes in focus and X–Y position greatly affect intensity (but not depth in sample).

1. Introduction

Traditionally, the density of CO_2-rich fluids in geological samples have been measured using Microthermometry, a technique in which phase changes are observed during heating and cooling of trapped inclusions. Starting in the 1930s, it was recognised that CO_2 fluid/gas/vapour has a distinct signal when analysed by Raman spectroscopy, with two strong peaks at ~1285 and ~1388 cm^{-1} (Fermi, 1931; McLennan F.R.S. and Smith M.A., 1932). These peaks are collectively called the Fermi diad. In the 1970s, the distance between the two peaks – referred to as the Fermi diad separation, splitting, peak splitting or diad splitting – was shown to be related to the density of CO_2 (Wright and Wang, 1973). These findings opened up the possibility of using Raman spectroscopy to quantify the density of CO_2 fluids, an important parameter in many geological research questions.

The relationship between diad splitting and CO_2 density on a given Raman instrument is described using a densimeter, which is typically modelled as a polynomial function of Nth degree. A number of groups have developed experimental apparatus to determine densimeters for different instruments (DeVitre et al., 2021; Fall et al., 2011; Kawakami et al., 2003; Lamadrid et al., 2017;

Rosso and Bodnar, 1995; Song et al., 2009; Wang et al., 2019, 2011; Yamamoto and Kagi, 2006). Not only do densimeters vary widely between Raman instruments (e.g. Lamadrid et al. 2017, DeVitre et al. 2021); changes in hardware on a single instrument have also been shown to affect the densimeter. For example, Lamadrid et al. (2017) show that the densimeter on a single instrument can be shifted by changing the laser wavelength (e.g. a ~0.02 g/cm^3 shift from 514 nm to 632 nm at 2400 g) or the instrument grating (e.g., a 0.02-0.04 g/cm^3 shift from 600-2400 g at 632 nm). They conclude that the same wavelength and grating must be used during analysis and calibration.

In contrast, Remigi et al. (2021) investigated offsets between densimeters by generating a calibration using natural fluid inclusion (FI) standards with densities between 0.37-1.08 g/cm^3. They compare their densimeter to published densimeters using bootstrapping techniques to better account for uncertainty in densimeter regressions. They conclude that published Raman densimeters fall into two main categories – those collected on instruments with higher spectral resolution (~0.4 cm^{-1}) and those collected on instruments with lower spectral resolution (~1-1.5 cm^{-1}). For CO_2 densities > 0.3-0.4 g/cm^3, they show that published densimeters within the high- or low-resolution category are within error of each other. Thus, they suggest that published densimeters have wider applicability than previously thought, and instrument-specific calibrations may not be needed.

However, it is worth noting that all the high resolution densimeters they consider were performed on a HORIBA HR instruments, so do not encompass the true variability of Raman hardware. Additionally, they do not consider offsets between densimeters at lower densities (<0.3 g/cm^3). When considering densimeter offsets as a percentage of the CO_2 density, published densimeters differ the most for analyses of gaseous CO_2 at room temperature (ρ~ 0-0.2 g/cm^3; Lamadrid et al. 2017). At these densities offsets can be a factor of 2 or more. This has major implications in volcanology, because many melt inclusion vapor bubbles have CO_2 densities below 0.2 g/cm³ (see Fig. 21 of Wieser et al., 2025). Accurate measurements of vapor bubble CO_2 contents are essential for reconstructing the CO_2 contents of magmas, with implications for determining magma storage depths and the cause of explosive eruptions (Allison et al., 2021; DeVitre et al., 2023b; Moore et al., 2015). Despite this, many recent studies are still measuring CO_2 fluids with low densities using calibrations published in other laboratories (e.g. Howe et al., 2025).

Another recent discussion of the utility of Raman spectroscopy for quantifying CO_2 densities was provided by Bakker (2021). This work assessed the uncertainties associated with various parts of the Raman method (e.g., peak fitting, instrument drift etc) and suggested that errors in the position

of each diad propagate through to very large errors in diad splitting (±0.26-0.27 cm^{-1}) and thus CO_2 density (~±0.1 g/cm^3). This is in contrast to the very low theoretical errors suggested by (Yamamoto and Hagiwara, 2024). Bakker (2021) also suggests that a common method of correcting for instrument drift using the distance between two Ne lines (e.g. Lamadrid et al., 2017) does not fully capture the complex nonlinearity of Raman spectrometers.

Overall, the Bakker (2021) and Remigi et al. (2021) papers demonstrate that while a lot of progress has been made in recent years on optimizing Raman analyses of CO_2 fluids (DeVitre et al., 2023a, 2021; Fall et al., 2011; Lamadrid et al., 2017; Le et al., 2021; Wang et al., 2011), there are still some fundamental questions regarding the factors affecting the densimeter relationship for a single instrument, and the accuracy and precision of the Raman method when applied to natural samples. In this study, we investigate the effect of acquisition and data processing strategies on the precision and accuracy of CO_2 fluid measurements, with the goal of establishing coherent best practices for the broader community.

2. Methods

We acquire Raman spectra on natural FI and melt inclusions (MI) hosted in olivine using a WITec Alpha 300R Raman spectrometer in the Department of Earth and Planetary Science, University of California, Berkeley (hereafter, UCB WITec). We use a green solid-state laser with a wavelength of 532.046 nm, and a Ne lamp in the beam path to correct for instrument drift. For measurements of the CO_2 Fermi diad, the 1800 grooves/mm grating was used, yielding a spectral resolution of 0.57 cm^{-1}. The laser was focused on the sample with a Zeiss 50X objective (x0.55NA, 9.1 mm working distance) or a Zeiss 100X (0.95 Na, 4 mm working distance). This Raman system is equipped with a TruPower module, allowing control of the laser power with an accuracy of ±0.1 mW.

Various methods were used to heat samples above the critical temperature of CO_2 to ensure a single homogenous fluid was being analysed (DeVitre et al., 2023a). For most analyses, samples were placed on a glass slide in crystalbond and placed on a Peltier heating stage with a central hole for transmitted light illumination (Supporting Fig. 1). The target sample temperature was 37 °C, matching the gas cell calibration temperature for this instrument (DeVitre and Wieser, 2024). Temperature was monitored using a type K thermocouple taped to the slide with electrical tape. When tighter temperature control was needed, crystals were double polished and placed in a Linkam THMSG600 stage. To achieve the long working distance required to see through the window, we initially made measurements using a LWD 40X objective with a cover slip correction collar. After doing tests with and without the window, for the wide range of sample temperatures

investigated here (37-70℃), there was no difference in heating series. Thus, later analyses performed them without the window using the Zeiss 50X objective to help increase the strength of signals. We covered the sample with a silver lid with a top hole to enhance uniform heating. All data processing was performed in the open-source Python3 tool DiadFit (Wieser and DeVitre, 2024).

3. Results and Discussion

3.1 Neon lines and spectral nonlinearity

Instrument drift during a Raman session is commonly assessed using repeated analyses of the spectral emission of Neon generated by a Ne lamp (e.g. DeVitre et al., 2021; Lamadrid et al., 2017. Fig. 1a). Two emission lines bracketing the diad are selected. The theoretical distance between these lines is calculated from the published wavelength of the emission spectra of Neon in air from the NIST webbook, converted to wavenumber using the wavelength of the laser used for analysis. This theoretical distance is then compared to the measured distance in the acquired spectra. For example, if the theoretical distance between Ne lines is 330.4776 cm^{-1}, and the measured distance is 331.0587 cm^{-1}, the correction factor is $\frac{\text{Theoretical distance (330.4776)}}{\text{measured distance (331.0587)}} = 0.9982$. If the diad splitting was measured at 103 cm^{-1}, the corrected diad splitting would be 0.9982*103 = 102.8192 cm^{-1}.

Bakker (2021) criticized this method (which they refer to as the 'line segment' technique) because it assumes that the correction factor at any given point between two lines is the same, which is not true if there is any nonlinearity in the spectrometer. Nonlinearity causes different line pairs to yield different correction factors (as noted by Wieser et al. 2021). Bakker (2021) suggest that a 'bracketing technique' should be used instead, where a polynomial model is developed to describe how the position of each Ne line deviates from the theoretical position as a as a function of wavenumber. For brevity, we refer to the lower wavenumber peak of CO_2 as diad 1 (also v- or 2v2), the higher wavenumber peak as diad 2 (also v+ or v_1+2v_2) and the Fermi diad separation as diad splitting. This polynomial allows a correction factor to be calculated for diad 1 and diad 2. These corrected peak positions are used to calculate the splitting, rather than applying a correction factor to the splitting as in the line-segment method.

We investigate spectrometer nonlinearity using three different WITec instruments, and determine the effect of this nonlinearity on instrument drift corrections and calculated CO_2 densities. First, we perform 50 consecutive repeated acquisitions of the emission spectrum of Neon. We fit

pseudovoigt curves to the 6 major Ne lines within the spectral window for each acquisition using DiadFit (565.66588 nm ≈1117 cm^{-1}, 568.98163 nm ≈1220 cm^{-1}, 571.92248 nm≈1310 cm^{-1}, 574.82985 nm≈1399 cm^{-1} 576.44188 nm≈1447 cm^{-1}, and 580.44496 nm≈1567 cm^{-1} for the 532.046 nm laser wavelength used here, Fig. 1a, Kramida and Ralchenko, 1999). For the line at 1117 cm^{-1}, we iteratively fit two pseudovoigt functions to resolve the smaller peak on the shoulder. Fig. 1b shows the fitted Ne line position divided by the theoretical position calculated from the laser wavelength and the theoretical positions in air. This comparison demonstrates that the spectrometer is indeed non-linear, with the correction factor varying across the acquisition window (Fig. 1b).

The polynomial fit through these correction factors is shown for the 'bracketing technique' (grey curve, Fig. 1c) for a single Ne acquisition. Correcting for the position of the CO_2 diad using this curve this would yield a corrected splitting for the diad position shown by blue dotted lines that would be equivalent to a line segment correction factor of 0.9977. The 'line segment' technique for drift correction can be visualized by drawing a straight line between any two datapoints (circles) on this polynomial curve (Fig. 1c). If the gradient of this linear segment is the same as the gradient of a line drawn between where the x positions of the diad intercept the polynomial, the line segment technique and bracketing techniques would give the same result. The line segment method applied to the 1220-1399 cm^{-1} lines results in a very similar correction factor to the bracketing technique (0.9976 vs. 0.9977). The disadvantage of choosing this pair is that the 1220 cm^{-1} line is relatively small, resulting in larger fitting errors, meaning that correction factors show substantially more variability in a given run than using the 1117-1447 cm^{-1} pair (see error bar on Fig. 1c). The 1117-1447 cm^{-1} pair used by our laboratory yields a reasonably similar correction factor to the bracketing technique (0.9982 vs. 0.9977). However, applying the line segment technique to the 1220-1567 cm^{-1} lines (red dashed segment) would result in a Ne correction factor that is far smaller than that determined using the bracketing technique (0.9991 vs. 0.9977), yielding a higher apparent diad splitting ($\Delta_{CO2}^{Corr,brack}$=103.450 cm^{-1} vs. $\Delta_{CO2}^{Corr,seg}$=103.648 cm^{-1}).

The differences in correction factor mean that the choice of Ne line pair affect the corrected splitting, and thus the relationship between CO_2 density and corrected splitting (i.e. the densimeter). To demonstrate this, we take the CO_2 and Neon spectra from the analytical sessions used to calibrate the UCB densimeter. The published UC densimeter was calibrated from corrected splittings calculated using correction factors from the 1117-1447 cm^{-1} Ne line pair (DeVitre et al., 2021; DeVitre and Wieser, 2024, black dotted line, Fig. 2a-b). We reprocess the data using 4 new pairs of Ne lines: ~1220-1447 cm^{-1} (dashed red line, Fig. 2a, c), ~1117-1399 cm^{-}

188 ^{1} (dashed blue line), 1220-1398 cm^{-1} (solid cyan line), and 1220-1567 cm^{-1} (solid magenta line,
189 Fig. 2a-b). Thus, for each CO_2 spectrum, we have one value for the known density of the fluid
190 from the calibration cell, and 5 different corrected splitting values – one for each Ne line pair.
191 Using three polynomial fits, one for low, medium and high densities (following DeVitre et al. 2021),
192 we generate 5 different densimeter equations (Fig. 2a-b). Despite being collected on a single
193 instrument using the same calibration dataset, the densimeters differ by up to ~0.08 g/cm^3 simply
194 based on Ne line pair used for data reduction. To put the magnitude of these offsets into context,
195 we underlay the densimeters collected on a wide variety of Raman instruments (Fall et al., 2011;
196 Kawakami et al., 2003; Lamadrid et al., 2017; Wang et al., 2011, 2011; Yamamoto and Kagi,
197 2006), colored using the high (grey) and low (salmon) resolution classifications from Remigi et al.
198 (2021). The variability from a single instrument introduced through the choice of a Neon line pair
199 is as large as the differences between Raman instruments. It is also noteworthy that despite our
200 instrument having a 'high resolution' spectrometer, all our possible densimeters lie with the low
201 resolution densimeters of Remigi et al. (2021). Table 1 shows that different laboratories use a
202 wide variety of methods to calibrate their spectrometers and subsequently correct them for
203 instrument drift. Thus, we suggest that the choice of drift correction method is likely a major
204 contributor to the wide diversity of densimeters published by different laboratories (see also
205 Bakker, 2021).

206 Table 1- Compilation of studies publishing densimeters, and the methods used to calibrate the
207 spectrometer (which sets the nonlinearity response seen in Fig. 1b) and correct data for drift
208 during a run. n.d. indicates the publication did not say what method was used.

Paper	**Spectrometer Calibration method**	**Drift correction used**
DeVitre et al., 2021; DeVitre and Wieser, 2024	Hg-Ar lamp (atomic emission line)	Ne lamp (lines at 1117 cm^{-1} and 1447 cm^{-1} at 532.046 nm)
Wieser et al., (2021)	Si chip	Repeated FI measurement
Lamadrid et al. (2017)	Laser line and Ne line at 1458.58 cm^{-1}	Ne lamp (lines at 1031.42 cm^{-1} and 1458.58 cm^{-1} for a 514 nm laser)
Fall et al. (2011)	Silicon wafer	n.d. say methods similar to Lin et al. (2007) who use Ne lines

Wang et al. (2019, 2011)	Benzonitrile - (Raman shift standard)	Diamond
Yamamoto and Kagi, (2006)	Napthalene (Raman shift standard)	n.d.
Song et al. (2009)	Diamond	n.d.

These offsets between these densimeters are only problematic if they yield different results when analysing unknowns. We test whether this is the case using data collected on FI from Fogo volcano collected by DeVitre and Wieser (2024), where there are independent constraints on CO_2 density from microthermometry. We process the FI data using each of the 5 different Ne line pairs (Fig. 2b), generating 5 values of corrected splitting for each spectrum, and input these values into the densimeter corresponding to each Ne line pair (e.g. data reduced using correction factors for the 1220-1399 pair was fed into the 1220-1399 densimeter). To visualize the differences between these data reduction strategies, we subtract the density calculated using each line pair from that calculated using the 1117-1447 pair, which was shown to correlate very well with Microthermometry (DeVitre and Wieser, 2024). The error bar on each datapoint shows the combination of the peak fitting error, drift correction error, and uncertainty on the densimeter (errors propagated using DiadFit, (Wieser and DeVitre, 2023). Densities for the 4 other line combinations are within error of the data reduced using the 1117-1447 cm^{-1} line pair. We also overlay lines showing the 1σ uncertainty associated with Microthermometry assuming a 0.1℃ and 0.2℃ error in sample temperature (Bakker, 2021). This analysis demonstrates that the uncertainties in the choice of data reduction strategies are small, and comparable to the errors associated with the stage temperature when performing Microthermometry.

Repeated acquisitions of Neon lines at UCB in April 22 and October 2024 shows that the shape of the nonlinearity curve shifts up and down with time, but the shape is maintained (Fig. 4a, solid lines). We also tested recalibrating the UCB spectrometer in April 2024 using a Hg-Ar lamp (WITec's default calibration routine). The nonlinearity curve is shifted down (dotted vs. solid lines, Fig. 4a), but the shape is preserved. Thus, while spectrometer nonlinearity is clearly significant, as long as calibration and natural data is processed in the same way, the nonlinearity introduces a consistent offset through time, and choice of Ne line is not a major source of uncertainty. This stability also means that the bracketing technique is not necessary, given the additional computation steps, and the relatively large uncertainty associated with fitting a polynomial through

some weaker Ne lines (e.g. 1310 cm^{-1}). However, if a laboratory wishes to change drift correction strategy, they would need to reprocess their calibration data to use the same strategy.

3.1.1 The effect of changing the Spectral Center

The significant nonlinearity in the spectrometer response shown in Fig. 1b has other implications for the densimeter equation determined for a given instrument. When setting up a Raman analysis, the user must choose the spectral center—the wavenumber at the center of the acquisition window. Along with the grating, this center position determines the range of wavenumbers collected in a single spectral acquisition. Shifting the center means that the photons at a specific wavenumber are collected on a different pixel on the charge-coupled device (CCD) within the spectrometer.

Given the strong spectral nonlinearity shown in Fig. 1b, it is worth investigating whether shifting the spectral center affects the measured splitting, because each pixel of the diad would shift to a different part of the polynomial in Fig 1b (see also Bakker 2021). We perform repeated acquisitions on an olivine-hosted CO_2-rich FI from Fogo Volcano with a bulk density of ~0.62 g/cm^3 using different spectral centers. We started at the spectral center used for calibration of the Berkeley densimeter (1325 cm^{-1}), then decreased the spectral center (1325→1320→1275→1250→1225 cm^{-1}, magenta colors, Fig. 3a). To help resolve changes from the spectral center vs instrument drift, we increased (green colors), decreased (yellow colors) and then increased (cyan) the spectral center throughout the day (Fig. 3a). We acquire a Neon line at the same spectral center as each FI measurement to correct each spectra (using the 1117-1447 cm^{-1} line pair). For each individual acquisition, we calculate the corrected splitting using the Ne line acquired at the same spectral center. Lastly, we calculate density using the UCB densimeter developed using a spectral center of 1325 cm^{-1}.

The uncorrected splitting of the diad increases by ~0.22 cm^{-1} as the spectral center is increased from 1225 to 1350 cm^{-1} (~0.0017 cm^{-1} per cm^{-1} of center shift, Fig. 3b). The change in splitting for spectral center shifts of only ~ 25 cm^{-1} apart is far larger than the variation at a given spectral center throughout the day (e.g. instrument drift). After correcting each acquisition using the Neon line collected at the same spectral center, the change in splitting is smaller, but still notable (~0.15 cm^{-1} across the window, 0.0012 cm^{-1} per cm^{-1} of shift, Fig. 3c). Calculated CO_2 density changes by 0.08 g/cm^3 across the window (Fig. 3c), which is far outside the ~0.01-0.02 g/cm^3 uncertainty of the Raman method at the densities of interest (Dayton et al., 2023; DeVitre and Wieser, 2024). Interestingly, this 0.08 g/cm^3 offset is also comparable to the offset between all the 'high resolution' densimeters identified by Remigi et al. (2021; Fig. 3c). Overall, this test indicates that unknowns

must be analysed at the same spectral center at which the calibration was performed, else calculated densities will be incorrect.

To further illustrate the influence of spectral center, we compare the densimeter developed on the UCB WITec alpha300R with densimeters developed in two laboratories at Cornell University (Cornell Center for Materials Research CCMR and Cornell Mass Spectrometry Facility CMaS, DeVitre et al., 2021). These two laboratories were calibrated with a gas cell that is very similar to that at UCB (following the design of DeVitre et al., 2021), and the Raman hardware for all three instruments is very similar: ~532 nm laser wavelength, 1800 grating, Ultra-High-Throughput-Spectrometer UHTS600 for VIS. All data was reduced with the 565.66588 - 576.44188 nm Neon line pair (corresponding to 1117-1447 for the UCB 532.046 nm laser wavelength). Comparing the fitted neon line positions to the theoretical positions (Fig. 4a) shows that each spectrometer has its own unique signature of nonlinearity.

Despite CMaS and CCMR having more similar nonlinearity responses, the CCMR densimeter shows the biggest offset in densimeter equation relative to UCB and CMaS. We suggest that this is because the UCB densimeter and the CMaS densimeter were both calibrated using a spectral center of 1325 cm^{-1}, while the CCMR densimeter was calibrated with a spectral center of 1340 cm^{-1}. The absolute difference between these densimeters reaches ~0.04 g/cm^3 (Fig. 4c). Notably, these densimeter differences cannot be explained by differences in resolution as advocated by Remigi et al. (2021), because the resolution of all three of these WITec instruments is identical.

We can also track the stability of our densimeter (and thus spectral non-linearity) with time using repeated acquisitions of FIs from Fogo volcano (FG04-A1-4 and FI FG04-101-A) collected during different analytical sessions. The standard deviation calculated from the 240 repeats on A1-4 collected by PIs, postdocs, graduate students and undergrads spanning almost two years is 0.008 g/cm^3 (Fig. 5a), and is very similar for the N=82 acquisitions of FG04-101-A (0.0078 g/cm^3, Supporting Fig. 2). For both inclusions, microthermometry measurements are within, or extremely close to the Raman analyses considering the 1σ values. Overall, this small deviation and lack of coherent trends with time indicates that at least on the WITec, changes in spectrometer nonlinearity does not cause any notable drift in the densimeter, and densimeters are remarkably stable once calibrated.

While the Neon method is clearly robust, even with variations in non-linearity, it is worthwhile to determine whether it actually helps correct for drift between and within runs.

Yamamoto and Hagiwara, (2024) show that over short-timescales (minutes) where drift is not controlled by temperature, the periodicity seen in CO_2 peak positions is not seen in Ne line acquisitions. We reprocess the repeated FI acquisitions using the median Ne correction factor for all the standard analyses after the instrument recalibration, rather than the correction factor calculated by regressing Ne correction factors as a function of time in each analytical run. The standard deviation of both FIs is extremely similar with and without an analysis-specific Ne correction. Interestingly, for FG04 one outlier is generated using a Ne line correction specific to that analysis that goes away using the average correction factor (Fig. 5a), while the opposite is true for standard FG19_101 (Supporting Fig. 2), one outlier is generated using the median Ne correction. It is noteworthy that after the instrument recalibration in April 24, the Raman was located in a laboratory with an excellent HVAC system, yielding temperature variations of <±1℃ per day, which could explain the small difference between these two correction methods.

To test the efficiency of the Neon correction under more extreme temperature fluctuations, we turned off the heating and cooling system in the Raman laboratory the night before a forecast for a hot day in Berkeley. We start the test at ~ 6:30 am after 30 mins of instrument warm up time, when the laboratory temperature was 23.5℃. Two Icelandic inclusions (Kahl et al. in review) were double polished and mounted in a Linkam THM600 stage to keep the sample temperature at 37±0.1 ℃. As the room warmed up, these two FI were analysed repeatedly. After each acquisition of the two FI, a Ne line was collected. Room temperature was measured using an Aranet4 sensor located on the table with the Raman and Ne lamp (Fig. 6a). At around 3pm, the room temperature had stabilized at around 26℃ as the external temperature peaked. To continue heating the lab, a temporary heater was switched on. At 5 pm, the temperature began to level out again, so a second heater was turned on, causing the laboratory temperature to rise to 28℃ at ~ 7:30 pm. Two air filters with a combined clean-air delivery rate of 500 cubic feet per minute were used to circulate air within the room to ensure even temperatures with these different heat sources.

The Ne correction factor shows a strong anticorrelation with temperature (Fig. 6a, note the flipped y axis for temperature). By parametrizing temperature vs. time and Neon correction factor vs. time using high order polynomials (Fig. 6a), a laboratory temperature and correction factor was calculated for each FI measurement. We calculate the corrected splitting using the Ne correction model (blue line, Fig. 6a) and compare this to corrected splitting calculated using the first Ne acquisition at the start of the day (Ne1, Fig. 6a). Fitting a linear regression for calculated density vs. laboratory temperature yields a far stronger correlation when using a constant Ne correction factor vs. the Ne correction model (0.57 vs. 0.14 for B30, and 0.74 vs. 0.39 for B23).

This indicates that during large temperature swings, the Ne line correction does help correct for instrument drift, keeping the rate of change within ~0.01 g/cm^3 for 10℃ of laboratory heating. Not using a Neon lamp could generate ~0.03-0.04 g/cm^3 of drift for 10℃. This test also shows that while it is better to have the Raman within a temperature-controlled lab, if Ne lines are used, having a suboptimal room only doubles the typical analysis error. This is excellent news for institutions and departments without the resources to build a temperature-controlled laboratory.

Overall, these tests demonstrates that spectral nonlinearity can generate significant diversity in densimeters on a single instrument based on the choice of spectra center and neon line correction routine, and that variability in these parameters can explain some of the offsets between instruments with nearly identical hardware. While it may be tempting to shift the spectral center to capture secondary peaks that appear in specific samples, or swap to a new Neon line data processing strategy, this would require a new densimeter relationship to be developed. We suggest that extreme caution must be used when applying a densimeter from another instrument, which likely has a different nonlinearity characteristic and different acquisition parameters (e.g. spectral center). Additionally, this analysis shows that just because two instruments have the same spectral resolution, does not mean they have the same densimeter (c.f. Remigi et al., 2021). In a temperature-stable laboratory, Ne line corrections are useful to tie the analysis of unknowns to the densimeter, but at least for the WITec used here, the system is stable enough there is no appreciable drift in the spectral nonlinearity over years. We suggest that measuring a Neon line every 40-60 mins is generally sufficient and possibly too frequent if the instrument is housed in a temperature-controlled laboratory environment. In contrast, if the laboratory undergoes large temperature swings, more frequent Neon acquisitions are usefull to correct for drift (Fig. 6). However, we have found that our Ne line acquisitions help us to identify days where the HVAC system was malfunctioning and correct the data for those days, given their strong relationship with laboratory temperature.

3.2 Peak fitting errors

The above analysis shows that developing a densimeter for a specific analytical conditions and drift correction methods is key to remove the large systematic offsets between different densimeters, and generate accurate measurements of CO_2 density. Now, we focus our discussion to optimizing the precision of Raman measurements. Bakker (2021) raised concerns regarding precision, noting the discrete nature of Raman spectra, which comprise x coordinates (wavenumber) collected on the CCD with spacing defined by the grating and other hardware. At each x coordinate, an intensity value is recorded, the magnitude of which is highly dependent on

the instrument. Bakker (2021) show that shifting the spectral window one pixel at a time when collecting a spectrum causes a lateral shift in the maximum peak intensity (Fig. 7). They suggest that the error on the peak center is equal to the magnitude of the spectral shift. For two different Raman set ups, they estimate a splitting error of ~ ±0.27 cm^{-1}. They emphasize that '*these numbers must be regarded as the best estimated uncertainties of Raman band peak positions'*. A splitting error of ±0.27 cm^{-1} yields an error of ±0.1 g/cm3 using the UCB densimeter. For a typical melt inclusion vapour bubbles with 3% bubble volume, this corresponds to an uncertainty of the amount of CO_2 held in the bubble of ±1111 ppm, which would introduce several kbar of uncertainty into melt inclusion saturation pressures. Similarly, a FI with a density of 0.3±0.1 g/cm^3 corresponds to pressures spanning 0.5-1.25 kbar (Span and Wagner, 1996). Overall, peak fitting errors of this magnitude would make using Raman spectroscopy for melt and FI barometry untenable, so these statements must be investigated.

We use DiadFit (Wieser and DeVitre, 2023) to refit the spectra of Bakker (2021) shown on their Fig. 18 in DiadFit (Wieser and DeVitre, 2023) using pseudovoigt peaks. Their spectra were collected as the spectral window was shifted ~3 cm^{-1} in steps of 0.137 cm^{-1} on a LabRamHR (600 grating, spectral resolution of 0.62 cm^{-1}). To help visualize the shift in the maximum y pixel intensity, we vertically stack the acquisitions collected using different spectral centers after normalizing the intensity for ease of visualization (Fig. 7a). The positions of diad 1 and diad 2 do indeed move by significant amounts as the window is shifted (Fig. 7b). Bakker (2021) state that the total error on the splitting is '*by definition, the sum of the uncertainties of the lower and upper band (i.e. peak) of* CO_2', i.e. the amount of shift – yielding 0.274 cm^{-1} in this scenario (red error bar, Fig. 7c). We also combine these errors in quadrature (purple error bar, Fig. 7c, total error= $\sqrt{diad\ 1\ shift^2 + diad\ 2\ shift^2}$, Hughes and Hase, 2010). However, it is crucial to recognise that diad 1 and diad 2 move in the same direction (Fig. 7b), such that the calculated splitting varies very little (cyan diamonds, Fig. 7c). In fact, the overall variation in calculated splitting is smaller than the estimated error from combining the peak fitting errors on diad 1 and diad 2 from lmfit in quadrature within DiadFit (Newville et al., 2016). Clearly, the errors suggested by Bakker (2021) are drastic overestimates, based on neglecting the similar effect shifting the window has on diad 1 and diad 2.

Bakker (2021) also suggest that the choice of different probability density functions (PDFs, e.g. Voigt, PseudoVoigt, Gaussian) return different center positions, and that *'these best fit reproductions provide peak position at maximum intensity, but do not consider uncertainty of each measurement'.* Fortunately, modern peak fitting packages in python such as sklearn, or lmfit (used

in DiadFit, Newville et al., 2016) provide an estimate of the uncertainty on the peak center using the covariance matrix obtained during the peak fitting process. To assess how much difference the choice of PDF makes, we fit Raman data collected on natural FIs from Fogo Volcano, Cabo Verde (DeVitre and Wieser, 2024), and Kīlauea Volcano, Hawai'i (DeVitre et al., 2024) using Voigt, PseudoVoigt, and Pearson4 functions. These were identified as the most physically-plausible peak shapes for CO_2 fluids by Yuan and Mayanovic (2017). Peak positions obtained from different fits overlap within the calculated uncertainty on the peak center (Fig. 8, Supporting Fig. 3). This can be shown more formally, by dividing the absolute difference between models by the fitting error combined in quadrature (Fig. 8c-d). Y values <1 on this plot show that the difference between functions is less than the 1 σ estimated error. This analysis demonstrates that for a wide range of CO_2 densities and signal intensity, differences between physically plausible peak fit shapes are within the stated error on each model, and that quoted peak fitting errors are realistic.

It is notable that the errors on the PseudoVoigt peak position are twice as large for diad 1 as diad 2, as a result of its lower intensity (Fig. 9a). Errors are also larger at lower CO_2 densities. However, for all inclusions, peak fitting errors are still significantly smaller than the 0.1-0.3 cm^{-1} estimated by Bakker (2021). Comparing Raman measurements with Microthermometry measurements for specific fluid inclusions provide another opportunity to assess uncertainty (Fig. 9b). We use data from N=58 FI from Fogo volcano from DeVitre and Wieser (2024) supplemented with N=39 new measurements from Galápagos made in this study using the same technique. The Raman error was estimated from Diadfit, by combining the peak fitting errors with the uncertainty from the Neon line correction model and the densimeter. This error was combined in quadrature with the uncertainty in microthermometry homogenization temperature (±0.2 ℃) to create the y error bar shown in Fig. 9b. On Fig. 9c, we perform the same analysis, but now show error bars estimated from multiple repeats of FI analyses, rather than the DiadFit peak fitting error. On both plots, the two FI with the largest offset between Raman and Microthermometry have CO_2 densities very close to critical, where Microthermometry errors are hard to quantify. The majority of inclusions lie within the ~0.01-0.02 g/cm^3 error commonly quoted for the Raman method (red bars, Dayton et al., 2023; DeVitre and Wieser, 2024; Kobayashi et al., 2012; Remigi et al., 2021). In contrast, it is clear that a splitting error of ~0.2-0.3 cm-1 (grey dotted and dashed lines) from Bakker, (2021) is a drastic overestimate (see also Yamamoto and Hagiwara, 2024, who suggest a best-case scenario splitting error of 0.0005 cm^{-1} for a high pressure optical cell).

Although the errors estimated from comparing Microthermometry and Raman (Fig. 9), and repeated measurements of standards (Fig. 5) are far smaller than that estimated by Bakker,

(2021), it is noteworthy that the standard deviation in density obtained from averaging multiple repeats is about twice as large as the error estimated from DiadFit. This DiadFit error accounts for uncertainty in peak position, Neon correction models, and the densimeter itself. In Section 3.3, we suggest that a large fraction of this unaccounted-for uncertainty comes from the temperature of the sample. Overall, once this temperature effect is accounted for, peak fitting errors estimated from PDF functions, Ne line corrections and densimeters provide a good estimate of the uncertainty of Raman analyses.

3.1.1. Optimizing Signals

While the above discussion indicates that peak fitting errors are far smaller than those indicated by Bakker (2021), it is still worthwhile investigating methods to reduce uncertainties as much as possible. This is particularly important for low density CO_2 fluids (i.e. melt inclusion vapour bubbles), where relative errors can approach 50-100% near the instrument detection limit (~0.01-0.02 g/cm^3, Bearden et al., 2025). Peak fitting errors are highly dependent on both the instrument hardware (e.g., spectrometer efficiency, spectral resolution), analytical conditions (e.g., laser power, acquisition time, number of accumulations averaged), and sample characteristics (e.g., density of CO_2, size of inclusion). Most instruments can adjust the acquisition time, which is the time spent collecting a single spectrum, and the number of accumulations, which is the number of individual acquisitions that are collected and averaged for the final spectrum. In general, increasing the acquisition time results in higher counts, and more accumulations help to average out noise in the signal. Increasing both parameters will result in better spectra, but also longer analysis times.

We investigate the interplay between acquisition time and accumulations using a variety of samples with low CO_2 densities, which have the largest peak fitting errors. To investigate the effect of changing the number of accumulations (spectra averaged), we collect 14 consecutive individual acquisitions of 45s duration using the 'slow series' option in the WITec acquisition software. We fit each acquisition individually (i.e. a single accumulation). To simulate two accumulations, we average the 1st and 2nd collected spectra, the 2-3rd, 3-4th and so forth, and then fit that averaged spectra. To simulate 3 accumulations, we average the 1-2-3rd spectra, 2-3-4th, and for 4 accumulations, the 1-2-3-4th spectra, 2-3-4-5th spectra etc. Fig. 10 shows a CO_2 capillary tube with a CO_2 density of 60 MPa, corresponding to ρ=0.011±0.011 g/cm^3 (Le et al., 2021). Supporting Fig. 4 shows the same plot for a low density melt inclusion vapour bubble from Mauna Loa (ρ=0.038±0.005 g/cm^3). Each 'averaged spectrum' is shown as a semi-transparent dot on panel a-b, and the overall average for combinations yielding N accumulations is shown as a cross with

an error bar. These tests were performed for different integration times (45s, 60s, 90s, and 120s). The errors are smaller for 90s compared with 45s, as expected given the more intense spectra, and higher signal to noise ratio (Fig. 10c vs 11d), although for both, the error for diad1 is about twice that as for diad 2. The error drops quickly as the number of accumulations is increased, and then the trend flattens out (Fig. 10a-b). In terms of assessing ways to optimize instrument time, it is useful to compare the errors in the context of the total acquisition time (Fig. 10e). Interestingly, there are no clear differences outside of error; while 90 s acquisitions have slightly smaller errors for a given total analysis time than 45 s acquisition for this capillary, for the vapour bubble, the errors for 120 s are smaller (Supporting Fig. 4). For both series, increasing total analysis times beyond about 4 minutes results in rapidly diminishing returns. We suggest that performing these tests on each specific Raman instrument can help inform an analytical strategy that is cost-effective and reduces peak fitting error as much as possible.

3.3 Sample Temperature

It is important to investigate the effect of sample temperature on calculated densities. This has implications for how the sample should be heated during Raman analyses. Heating samples above the critical point of CO_2 (31.1℃) ensures that a homogenous fluid can be analysed, which removes issues associated with analysis of a mixture of gaseous and liquid phases (see DeVitre et al. 2023). We use a low cost heating apparatus consisting of a $60 DC power supply, a $41 Peltier plate with a hole in it to maintain the ability to use transmitted light for sample navigation, and a $24 type K thermocouple with a precision of ±2℃ attached to the surface of the sample with electrical tape (Supporting Fig. 1). However, the precision of type K thermocouples means that the sample may be at 35℃ or 39℃, even if the display reads 37℃. Determining the error in splitting and density that results from this uncertainty in sample temperature is important to determine whether higher precision thermocouples or a more sophisticated heating apparatus is needed (i.e. a Linkam stage with a precision of ±0.1℃).

A number of studies have investigated how sample (and thus fluid) temperature affects diad splitting. Kawakami et al. (2003) measured CO_2-rich FIs with densities of ~1 g/cm^3 in mantle xenoliths and found that splitting stayed remarkably constant between 20-200℃ (see their Fig. 10). Thus, they deduce that splitting is sensitive only to density, and is insensitive of temperature. Wang et al. (2011) investigate splitting vs. temperature for a CO_2-rich FI (0.72 g/cm^3) and a H_2O-CO_2 FI (see their Fig. 11). Both these FI exhibit a drop in splitting of ~0.2 cm^{-1} between ~40 and 200℃, corresponding to a drop in calculated density of 0.08 g/cm^3. As well as making measurements on natural FIs with specific densities, Wang et al. (2011) also investigated

499 temperature sensitivity using a high-pressure optical apparatus where the analyte CO_2 gas was
500 held at a controlled pressure and temperature. Their acquisitions at 21, 25, 50, 100, 150 and
501 200℃ indicated that Δ decreases for a given CO_2 density as temperature increases (their
502 experiments span densities between ~0.2 and 0.7 g/cm^3).

503 Sublett et al. (2021) performed analyses on pure CO_2 in a high-pressure optical apparatus at
504 22℃, 50℃, 100℃, 200℃ and 350℃. They provide a parameterization for the relationship between
505 CO_2 density and splitting as a function of temperature (for 22-250℃ and 10-500 bars). We use
506 this equation to generate densimeters for 4 different temperatures (Fig. 11a). The strong increase
507 in pressure required to achieve a certain CO_2 content means that the densimeters for higher
508 temperatures terminate at progressively lower densities as the pressure limit of the apparatus
509 was reached. The temperature effect on splitting is largest at higher densities, and smaller at
510 lower densities, although all densities show some sensitivity to temperature. Hagiwara et al.
511 (2021, hereafter H2021) extended the results of Sublett et al. (2021, hereafter S2021) to higher
512 CO_2 densities, comparing densimeters for 23℃-200℃ for pressures between ~70-2500 bars,
513 yielding densities of ~0.65-1.2 g/cm^3 (Fig. 11b). For both H2021 and S2021, we calculate the
514 expected offset in density if an analysis is performed at X℃, but splitting is converted to density
515 using the densimeter obtained at 37 ℃ (Fig. 11c). This would reflect the sample being overheated
516 due to issues with a thermocouple and/or heating stage, or heating of the fluid by the laser itself
517 (see section 3.4). These models predict that CO_2 densities of ~0.6-0.8 g/cm^3 are the most
518 temperature sensitive, with the change in calculated density for 1 g/cm^3 being half that for 0.7
519 g/cm^3.

520 To assess these model predictions (Fig. 11c), we perform heating tests on natural olivine-hosted
521 FIs with densities spanning 0.4-0.9 g/cm^3 (Fig. 11 d-i). Double polished wafers were placed within
522 a LinkamTHMS600 stage and spectra were acquired at 6 mW laser power at temperatures
523 between 37℃ and 70℃. To account for the possibility of instrument drift, analyses were run with
524 increasing temperature and then decreasing temperature (2 repeats made at each temperature).
525 We fit a linear regression to plots of temperature vs. density, and use this to define a density at
526 37℃. For each acquisition, we then subtract this 37 ℃ from the calculated density. The change in
527 density is largest for FI with densities of ~0.4-0.7 g/cm^3, and smallest for ones at 0.9 g/cm^3. We
528 compare the change in density to that predicted from H2021 and S2021 (Fig. 11c, d-i). The
529 extrapolation of the H2021 model for the 0.4 g/cm^3 FI overpredicts the change in density with
530 heating, while S2021 (within its calibration range) underpredicts it. Both models, but particularly
531 H2021, do a good job of predicting the change in density for the inclusions at ~0.7 g/cm^3 (Fig.

11c, e-g). Both models drastically overpredict the density change for the inclusions at ~0.9 g/cm^3 (Fig. 11h-i).

These temperature-density gradients can be used to assess the uncertainty introduced by measuring the sample temperature. The gradients (Fig. 11e-i) mean that the ±2℃ error introduced from the thermocouple causes an additional error of ±0.0008-0.0028 g/cm^3. Combined with offsets we observe based on the type of tape used to stick the thermocouple down (1-2℃), we believe sample temperature variation accounts for the factor of 2 offset determined from repeated analyses of standards vs. the average error estimated from the uncertainty in spectral and Ne fitting, and the densimeter alone (Fig. 5). However, this is still a small uncertainty, and the additional analytical time and instrument cost required to heat samples in a Linkam stage is not justified.

3.4. Laser Power

These heating tests give us a framework to assess the effect of laser power on CO_2 density. This has been a topic of extensive debate in the literature. Fall et al. (2011) suggest that the laser doesn't heat the inclusion more than a few 10ths of a degree, based on observations that many inclusions analysed in their laboratory which homogenized during microthermometry at temperatures very close to laboratory temperature still showed distinctive liquid and gaseous phases when analysed by Raman spectroscopy. However, Hagiwara et al. (2021b) simulate laser heating with a numerical model, concluding that the absorption coefficient of the host mineral is the most important parameter for determining the amount of heating, because the CO_2 inclusion itself has very little absorption at the wavelengths of the laser. They perform Raman analyses at varying laser powers, and use a thermometer based on hot bands to determine the laser heating coefficient B (℃ per mW of laser power) for FIs in olivine, orthopyroxene, clinopyroxene, spinel and quartz. It is notable how much lower their B values are for quartz (0.010-0.014℃/mW) vs. mafic minerals such as olivine (0.02-1℃/mW). In their tests, as laser power is changed from 4-14 mW, the olivine FI shows a ~0.02 g/cm^3 decrease in density while the quartz inclusion shows no change outside uncertainty. Thus, while Fall et al. (2011) do not note the host mineralogy of the inclusions they draw their conclusions based on, the inclusion shown in their figure that they reference as evidence for a lack of laser heating is hosted in quartz. If the Fall et al. (2011) observations are from quartz inclusions, they are not in conflict with the results of Hagiwara et al. (2021b) who predict minimal heating for quartz.. DeVitre et al. (2023) also demonstrate the effect of laser heating on calculated CO_2 densities through the analyses of olivine-hosted melt inclusion

564 vapour bubbles with densities of ~0.3, 0.5 and 0.6 g/cm^3. They show a clear drop in splitting (and
565 thus density) with increasing power (~0.1 g/cm^3 from 0-20 mW).

566 It is vital to determine the effect of laser heating in different samples and bring some consensus
567 to the literature, because it is very tempting to use high laser powers for analysis to obtain strong
568 signals and small peak fitting errors. For example, Supporting Figure. 5 shows the peak fitting
569 error associated with the analysis of FIs and vapour bubbles using laser powers ranging from ~5-
570 35 mW. A laser power of ~5 mW yields a peak fitting error 2-3X higher than a laser power of 35
571 mW. This reduction in error seems highly beneficial for low density samples like melt inclusion
572 vapour bubbles (often 0.02-0.04 g/cm^3), where peak fitting errors can introduce an uncertainty of
573 20-50% in density.

574 We perform analyses at laser powers from ~5 to 50 mW on 4 olivine-hosted melt inclusion vapour
575 bubbles from Mauna Loa and the Cascades (Bearden et al., 2025; Wieser et al., 2023), 29 olivine-
576 hosted FIs from Iceland (Kahl et al. in review), Fogo volcano (DeVitre et al., 2023b), and American
577 Samoa, and 3 pyroxene-hosted FI from the Galápagos (Gleeson et al., 2025). These span a wide
578 range of CO_2 densities (Fig. 12, Supporting Figs 6-10). We also perform power series on the FI
579 and melt inclusion vapour bubbles that were used for heating series (Fig. 13, Supporting Fig. 6-
580 7). As for temperature, we analyse each FI with increasing then decreasing laser power. We
581 calculate the gradient of a linear regression between laser power and CO_2 density. We find that
582 this gradient varies dramatically between different fluids from ~0 to -0.005 g/cm^3 per mW (Fig.
583 12a, Supporting Figure 4-5). In general, FIs show weaker negative gradients than melt inclusions
584 from the same samples (see Supporting Fig. 10). However, FIs show great diversity in gradients.
585 The largest change in density is for FI 101C from Fogo volcano. Over 50 mW, the calculated
586 depth would change by 8 km (Fig. 13d). The three Icelandic FI shown in Fig. 12c-e show density
587 change varies from -0.08 g/cm^3 to -0.018 g/cm^3 for a 50 mW change in laser power. The drop in
588 density for B22_1_FIA between 0-50 mW corresponds to a change in calculated depth of ~ 3km
589 (Fig. 12c, RH axis). These changes in density are far larger than the uncertainty on each Raman
590 measurement (see error bars, Fig. 12c-e).

591 For a subset of fluid inclusions, EDS measurements were conducted to determine the forsterite
592 (Fo) content of the host olivine. We observe a strong correlation between the measured gradient
593 and the Fo content (Fig. 12b). This relationship is consistent with the known dependence of olivine
594 color on Fo content, which will affect the absorption coefficient. A wide variety of absorption
595 coefficients for olivine have been reported in the literature. For their laser heating simulations,
596 Hagiwara et al. (2021) use an olivine absorption coefficient of 1.14 cm^{-1} based on measurements

of a hydrothermal olivine from the Cola Peninsula, Russia (Fo_{95} Taran and Matsyuk, 2013). In contrast, Chassé et al. (2015) report an olivine absorption coefficient at wavenumbers corresponding to a 532 nm green laser (~18800 cm^{-1}) of 11 cm^{-1} (the Fo content is not given). Other papers have shown that the absorption coefficient of olivine is sensitive to the Fo content, and the crystallographic orientation of the host (Hazen et al., 1977; Taran and Matsyuk, 2013; Ullrich et al., 2002). For example, at 532 nm, a Fo_{90} crystal has an absorption coefficient of ~6 cm^{-1} parallel to a vs. 3 cm^{-1} parallel to b (Ullrich et al. 2002). For Fo_{10}, the coefficient parallel to the b axis is ~97 cm^{-1} and 76 cm^{-1} parallel to c. This large difference in absorption coefficient as a function of olivine Fo content likely accounts for the stronger laser heating experienced by lower Fo olivine hosts (Fig. 12b).

However, olivine chemistry cannot explain all the variability in laser heating rates. Crystal 101 from Fogo volcano contains three FI in the same secondary trail within ~100 µm of each other (Supporting Fig. 12). FIC experiences a very dramatic drop in density, from ~0.93 g/cm^3 to ~0.75 g/cm^3 over 50 mW of heating (gradient of -0.033 g/cm^3 per mW). In contrast, FIB experiences no change in density outside of uncertainty (gradient of -0.0001 g/cm^3 per mW), and FIA experiences a minor drop with a gradient of -0.0006 g/cm^3 per mW. Initially, we thought the extreme heating experienced by FIC may result from its proximity to the surface (~6 µm depth). However, when the crystal was flipped over and a power series was performed from the other side (~68 µm depth), the gradient was almost identical (Supporting Fig. 13). 3D mapping reveals that 101C contains carbonate (Supporting Fig. 14). It has been suggested that microparticles which are not visible optically can enhance the laser heating effect (e.g. Burke, 2001). It is possible that carbonate is playing this role. The two Icelandic samples that lie off the trend in Fig. 12b also contain notable carbonate in 3D maps. However, interestingly, of the three FI from American Samoa (pink edges, Fig. 12b), the two which follow the gradient-Fo trend defined by the Icelandic samples contain abundant carbonate, while the one with more negative gradients contains no carbonate.

Performing laser heating and laser power tests on the same FI allows us to estimate the heating coefficient, B (℃/mW of laser power). For each FI, we calculate the gradient of density vs. temperature, and density vs. laser power. On Fig. 13, we adjust the power and temperature scale such that the gradients of the two datasets align. We calculate B as:

$$\text{B } (℃/mW) = \frac{Grad\ (\frac{g}{cm3}/\ mW)}{Grad\ (\frac{g}{cm3}/\ ℃)}$$

B values range from 0.22 to 5.3 $℃/\mathrm{mW}$, compared to 0.02-1℃/mW from Hagiwara et al. (2021). Overall, these power series demonstrate that while laser heating can be partially predicted based on the absorption coefficient of the host, the extreme change in density experienced by very specific FI, replicated across different analytical sessions in our lab, is worrying. Given that many melt and FIs are analysed prior to knowing the Fo content (as that is often the final step of measurement) and that we cannot diagnose why a few FI show such extreme heating, this work demonstrates that it is absolutely vital to use low laser powers, as the heating response is currently not entirely predictable.

3.5. Other strategies to optimize signal.

Having to use low laser powers is a real issue in terms of getting enough signal to minimise peak fitting errors. In addition to optimizing the acquisition times (Fig. 10), it is worth thinking about other ways to optimize signals. Our repeated measurements of FI standards (Fig. 5) not only allow us to track the stability of the densimeter, but also the intensity of signals with time. If the FI standard returns lower peak heights than normal, we analyse a Si chip. We use the oscilloscope feature ('live spectra' on HORIBA) to perform micro adjustments on the pinhole position to enhance laser transmission through the fiber. We find that this can easily increase signals by a factor of 2-3. We typically adjust this every few weeks, although sometimes it goes months with no decline in signal, and other times we have to readjust after a few days. Typically, after HVAC or power failures, adjustments are needed, suggesting this adjustment is required based on thermal expansion/contraction of components. On a mirror-based instrument, mirror alignments will have a similar effect.

Once the system's optics are optimized, it is worth considering the analytical geometry. The depth of the FI within the sample has been discussed in a variety of papers. Frezzotti et al. (2012) note that the depth resolution of Raman spectroscopy degrades with depth in the sample, so it is best to analyse FI within 30 μm of the surface. Burke, (2001) states that 'usually one strives to analyse inclusions as near the surface as possible' inclusions deeper than 50 μm start to give problems, especially if their density is not too high'. To assess the influence of FI depth, we individually ground 3 olivine-hosted FI down, performing analyses after each round of grinding and polishing. We measure the depth by focusing on the surface of the sample in RL, and then focusing down to the melt inclusion. We correct the movement of the Z stage to true depth accounting for the refractive index of olivine ($N_{olivine}$ ~1.7, 1.64-1.67 for Fo, 1.84-1.89 for Fa).

True depth = $N_{olivine}\, Z_{stage\ movement}$

We use the WITec autofocus function at each depth. Surprisingly, we find no coherent trends in signal intensity (quantified here using the area of diad 2) or the error on calculated density with increasing depth in the sample (Fig. 14a, Supporting Fig. 17-19). However, we do find big changes with minor changes in focus at a single sample depth. To demonstrate this, we perform acquisitions at different focuses when the FI was 91.8 μm deep in the sample. We first find the optical focus yielding a sharp inclusion edge (yellow box and spectra, Fig. 14). We then use the WITec autofocus feature at 50 mW. This collects spectra for ~3 s at various depths to find the maximum intensity in user-selected spectral window. The z position was ~ 2 μm close to the surface than the best optical focus and yielded very similar signal strengths (black spectra and box). We then used the oscilloscope function to manually scroll through Z positions to find the best signal (pink box and spectra). The 6 focus positions between -14.1 μm and 0 μm all yield optically reasonable images, and yet the signal strength varies by a factor of 3. Interestingly, the blue focus position (+2.3 μm) yields an optically poor image, but still a better focus than the oscilloscope feature found. This comparison clearly demonstrates that focus has far more effect on spectral strength than changing the depth in the sample by ~250 μm (Fig. 14 c-d).

This result was replicated for several inclusions (Supporting Fig. 17-21). We also find that the signal can vary quite considerably spatially, and small shifts in x-y position can also result in stronger signals. This becomes very apparent when taking 2D transects through and across FI (Supporting Fig. 22-23). We suggest that when signals are weak, the autofocus or oscilloscope feature should be used to investigate different x-y-z positions around the optimal focus. We perform these tests at high laser power (49 mW) for speed, and the drop the power to perform the analyses at the optimal Z position. Variability in signal strength can also be seen by performing 2D and 3D maps of signal intensity.

Conclusions

In summary, we investigate the effect of several instrument and data reduction methods on the accuracy and precision of Raman analyses. Our findings can be summarized as follows:

1. The spectra center and drift correction method (e.g. choice of Ne and Ar lines) used for densimeter calibration must be replicated when analysing unknowns in future sessions. Spectral resolution alone cannot account for the diversity in published densimeters, and even for a single spectral resolution, a single instrument can generate a wide variety of densimeter relationships as the spectral center or drift correction method is changed because of the nonlinearity of the spectrometer.

2. Estimates of peak fitting error from pseudovoigt curves, combined with uncertainty in the Ne line correction model, account for approximately half the scatter seen in repeated Raman analyses of the same inclusion over ~ 2 years (~0.004 g/cm^3 for FI with densities of >0.6 g/cm^3). These low uncertainties make prior suggestions of very large peak fitting errors untenable. The additional 0.004 g/cm^3 of scatter seen in repeated standard acquisitions likely results from uncertainty in the temperature of the sample. However, , this small uncertainty does not justify a more sophisticated heating apparatus for most geological applications.
3. We recommend tracking the density of a single standard during every run to ensure there has been no drift from the laboratory densimeter relationship. These standards also help to track the efficiency of the instrument (e.g. checking the peak heights are as high as previous days), so the user knows when re-alignment is required.
4. In a temperature-controlled laboratory, drift during and between analytical sessions is minimal using an WITec alpha300R Raman. However, when the laboratory temperature is perturbed, the Ne line correction helps to reduce instrument drift by a factor of ~3. Thus, while it is better to have a Raman in a temperature-controlled laboratory, it is not essential. Large temperature swings of +5℃ result in an additional uncertainty of <0.01 g/cm^3 if Ne lines are used for drift correction.
5. Laser heating is a significant issue, particularly for materials with higher optical absorption coefficients (e.g., silicate glass, lower Fo olivine). However, absorption coefficients alone are not enough to explain the large variability in heating response seen. 6mW laser power seems a good way to minimise heating for all but the most strongly laser-heated samples, while still providing sufficient signal to obtain good peak fits.
6. To help counteract the relatively weak signals achieved using low laser powers, the analyst should investigate the play off between uncertainty and acquisition time for their specific instrument. They should experiment with different focuses using an autofocus/live spectra function of the oscilloscope at high power to find the optimum signal within the fluid. Focus has a far larger effect than depth to the fluid within the sample (even at depths of ~250 μm).

Acknowledgments

PW and CD acknowledge funding from NSF EAR 2217371, EAR 2342156, the Sloan foundation, and the Berkeley Rose Hills Innovator Program. IS was funded through a SURF and Ramsden summer fellowship at UCB. The authors are very grateful to the producers of lmfit, without which this study would not have been possible. We thank Maren Kahl for supplying the Icelandic

samples, Drew Downs for the American Samoa samples, and Matthew Gleeson for the Galápagos samples. We are grateful to Alex Bearden for his early contributions to investigating laser heating in some Mauna Loa vapour bubbles.

Supporting Information

All data and Jupyter Notebooks needed to recreate the figures in this study are provided in the Github repository. We also supply a supporting spreadsheet containing processed data for each figure (e.g. peak fits etc).

PennyWieser/Raman_Best_Practices: Code for Raman best practices paper by Wieser et al.

Author Contributions

PW and CJD conceived the project. PW, CJD and IS collected the Raman data and performed peak fitting. PW wrote the manuscript. All authors contributed to the discussion of ideas and the editing of the manuscript.

Figure Captions

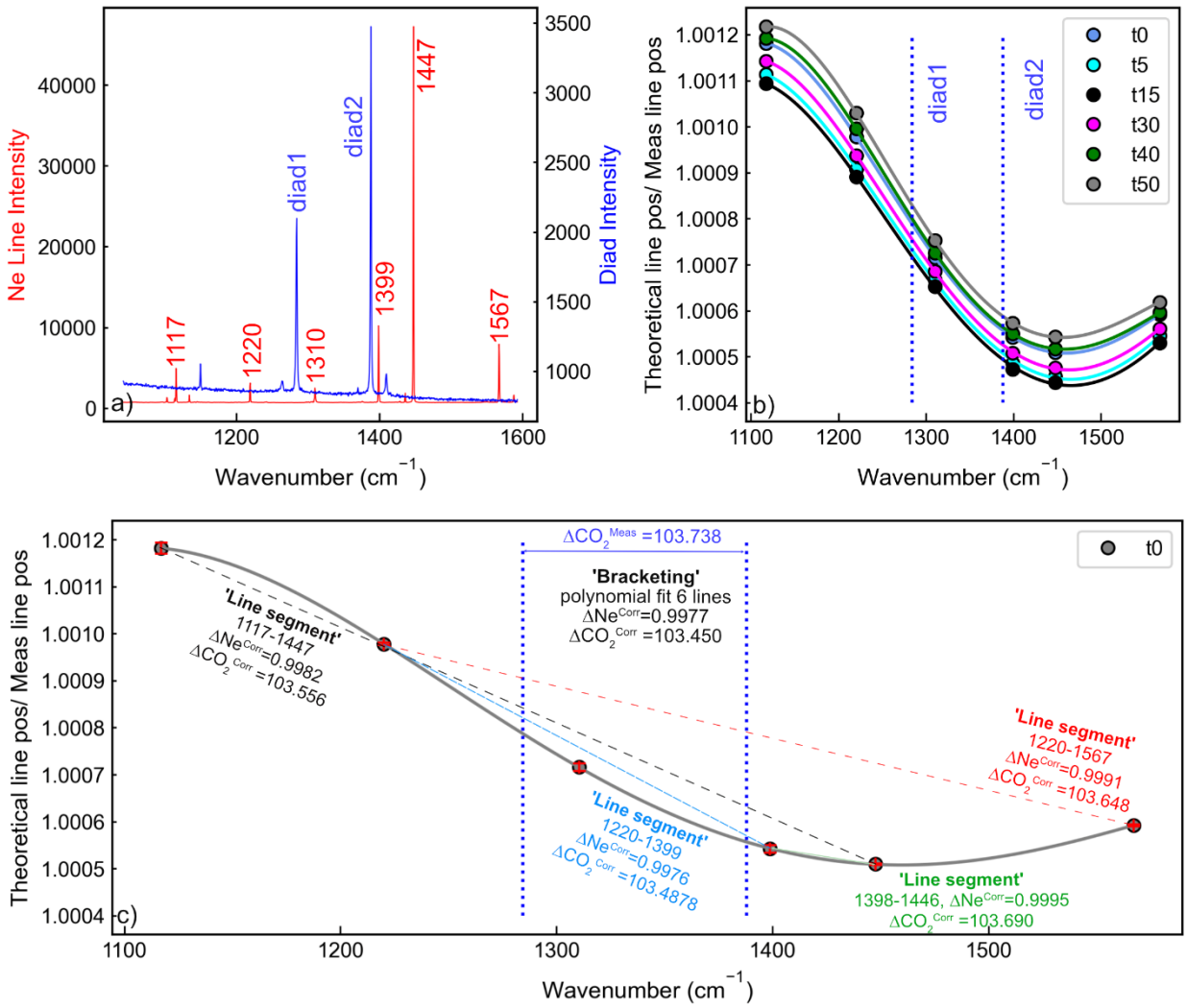

Figure 1 – Fitting Neon lines to demonstrate differences between the Line segment method and the bracketing technique. a) An example Ne line acquisition compared to a diad. Note that the intensity of the Ne (left hand axis) is almost 10X stronger than the diad (right hand axis). This is different from Fig. 8 of Bakker 2021 where Ne lines show very low intensities. b) For repeated acquisitions of Ne lines through the day, the actual peak position is compared to the theoretical peak position. For each line acquisition, a polynomial has been fitted through the data. c) For the first acquisition (t0), we show the polynomial fit through the 6 Ne peaks. The 'Bracketing technique' would correct each diad position based on the value for the polynomial at that wavenumber (where the blue dotted lines intersect the grey line). The 'Line segment' method will give similar results if the gradient drawn between two points is parallel to the intersection of the dotted blue and grey lines.

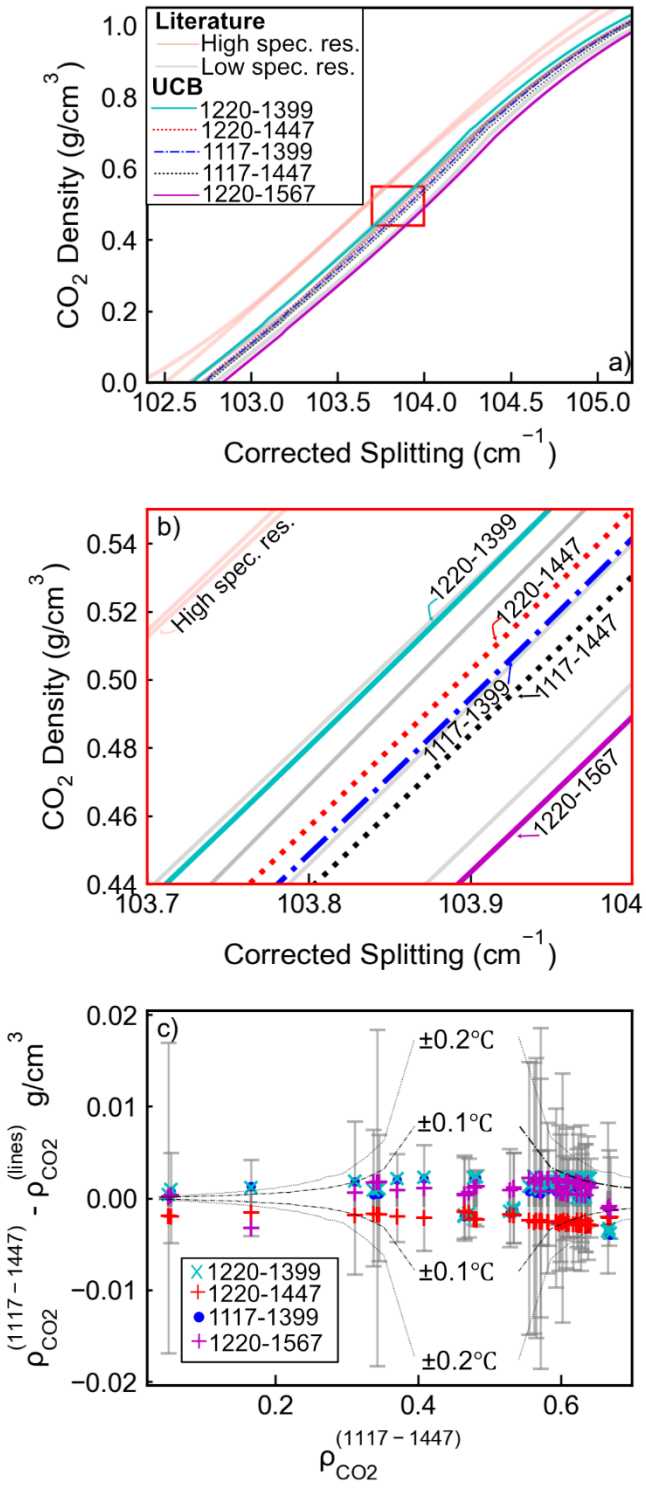

Figure 2 – Assessing the effect of different Ne line reduction routines on densimeters and densities calculated for natural FIs. a) The relationship between corrected splitting and CO_2 density (i.e. the densimeter) was determined using 5 different pairs of Neon lines for the same UCB calibration dataset. This variation is compared to other literature densimeters (grey = high precision, salmon – low precision based on the definitions of Remigi et al. 2021). b) Inset of area in red box in a). c) Natural FI data from DeVitre and Wieser, (2024) was reduced using these different Neon correction routines and densimeters. The y axis shows the difference in density for the default 1117-1447 line option compared with other data reduction strategies. The grey error bar shows the uncertainty on the 1117-1447 density. This demonstrates densities are within uncertainty as long as spectra from uknowns and calibration data are reduced in the same way. For reference, we overlay the uncertainty associated with Microthermometry for ±0.1 and 0.2℃ in sample temperature.

778

779

780

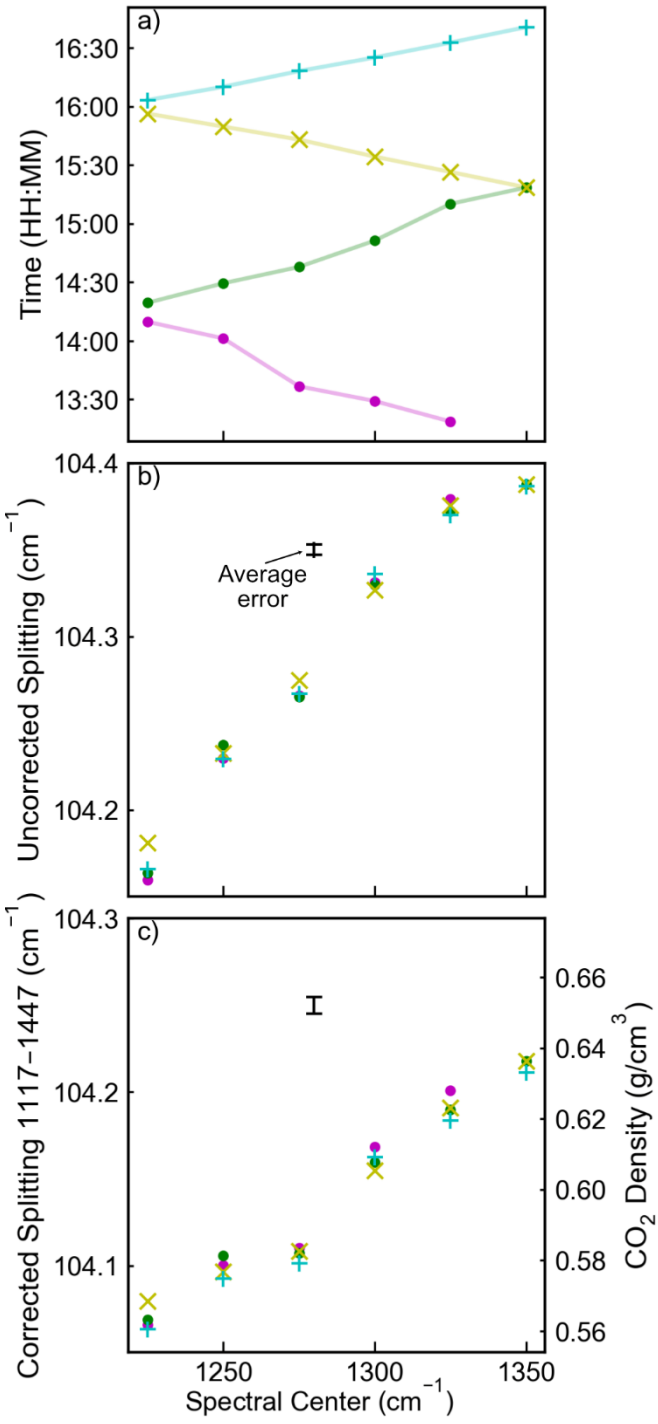

Figure 3 – Change in splitting and calculated density for a single FI as a function of the spectral center. a) The four symbol colors show 'up' and 'down' cycles changing the spectral center as a function of time through the day. b) Uncorrected splitting vs. spectral center and c) corrected splitting, using Ne lines collected at the same spectral center as the diad. The black error bars show a representative error for the splitting (b) and corrected splitting (c) respectively (offset from trend for clarity). The density axis in c is calculated using the densimeter developed for a spectral center of 1325 cm-^{1}.

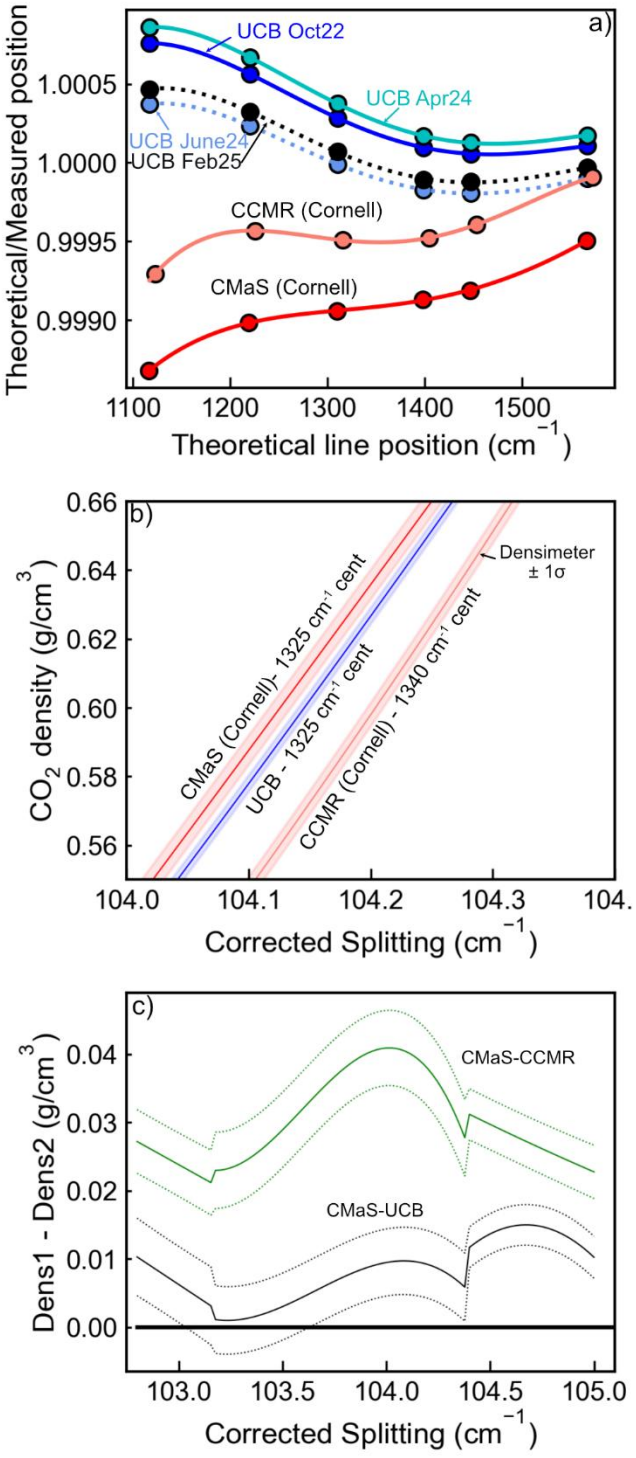

Figure 4 – a) Comparison of spectral nonlinearity determined from Ne line acquisitions for three different WITec alpha300R instruments. b) Comparison of the densimeters across a smaller density range showing that UCB and CMaS are more similar than CCMR and CMaS, despite CCMR-CMaS showing much more similar spectral non-linearities (a). c) Difference between densimeters as a function of splitting. The filled lines on b) show the 1σ errors on the densimeter fit, combined in quadrature and shown as dashed lines in c).

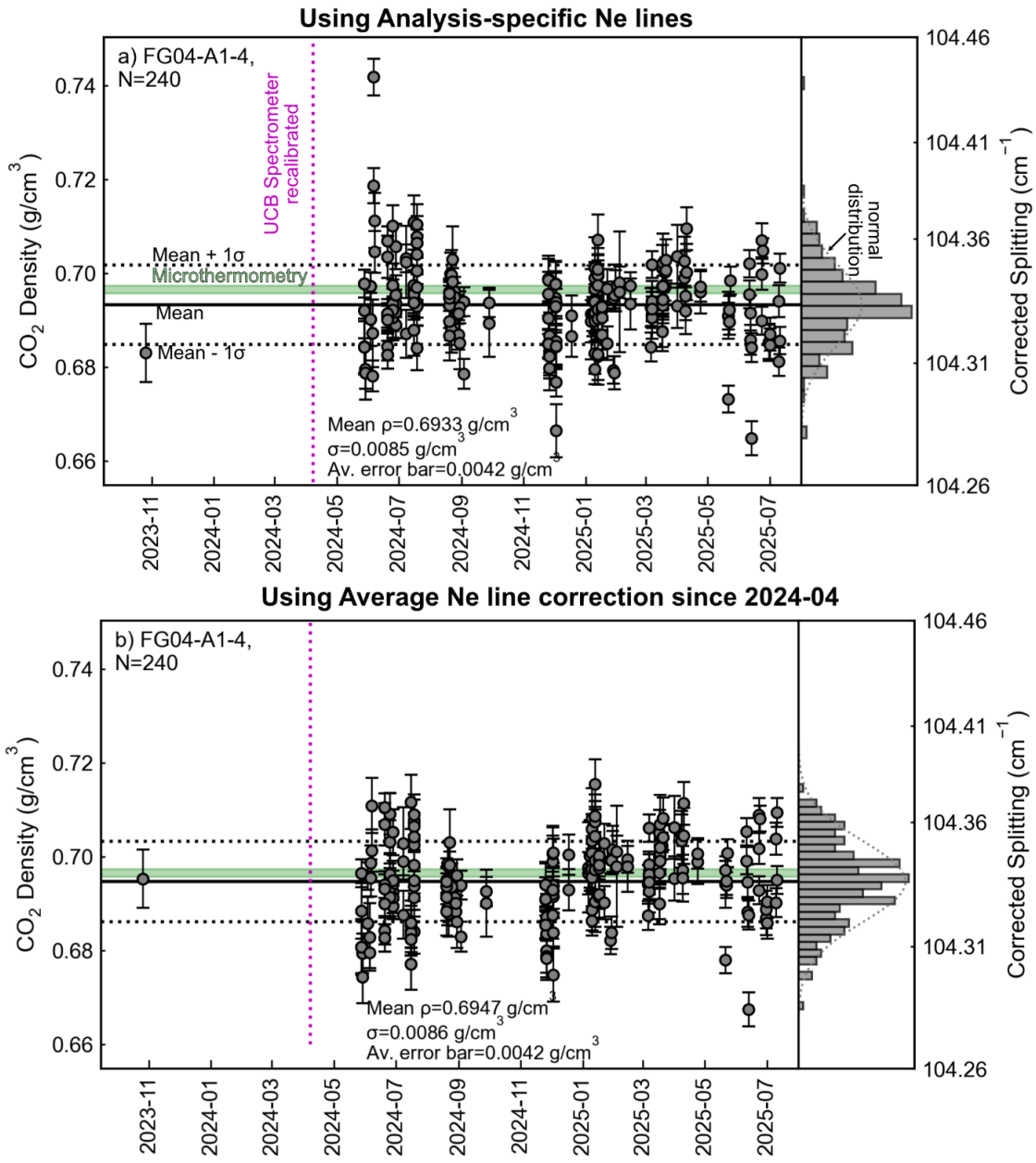

Figure 5- Long-term variability in standard value for FI FG04-A1-4 collected at UCB. a) Data reduced using a Ne drift correction model for each analytical session. b) Data reduced using the average Ne line correction factor for all standard acquisitions after the spectrometer recalibration (marked with a magenta line). The green bar shows the density determined by Microthermometry, accounting for the uncertainty in the temperature reading of the stage. The black solid line shows the mean Raman value for the standard, and the dotted black lines ±1 σ. The distribution of densities is shown as a histogram, compared to a normal distribution based on the mean and standard deviation. Supporting Fig. 2 shows a second standard run less frequently at UCB.

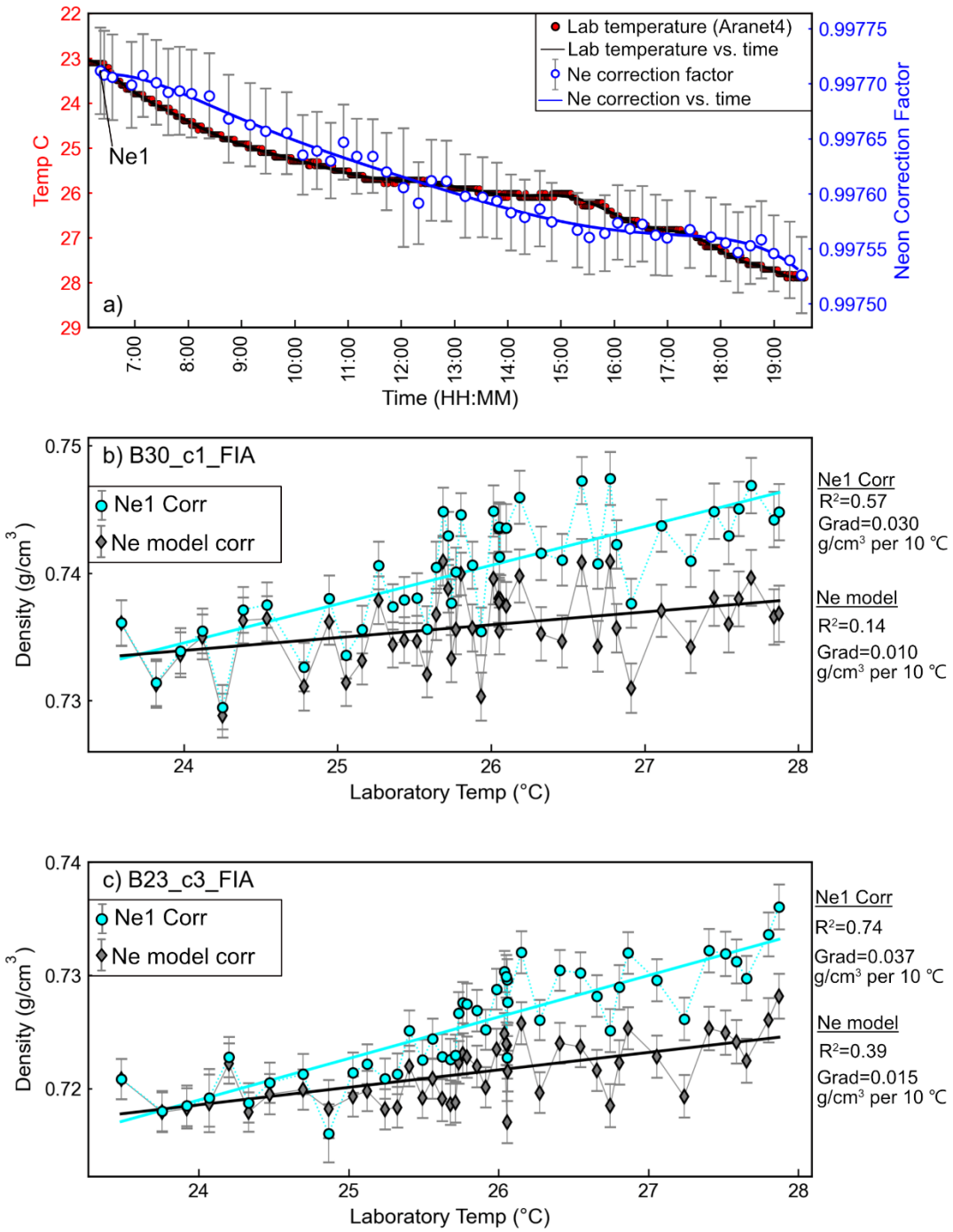

833

834 Figure 6 – Testing the sensitivity of Raman acquisitions to large fluctuations in room temperature.
835 a) Temperature log from an Aranet4 logger (red dots) against time. The white circles with blue
836 dots show the Ne correction factor calculated for each Ne line acquisition. These series were fitted
837 with a regression (black and blue lines) to calculate temperature and Ne correction factor for each
838 FI acquisition. b) Change in density of FI B30_c1_FIA as a function of laboratory temperature.

The grey diamonds are corrected based on the Ne line correction model (blue line in a), while the cyan circles use the correction factor for the first Ne acquisition (to replicate not applying a drift correction through time). The straight lines represent linear regressions, with the statistics shown on the right. c) Same for B23_c3_FIA.

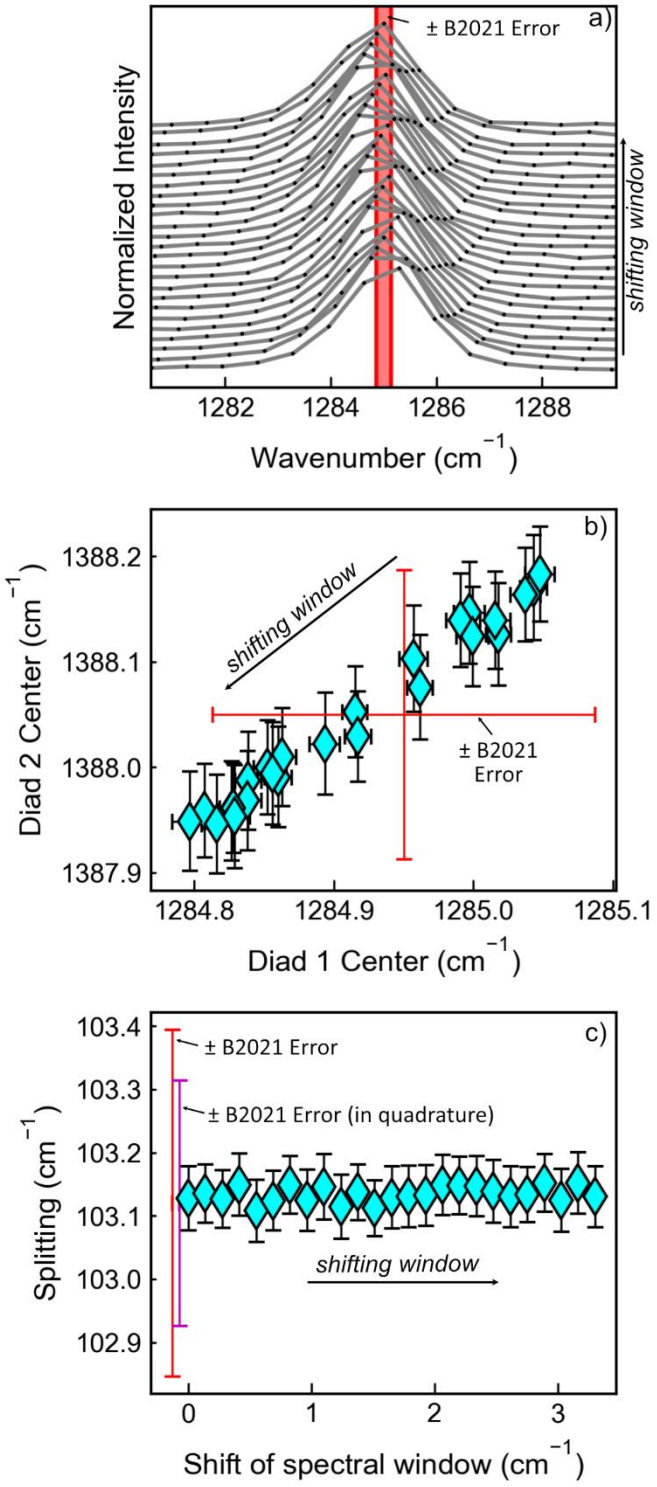

Figure 7. a) Stacked spectra collected as the spectral window was progressively shifted by Bakker (2021). The red band shows their stated error on the peak position, based on the wavenumber shift in the window. b) Plot showing the changing position of diad1 and diad2 for each acquisition shown in a). The error bar shows the 1 sigma error estimated by lmfit from the peak fit c) Change in splitting as a function of the shift of the window. Errors estimated by Bakker (2021) are shown in red, and purple shows their stated error on each peak combined in quadrature. The black error bar shows the uncertainty based on the lmfit peak positions propagated in quadrature.

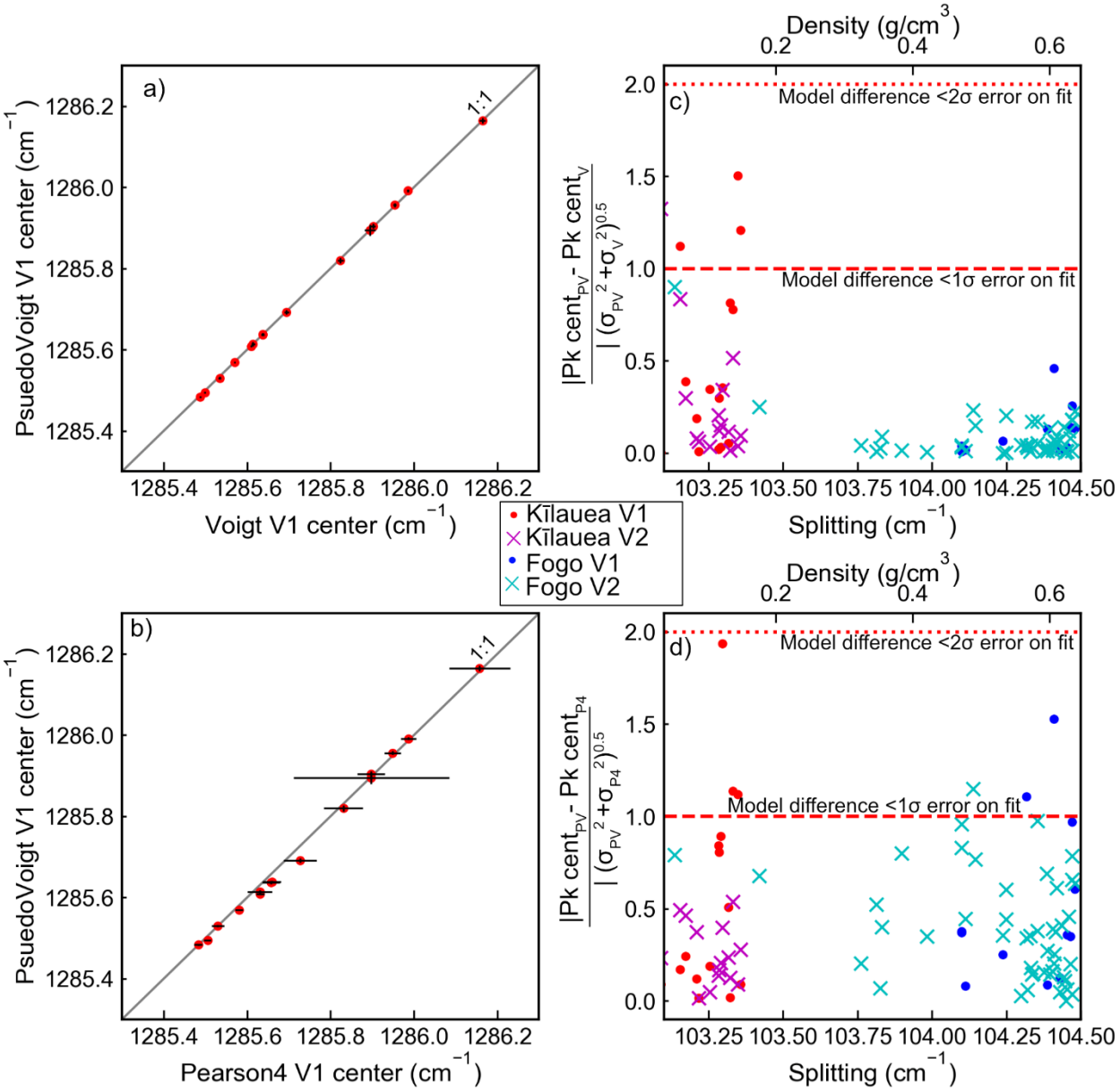

Figure 8 - Comparison of peak centers obtained with Voigt (V), Psuedovoigt (PV) and Pearson4 (P4) peak fits for Diad 1 (V1) and Diad2 (V2) for natural FIs from Fogo and Kīlauea Volcano. a-b) Comparison of Diad 1 position for Kīlauea FI, with errorbars showing the 1σ error on each peak fit from lmfit. c-d) The absolute difference between the peak center for each model is divided by the error on each model combined in quadrature. For datapoints lying below 1, the absolute difference between the models is smaller than the 1σ on each model. All differences are <2 σ. Comparison of PDF fits for the Fogo inclusions like in a-b) are shown in Supporting Fig. 3.

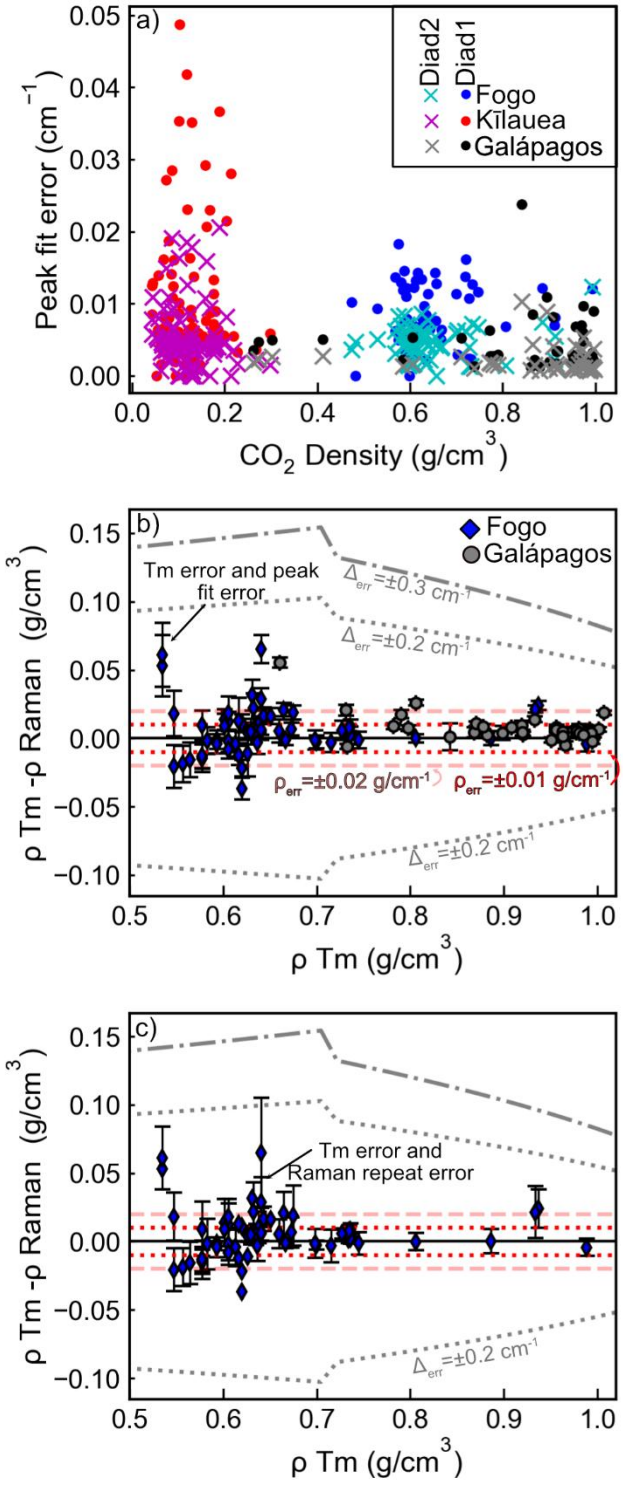

Figure 9 –Assessment of Raman errors using natural FIs with independent density constraints from microthermometry a) Errors on each peak position obtained from lmfit for low and high density FIs from DeVitre and Wieser (2024) from Kīlauea and Fogo, and from the Galápagos (this study). b) Comparison of densities obtained from Raman spectroscopy and Microthermometry. The error bars show 1 sigma errors estimated from peak fitting, analytical drift and densimeter uncertainty for Raman spectroscopy and Microthermometry combined in quadrature. c) Same comparison but using standard errors calculated from repeated Raman measurements (only FI with repeated analyses are shown). On b-c), we overlay the ±1 σ error bounds that would result from the splitting errors suggested by Bakker (2021). We also overlay red lines showing the errors determined from numerous studies comparing Raman and Microthermometry (±0.01-0.02 g/cm^3).

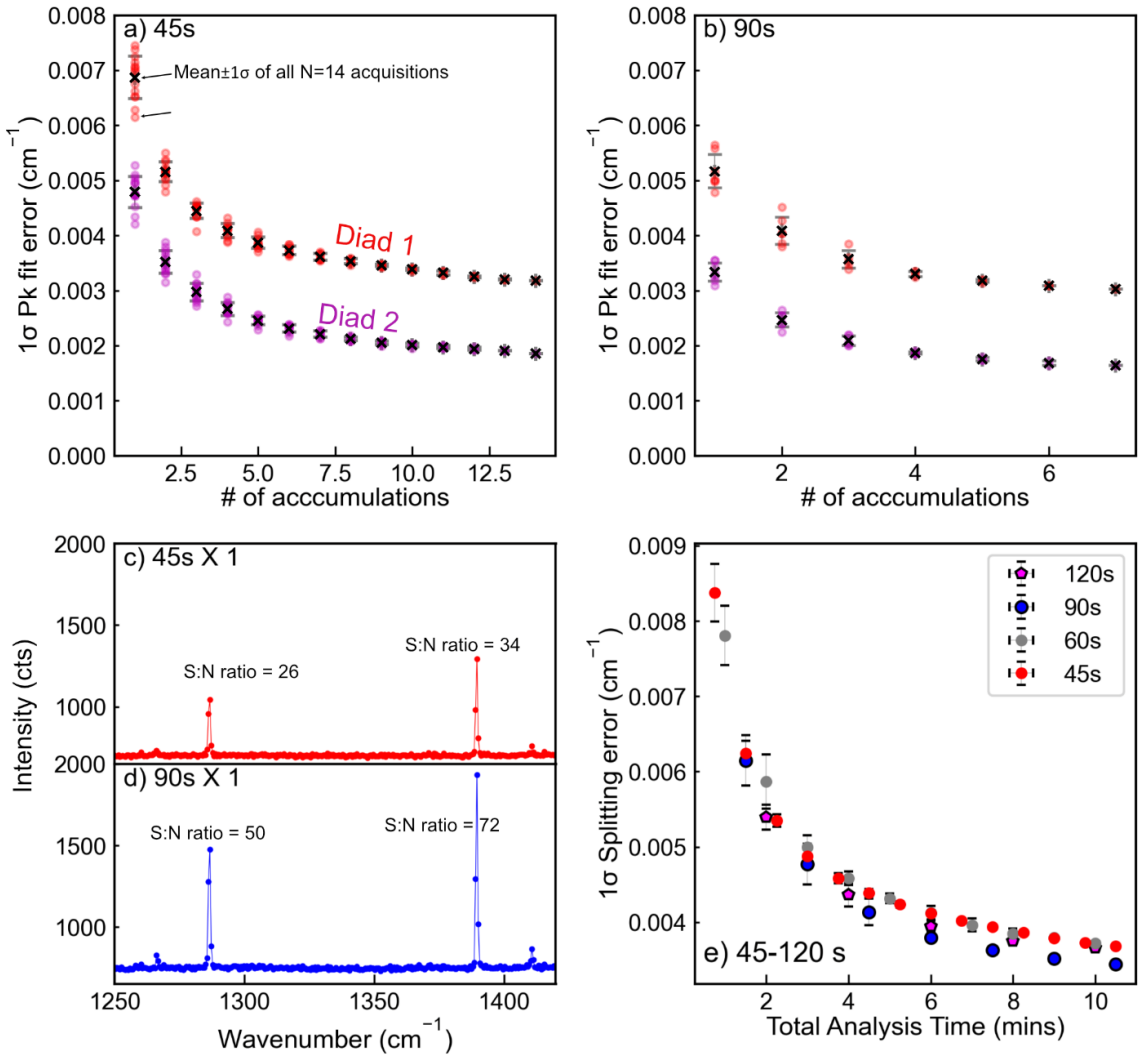

Figure 10 – Investigating peak fitting error as a function of integration time and accumulations using a low density capillary tube (~0.01 g/cm^3, Le et al., 2021). a-b) Error on the peak position of diad1 and diad2 for 45 and 90s acquisitions. The x axis shows the number of spectra that were averaged prior to fitting the peaks (analogous to accumulation). The dots show an individual fitted spectra (e.g. spectra 1 to 14 for accumulations =1, average of spectra 1-2, 2-3 3-4 for n=2 accumulations etc.), and the cross and error bar show the mean and standard deviation of averaged spectra for each number of accumulations (e.g. 14 individually fitted spectra for n=1 accumulations). c-d) Example spectra for 45s x 1 and 90s x 1. The signal to noise (S:N) ratio is calculated as the height of the highest pixel divided by the standard deviation of the region between the two diads. e) Error on peak fitting as a function of total acquisition time. For example, five 120s acquisitions were averaged for the 10 minute total acquisition time. The same figure for a low density melt inclusion vapour bubble is shown in Supporting Fig. 4.

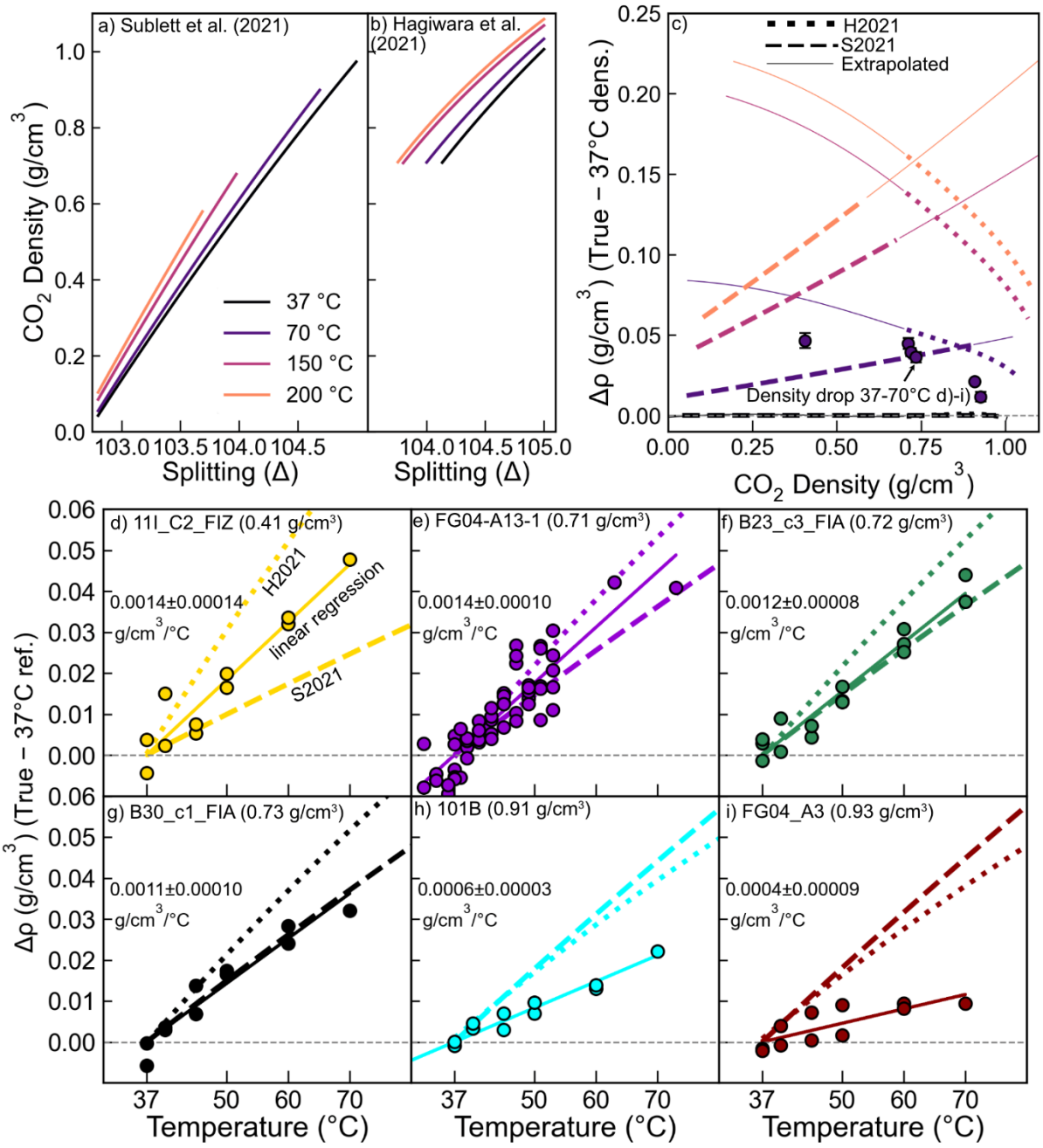

Figure 11 – Temperature sensitivity of splitting. a) Relationship between splitting and CO_2 for 4 temperatures calculated using equation 8 of Sublett et al. (2021, hereafter S2021). b) Same using equation 2 of Hagiwara et al. (2021a, hereafter H2021). We only show the lines within the calibration range of each study. c) Difference between true density of a FI and the density calculated using the 37℃ when analysed at T=X℃. Thin straight lines represent the equations of S2021 and H2021 when extrapolated outside their calibration range. d-i) For each inclusion, a linear regression was produced between calculated density using the 37℃ densimeter and the

sample temperature (Supporting Fig. 4). The 'True' density of the inclusion was determined from the best fit line at 37℃. This was then compared to the calculated density at T=X using the 37℃ densimeter (i.e. panel d, the density at 70℃ was 0.05 g/cm3 lower than the intercept at 37 ℃). The dotted and dashed lines show the predicted change in density using the models of H2021 and S2021 respectively.

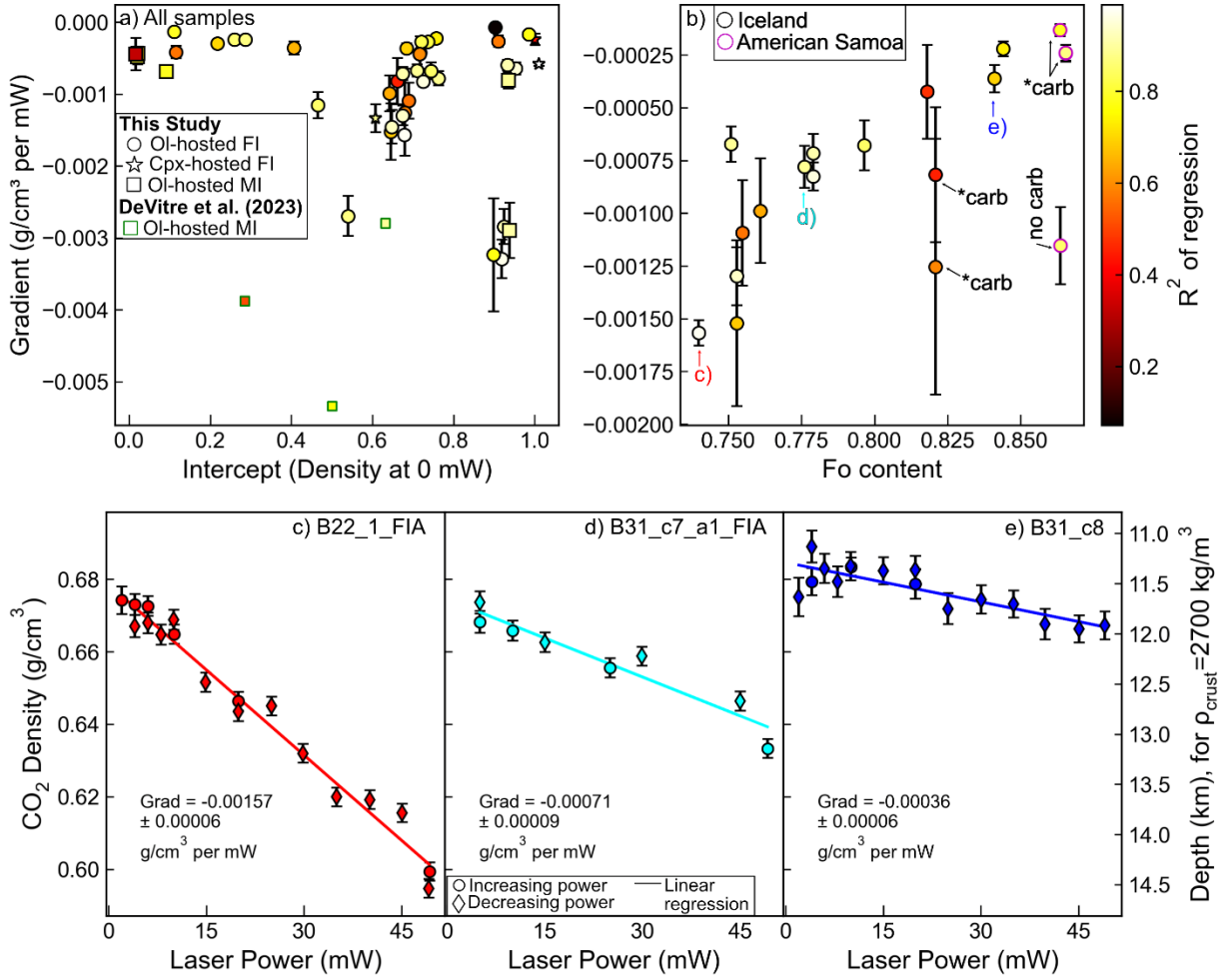

Figure 12 – Relationship between density and laser power. a) Gradient of laser power vs. density for all the heating tests conducted here (individual regressions shown in Supporting Figures). Symbol shapes show the host mineral and whether the sample is a fluid inclusion or melt inclusion. Squares with green edges show the three melt inclusions from DeVitre et al. (2023) b) Gradient of each power series vs. the forsterite content of the host crystal. FI with a carbonate are indicated with arrows. c-e) Laser power series on three Icelandic FI indicated by arrows in b).

The circle symbols show data collected at increasing laser power, and the diamonds at decreasing laser power. The gradients for the best-fit linear regression are shown.

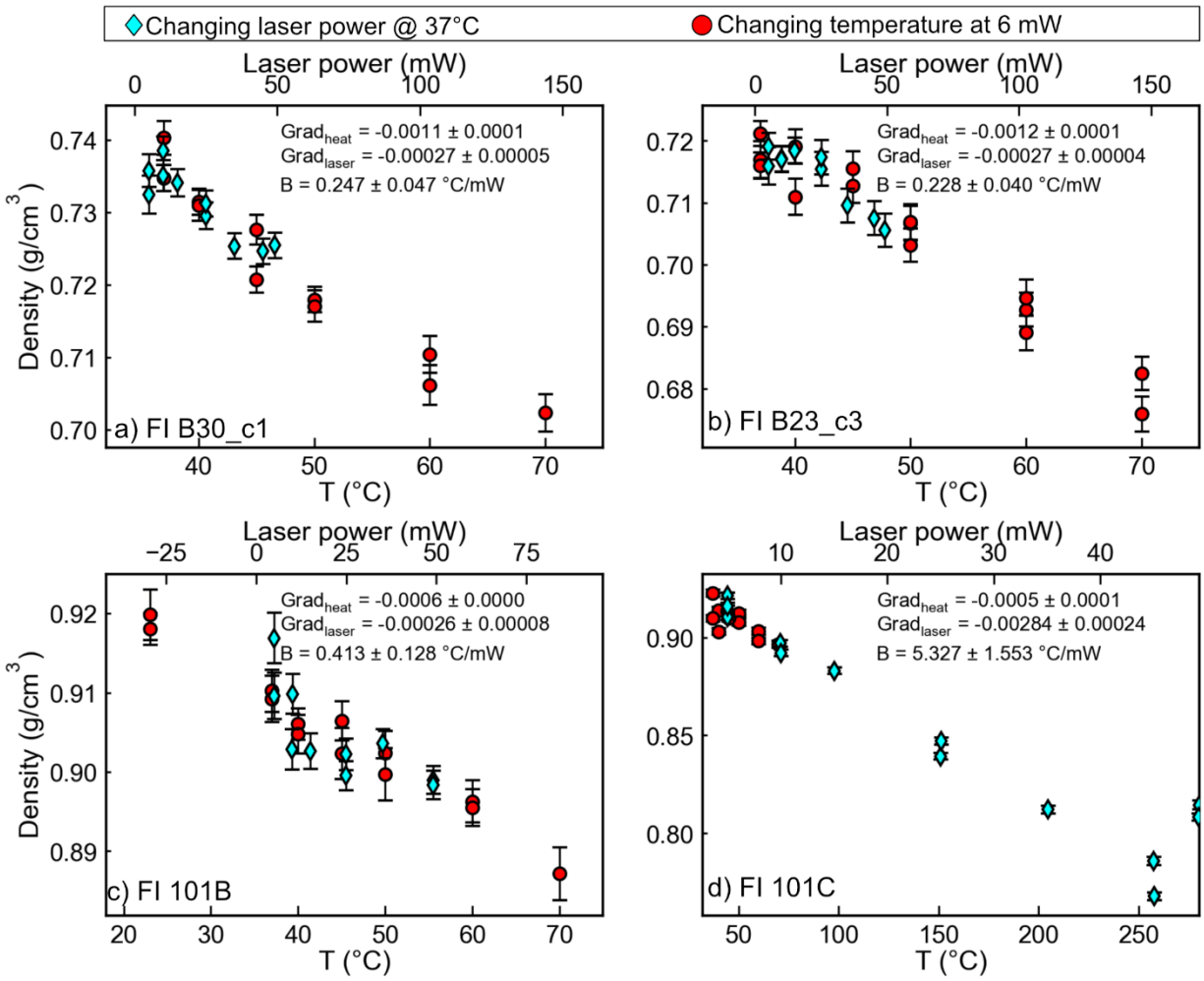

Figure 13 – Comparison of heating and laser power series. For each FI, we perform acquisitions at temperatures from 37-70℃ (red circles) at 6 mW, and at laser powers from 6 mW to ~50 mW with the sample temperature controlled at 37℃ (cyan diamonds). We adjust the limits of the two x axes such that the gradients of these two data series are identical. The gradient of each series is shown, along with the B value. The most noteworthy comparisons are 101B and 101C, which are located within 100 μm of each other (see Supporting Fig. 12).

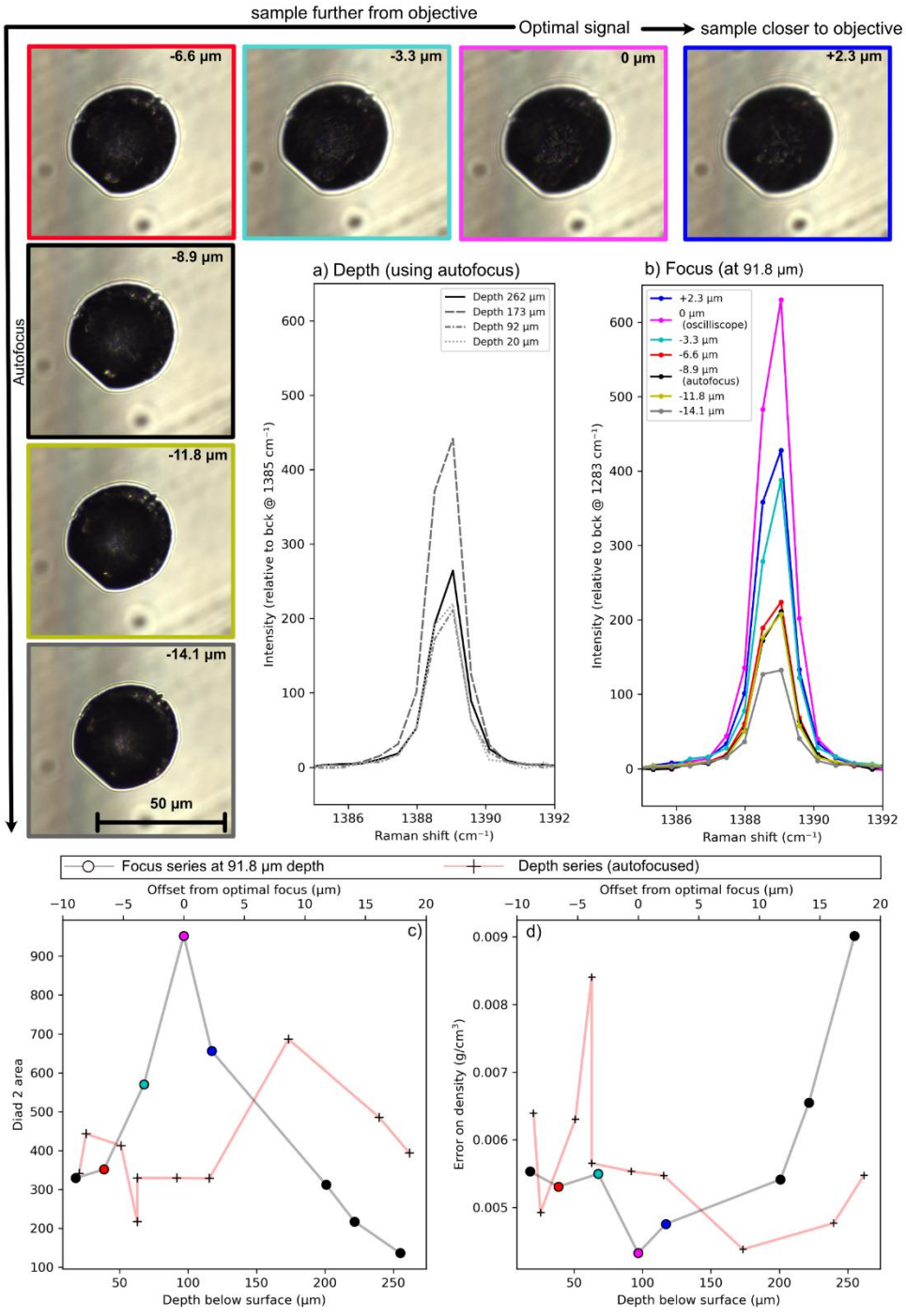

Figure 14 – Investigation of how signal strengths are affected by focus vs. depth in the sample. a) Spectra near Diad 2, showing the signal strength for different depths of the FI in the sample during serial sectioning. After each polishing round, the autofocus function was used to find the optimum depth. b) When the FI was at 91.8 µm depth in the sample, we acquire spectra at 7 different focus positions. The black spectra and dot represents the focus position found by the

autofocus, and the pink spectra and dot the best focus position using the oscilloscope feature. The images on the left-hand side show what the FI looked like at each focus. c) Change in diad 2 intensity and d) density error as a function of depth in the sample (circles) and focus (crosses).

References

Allison, C.M., Roggensack, K., Clarke, A.B., 2021. Highly explosive basaltic eruptions driven by CO2 exsolution. Nat. Commun. 12, 217. https://doi.org/10.1038/s41467-020-20354-2

Bakker, R.J., 2021. The perfection of Raman spectroscopic gas densimeters. J. Raman Spectrosc. 52, 1923–1948. https://doi.org/10.1002/jrs.6245

Bearden, A.T., Wieser, P.E., Rangel, B., DeVitre, C.L., Gleeson, M.L.M., Monteleone, B.D., Lynn, K.J., 2025. Volatile systematics and magma storage depths at Mauna Loa: a melt inclusion perspective., in: In Chapman Conference on Caldera-Forming Eruptions at Basaltic Volcanoes: Insights and Puzzles from Kīlauea and Beyond. AGU.

Burke, E.A.J., 2001. Raman microspectrometry of fluid inclusions. Lithos 55, 139–158. https://doi.org/10.1016/S0024-4937(00)00043-8

Chassé, M., Lelong, G., Van Nijnatten, P., Schoofs, I., De Wolf, J., Galoisy, L., Calas, G., 2015. Optical Absorption Microspectroscopy (μ-OAS) Based on Schwarzschild-Type Cassegrain Optics. Appl. Spectrosc. 69, 457–463. https://doi.org/10.1366/14-07628

Dayton, K., Gazel, E., Wieser, P., Troll, V.R., Carracedo, J.C., La Madrid, H., Roman, D.C., Ward, J., Aulinas, M., Geiger, H., Deegan, F.M., Gisbert, G., Perez-Torrado, F.J., 2023. Deep magma storage during the 2021 La Palma eruption. Sci. Adv. 9, eade7641. https://doi.org/10.1126/sciadv.ade7641

DeVitre, C.L., Allison, C.M., Gazel, E., 2021. A high-precision CO2 densimeter for Raman spectroscopy using a Fluid Density Calibration Apparatus. Chem. Geol. 584, 120522. https://doi.org/10.1016/j.chemgeo.2021.120522

DeVitre, C.L., Dayton, K., Gazel, E., Pamukçu, A., Gaetani, G., Wieser, P.E., 2023a. Laser heating effect on Raman analysis of CO2 co-existing as liquid and vapor in olivine-hosted melt inclusion bubbles. Volcanica 6, 201–219. https://doi.org/10.30909/vol.06.02.201219

DeVitre, C.L., Gazel, E., Ramalho, R.S., Venugopal, S., Steele-MacInnis, M., Hua, J., Allison, C.M., Moore, L.R., Carracedo, J.C., Monteleone, B., 2023b. Oceanic intraplate explosive eruptions fed directly from the mantle. Proc. Natl. Acad. Sci. 120, e2302093120. https://doi.org/10.1073/pnas.2302093120

DeVitre, C.L., Wieser, P.E., 2024. Reliability of Raman analyses of CO2-rich fluid inclusions as a geobarometer at Kīlauea. Geochem. Perspect. Lett. 29, 1–8. https://doi.org/10.7185/geochemlet.2404

DeVitre, C.L., Wieser, P.E., Bearden, A.T., Richie, A., Rangel, B., Gleeson, M.L.M., Grimsich, J., Lynn, K.J., Downs, D.T., Deligne, N.I., Mulliken, K.M., 2024. Depths in a day — A new era of rapid-response Raman-based barometry using fluid inclusions. J. Petrol. egae119. https://doi.org/10.1093/petrology/egae119

Fall, A., Tattitch, B., Bodnar, R.J., 2011. Combined microthermometric and Raman spectroscopic technique to determine the salinity of H2O–CO2–NaCl fluid inclusions based on clathrate melting. Geochim. Cosmochim. Acta 75, 951–964. https://doi.org/10.1016/j.gca.2010.11.021

Fermi, E., 1931. Über den ramaneffekt des kohlendioxyds. Z. Für Phys. 71(3–4).

Frezzotti, M.L., Tecce, F., Casagli, A., 2012. Raman spectroscopy for fluid inclusion analysis. J. Geochem. Explor. 112, 1–20. https://doi.org/10.1016/j.gexplo.2011.09.009

Gleeson, M., Wieser, P.E., DeVitre, C.L., Shi, S.C., Millet, M.-A., Muir, D.D., Stock, M.J., Lissenberg, J., 2025. Persistent High-Pressure Magma Storage beneath a Near-Ridge Ocean Island Volcano (Isla Floreana, Galápagos). J. Petrol. 66, egaf031. https://doi.org/10.1093/petrology/egaf031

Hagiwara, Y., Kawano, T., Takahata, K., Torimoto, J., Yamamoto, J., 2021a. Temperature dependence of a Raman CO_2 densimeter from 23°C to 200°C and 7.2 to 248.7 MPa: Evaluation of density underestimation by laser heating. J. Raman Spectrosc. 52, 1744–1757. https://doi.org/10.1002/jrs.6188

Hagiwara, Y., Yoshida, K., Yoneda, A., Torimoto, J., Yamamoto, J., 2021b. Experimental variable effects on laser heating of inclusions during Raman spectroscopic analysis. Chem. Geol. 559, 119928. https://doi.org/10.1016/j.chemgeo.2020.119928

Hazen, R., Mao, H., Bell, P.M., 1977. Effects of compositional variatoin on absorption spectra of lunar olivine. Proc Lunar Sci Conf 8th 1081–1090.

Howe, T.A., Christopher, T.E., Moune, S., Tuffen, H., Schiavi, F., 2025. Melt inclusion bubbles provide new insights into crystallisation depths and CO2 systematics at Soufrière Hills Volcano, Montserrat. Front. Earth Sci. 12, 1509409. https://doi.org/10.3389/feart.2024.1509409

Hughes, I., Hase, T., 2010. Measurements and their uncertainties: a practical guide to modern error analysis. OUP.

Kawakami, Y., Yamamoto, J., Kagi, H., 2003. Micro-Raman Densimeter for CO_2 Inclusions in Mantle-Derived Minerals. Appl. Spectrosc. 57, 1333–1339. https://doi.org/10.1366/000370203322554473

Kobayashi, T., Yamamoto, J., Hirajima, T., Ishibashi, H., Hirano, N., Lai, Y., Prikhod'ko, V.S., Arai, S., 2012. Conformity and precision of CO_2 densimetry in CO_2 inclusions: microthermometry *versus* Raman microspectroscopic densimetry: Conformity and precision of CO_2 densimetry in CO_2 inclusions. J. Raman Spectrosc. 43, 1126–1133. https://doi.org/10.1002/jrs.3134

Kramida, A., Ralchenko, Y., 1999. NIST Atomic Spectra Database, NIST Standard Reference Database 78. https://doi.org/10.18434/T4W30F

Lamadrid, H.M., Moore, L.R., Moncada, D., Rimstidt, J.D., Burruss, R.C., Bodnar, R.J., 2017. Reassessment of the Raman CO 2 densimeter. Chem. Geol. 450, 210–222. https://doi.org/10.1016/j.chemgeo.2016.12.034

Le, V.-H., Caumon, M.-C., Tarantola, A., 2021. FRAnCIs calculation program with universal Raman calibration data for the determination of PVX properties of CO2–CH4–N2 and CH4–H2O–NaCl systems and their uncertainties. Comput. Geosci. 156, 104896. https://doi.org/10.1016/j.cageo.2021.104896

McLennan F.R.S., J.C., Smith M.A., H.D., 1932. RAMAN EFFECTS WITH LIQUID AND SOLID CARBON DIOXIDE. Can. J. Res. 7, 551–555. https://doi.org/10.1139/cjr32-104

Moore, L.R., Gazel, E., Tuohy, R., Lloyd, A.S., Esposito, R., Steele-MacInnis, M., Hauri, E.H., Wallace, P.J., Plank, T., Bodnar, R.J., 2015. Bubbles matter: An assessment of the contribution of vapor bubbles to melt inclusion volatile budgets. Am. Mineral. 100, 806–823. https://doi.org/10.2138/am-2015-5036

Newville, M., Stensitzki, T., Allen, D.B., Rawlik, M., Ingargiola, A., Nelson, A., 2016. LMFIT: Non-linear least-square minimization and curve-fitting for Python. Astrophys. Source Code Libr. ascl-1606.

Remigi, S., Mancini, T., Ferrando, S., Frezzotti, M.L., 2021. Interlaboratory Application of Raman CO_2 Densimeter Equations: Experimental Procedure and Statistical Analysis Using Bootstrapped Confidence Intervals. Appl. Spectrosc. 75, 867–881. https://doi.org/10.1177/0003702820987601

Rosso, K.M., Bodnar, R.J., 1995. Microthermometric and Raman spectroscopic detection limits of C02 in fluid inclusions and the Raman spectroscopic characterization of C02. Geochim. Cosmochim. Acta 59, 3961–3975. https://doi.org/10.1016/0016-7037(95)94441-H

Song, Y., Chou, I., Hu, W., Robert, B., Lu, W., 2009. CO2 Density-Raman Shift Relation Derived from Synthetic Inclusions in Fused Silica Capillaries and Its Application. Acta Geol. Sin. - Engl. Ed. 83, 932–938. https://doi.org/10.1111/j.1755-6724.2009.00090.x

Span, R., Wagner, W., 1996. A New Equation of State for Carbon Dioxide Covering the Fluid Region from the Triple-Point Temperature to 1100 K at Pressures up to 800 MPa. J. Phys. Chem. Ref. Data 25, 1509–1596. https://doi.org/10.1063/1.555991

Sublett, D.M., Sendula, E., Lamadrid, H.M., Steele-MacInnis, M., Spiekermann, G., Bodnar, R.J., 2021. Raman spectral behavior of N_2, CO_2, and CH_4 in N_2–CO_2–CH_4 gas mixtures from 22°C to 200°C and 10 to 500 bars, with application to other gas mixtures. J. Raman Spectrosc. 52, 750–769. https://doi.org/10.1002/jrs.6033

Taran, M.N., Matsyuk, S.S., 2013. Fe2+, Mg-distribution among non-equivalent structural sites M1 and M2 in natural olivines: an optical spectroscopy study. Phys. Chem. Miner. 40, 309–318. https://doi.org/10.1007/s00269-013-0572-x

Ullrich, K., Langer, K., Becker, K.D., 2002. Temperature dependence of the polarized electronic absorption spectra of olivines. Part I - fayalite. Phys. Chem. Miner. 29, 409–419. https://doi.org/10.1007/s00269-002-0248-4

Wang, W., Caumon, M.-C., Tarantola, A., Pironon, J., Lu, W., Huang, Y., 2019. Raman spectroscopic densimeter for pure CO2 and CO2-H2O-NaCl fluid systems over a wide P-T range up to 360 °C and 50 MPa. Chem. Geol. 528, 119281. https://doi.org/10.1016/j.chemgeo.2019.119281

Wang, X., Chou, I.-M., Hu, W., Burruss, R.C., Sun, Q., Song, Y., 2011. Raman spectroscopic measurements of CO2 density: Experimental calibration with high-pressure optical cell (HPOC) and fused silica capillary capsule (FSCC) with application to fluid inclusion observations. Geochim. Cosmochim. Acta 75, 4080–4093. https://doi.org/10.1016/j.gca.2011.04.028

Wieser, P., DeVitre, C., 2023. DiadFit: An Open-SourcePython3 Tool for Peak fitting of Raman Data from silicate melts and CO2 fluids (preprint). Earth Sciences. https://doi.org/10.31223/X5CQ1F

Wieser, P., Kent, A.J.R., DeVitre, C.L., Gazel, E., Till, C.B., Johnson, Emily, Wallace, Paul, Couperthwaite, F.K., 2023. Bubble Trouble: Raman measurements of Cascade melt inclusion vapour bubbles indicate substantial underestimation of magma storage depths in legacy data. Presented at the AGU Fall Meeting 2023. Poster No. 0203, id. V23D-0203.

Wieser, P.E., Lamadrid, H., Maclennan, J., Edmonds, M., Matthews, S., Iacovino, K., Jenner, F.E., Gansecki, C., Trusdell, F., Lee, R.L., Ilyinskaya, E., 2021. Reconstructing Magma Storage Depths for the 2018 Kīlauean Eruption From Melt Inclusion CO_2 Contents: The Importance of Vapor Bubbles. Geochem. Geophys. Geosystems 22. https://doi.org/10.1029/2020GC009364

Wright, R.B., Wang, C.H., 1973. Density effect on the Fermi resonance in gaseous CO2 by Raman scattering. J. Chem. Phys. 58, 2893–2895. https://doi.org/10.1063/1.1679594

Yamamoto, J., Hagiwara, Y., 2024. Precision evaluation of Raman densimetry for carbon dioxide: improvement by correction for the drift effect. Appl. Opt. 63, 1402. https://doi.org/10.1364/AO.507939

Yamamoto, J., Kagi, H., 2006. Extended Micro-Raman Densimeter for CO_2 Applicable to Mantle-originated Fluid Inclusions. Chem. Lett. 35, 610–611. https://doi.org/10.1246/cl.2006.610

Yuan, X., Mayanovic, R.A., 2017. An Empirical Study on Raman Peak Fitting and Its Application to Raman Quantitative Research. Appl. Spectrosc. 71, 2325–2338. https://doi.org/10.1177/0003702817721527

Supporting Information for: Best practices for the analyses of CO_2 fluids by Raman Spectroscopy

Penny E. Wieser[1*], Charlotte L DeVitre[1, 2], Isabelle Susman[1]

[1] Earth and Planetary Sciences, University of California, Berkeley, CA 94270, USA

[2] Now at Department of Earth and Environmental Sciences, University of Ottawa, Ottawa, ON K1N 6N5, Canada

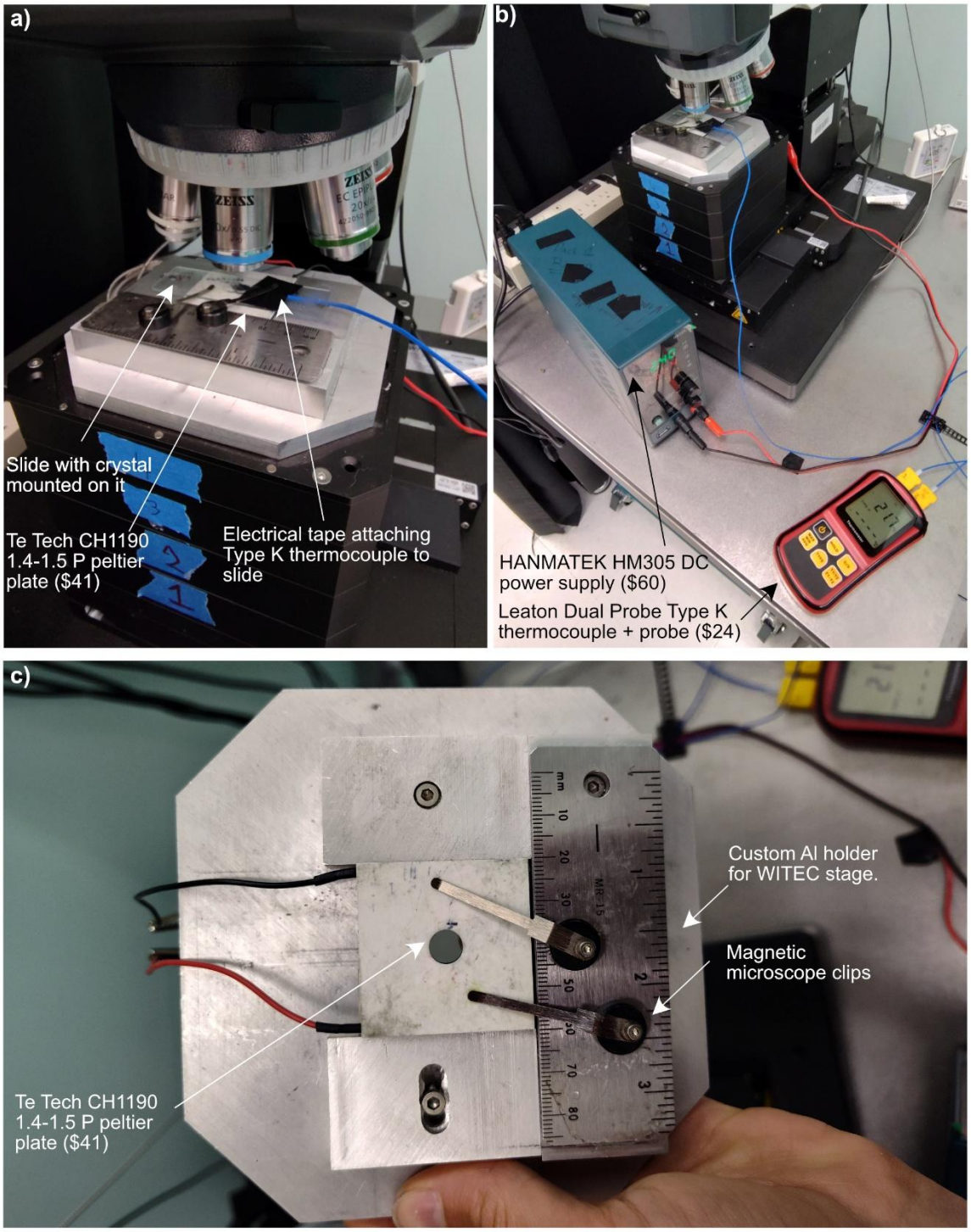

Supporting Figure 1 – Apparatus used for heating samples to 37℃. a) Picture showing a glass slide with a FI mounted in crystalbond under a 50X Zeiss objective. b) Picture showing the entire WITec system and the sample holder. A Type K thermocouple is taped on using electrical tape. This picture was taken while the slide was still warming up (hence the 21.7 ℃ temperature). c) Close up of the custom Aluminum holder that has the bottom machined out to slot onto the shape of the WITec base. There are 4 screws that attach to the magnets on the WITec stage (because Al is not magnetic). The ruler is glued to the top to provide a magnetic surface to attach a set of

magnetic microscope clips to help keep the sample in place. This holder was manufactured by our in-house machine shop (labour and material cost, $900), and can be ordered by contacting Wieser. This holder keeps the peltier plate and sample still, making it possible to analyze very small inclusions without drift (1-2 µm).

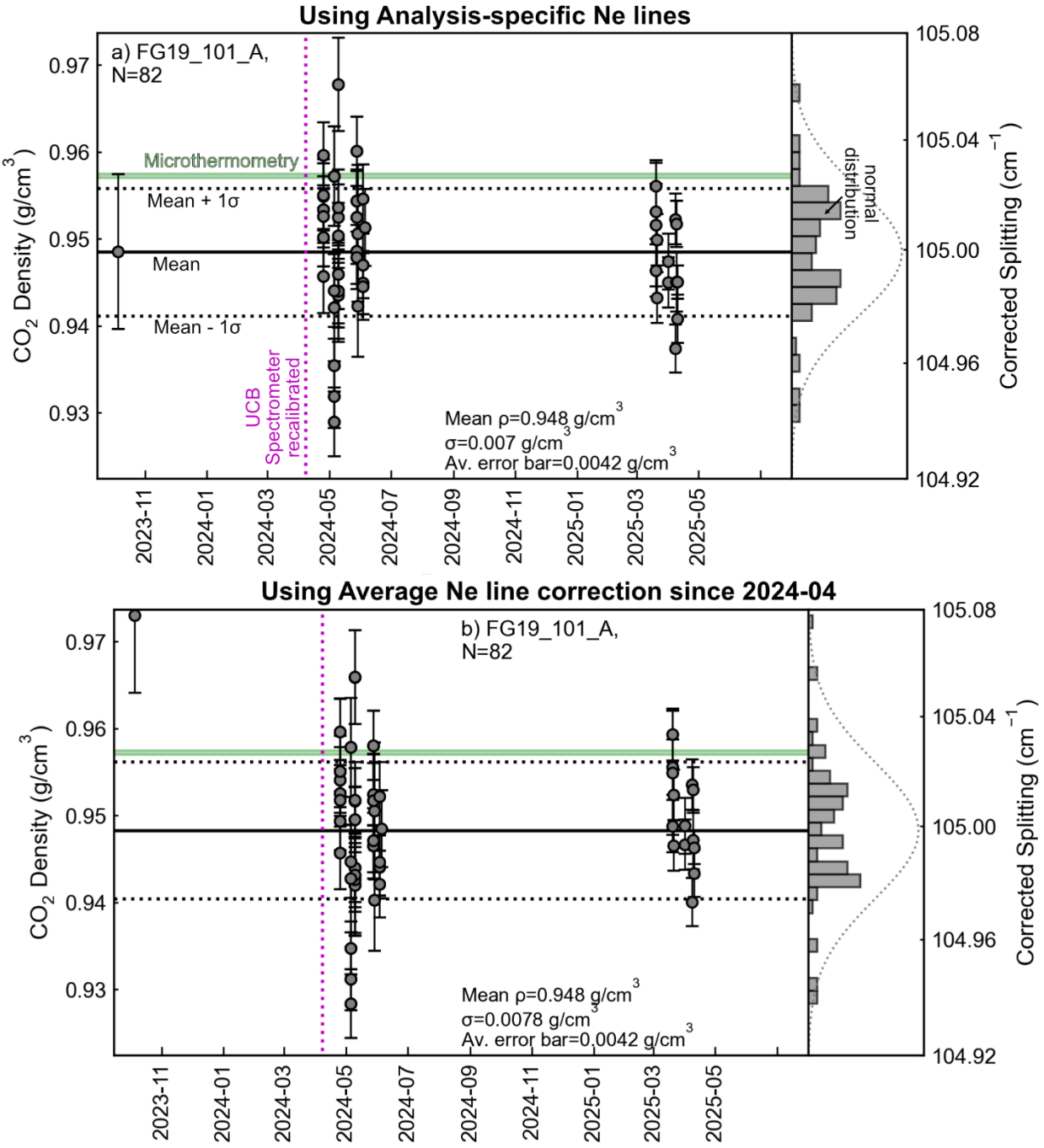

Supporting Figure 2 - Long-term variability in standard values collected at UCB. a) Data reduced using a drift correction model for each analytical session. b) Data reduced using the average Neon line correction factor for all standard acquisitions after the instrument recalibration (marked with a magenta line). The green bar shows the density determined by Microthermometry, accounting

for the uncertainty in the temperature reading of the stage. The black solid line shows the mean Raman value for the standard, and the dotted black lines ±1 σ. The distribution of densities is shown as a histogram, compared to a normal distribution based on the mean and standard deviation

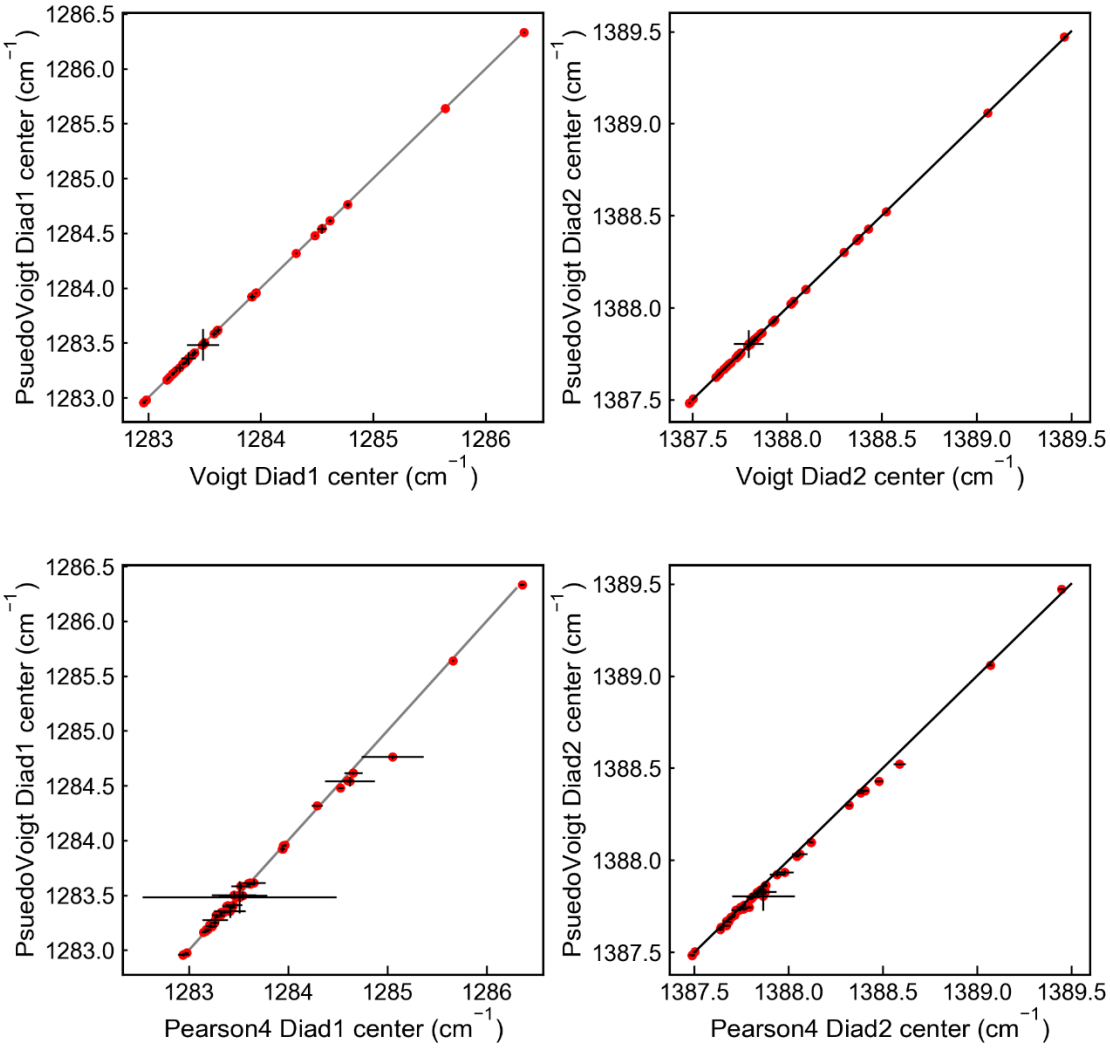

Supporting Figure 3 – Comparison of different PDF fits for Fogo fluid inclusions (as for Fig 8 in the main text).

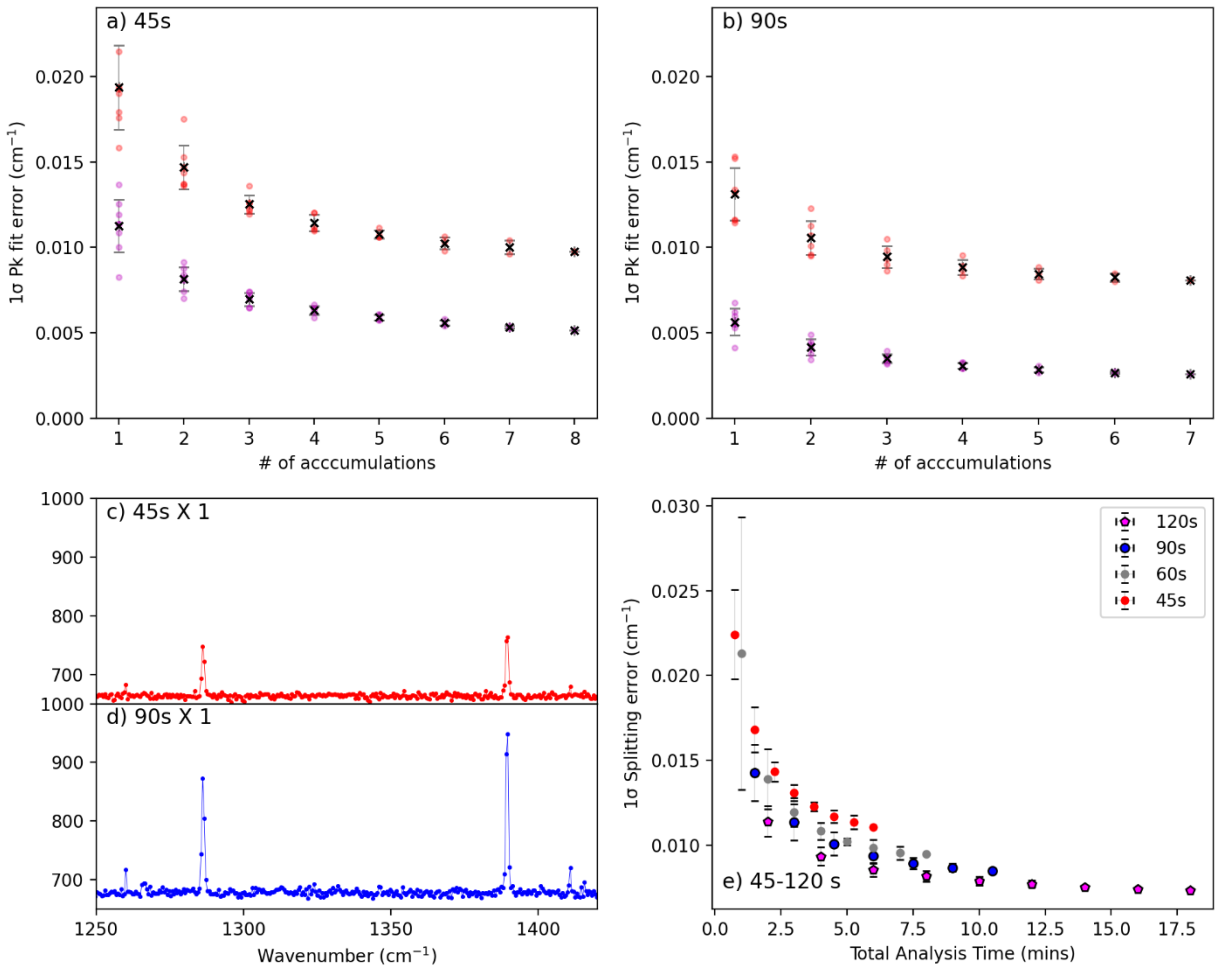

Supporting Figure 4 – Investigating peak fitting error as a function of integration time and accumulations using a melt inclusion vapour bubble from Mauna Loa (~0.01 g/cm^3, (Bearden et al., 2025). a-b) Error on the peak position of diad1 and diad2 for 45 and 90s acquisitions. The x axis shows the number of spectra that were averaged prior to fitting the peaks (analogous to accumulation). The dots show an individual fitted spectra (e.g. spectra 1 to 14 for accumulations =1, average of spectra 1-2, 2-3 3-4 for n=2 accumulations etc.), and the cross and error bar show the mean and standard deviation of averaged spectra for each number of accumulations (e.g. 14 individually fitted spectra for n=1 accumulations). c-d) Example spectra for 45s x 1 and 90s x 1. e) Error on calculated splitting after combining different numbers of individual acquisitions to give different acquisition times. For example, 5 different 120s acquisitions were averaged for the 10 minute total acquisition time.

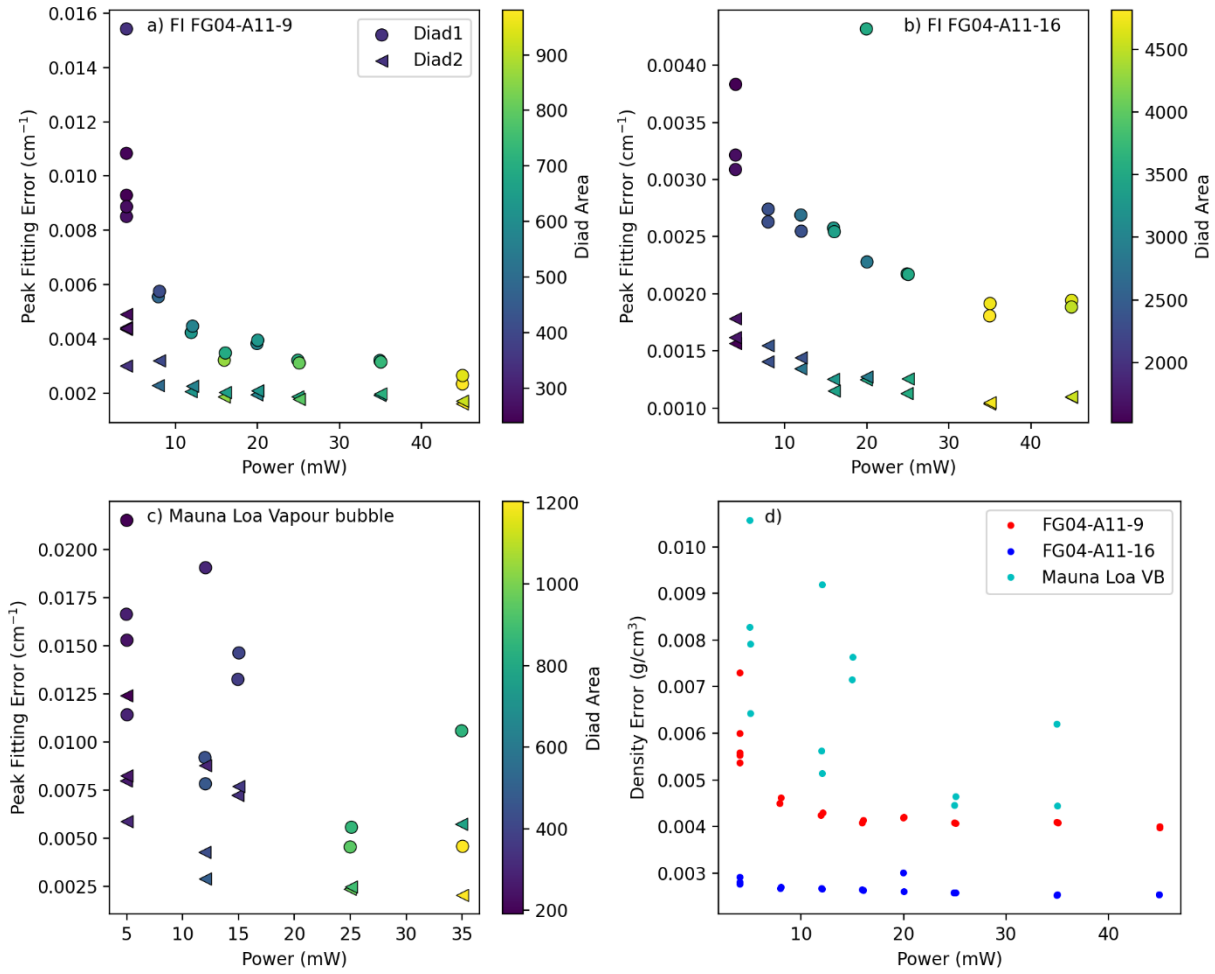

Supporting Figure 5– Change in peak fitting errors with increasing laser power. a-b) There is a clear drop in the peak fitting error for diad1 and diad2 as laser power is increased for Fogo fluid inclusion (FG04-A11-9), and for a melt inclusion vapour bubble from Mauna Loa (c). d) Same datasets but showing the error in calculated density.

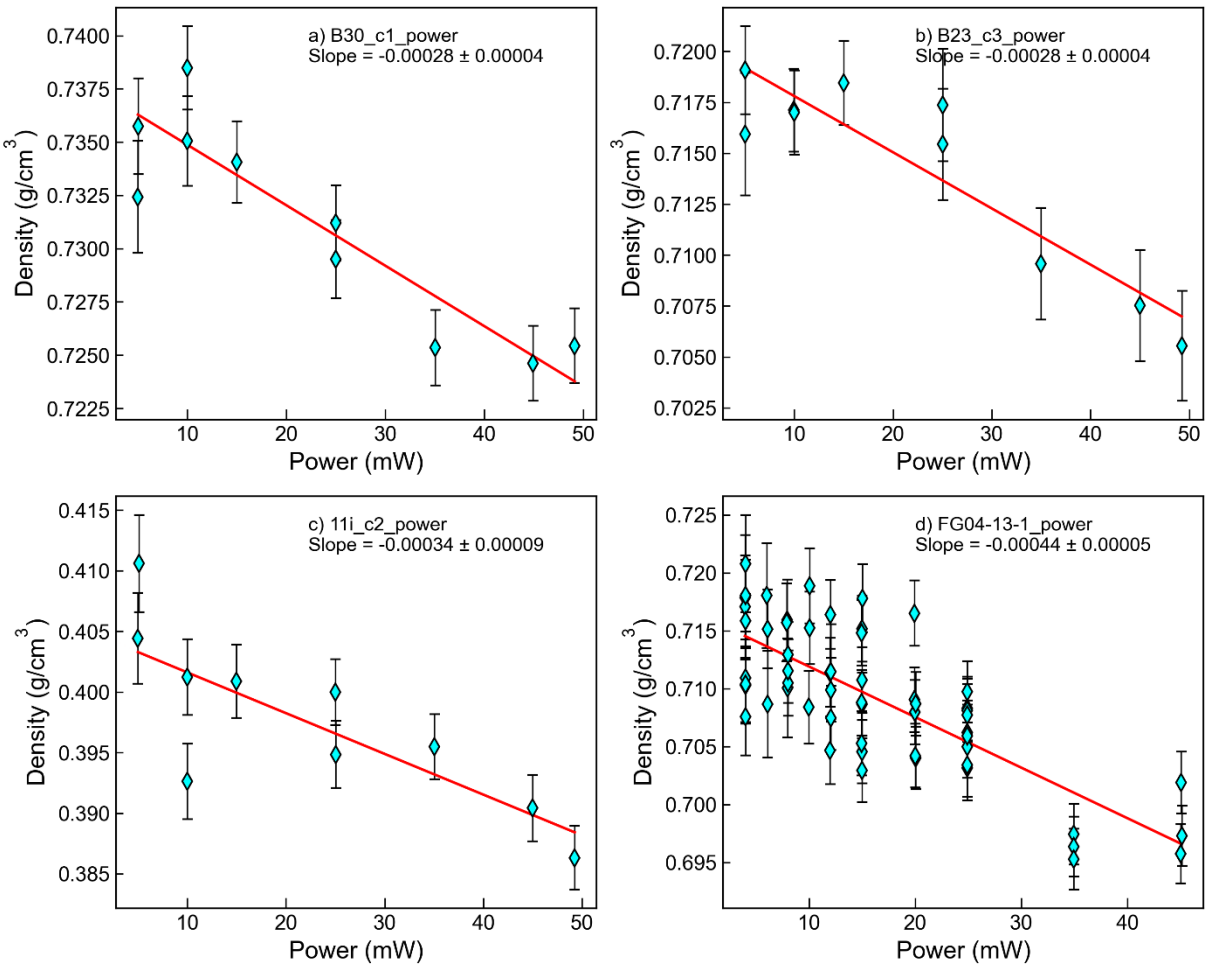
a) B30_c1_power
Slope = -0.00028 ± 0.00004
b) B23_c3_power
Slope = -0.00028 ± 0.00004
c) 11i_c2_power
Slope = -0.00034 ± 0.00009
d) FG04-13-1_power
Slope = -0.00044 ± 0.00005
Density (g/cm3)
Power (mW)

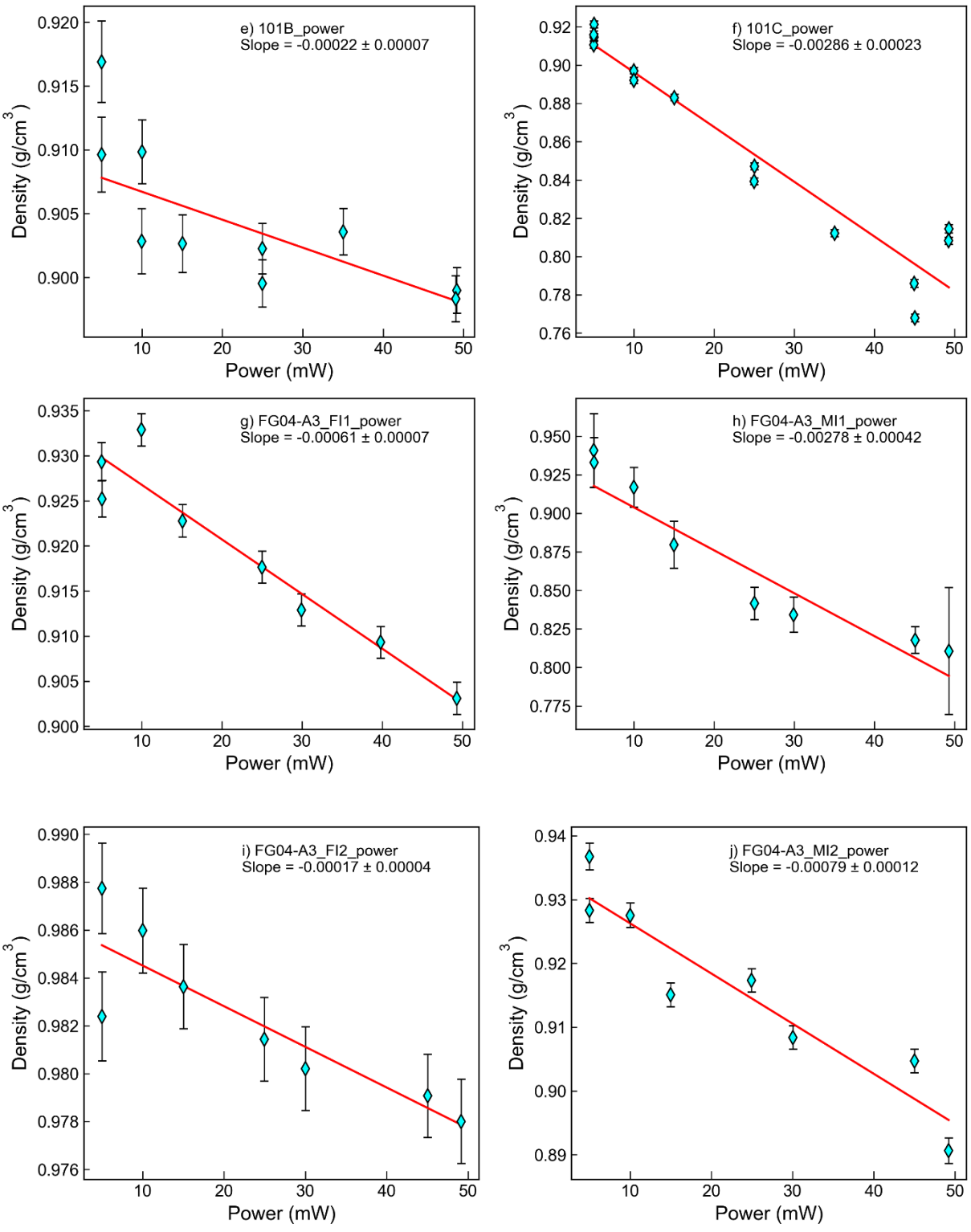

Supporting Figure 6 – Power series for 10 FI/MI, 4 of which are shown in Fig. 13 of the main text. The gradient and error on the slope is shown.

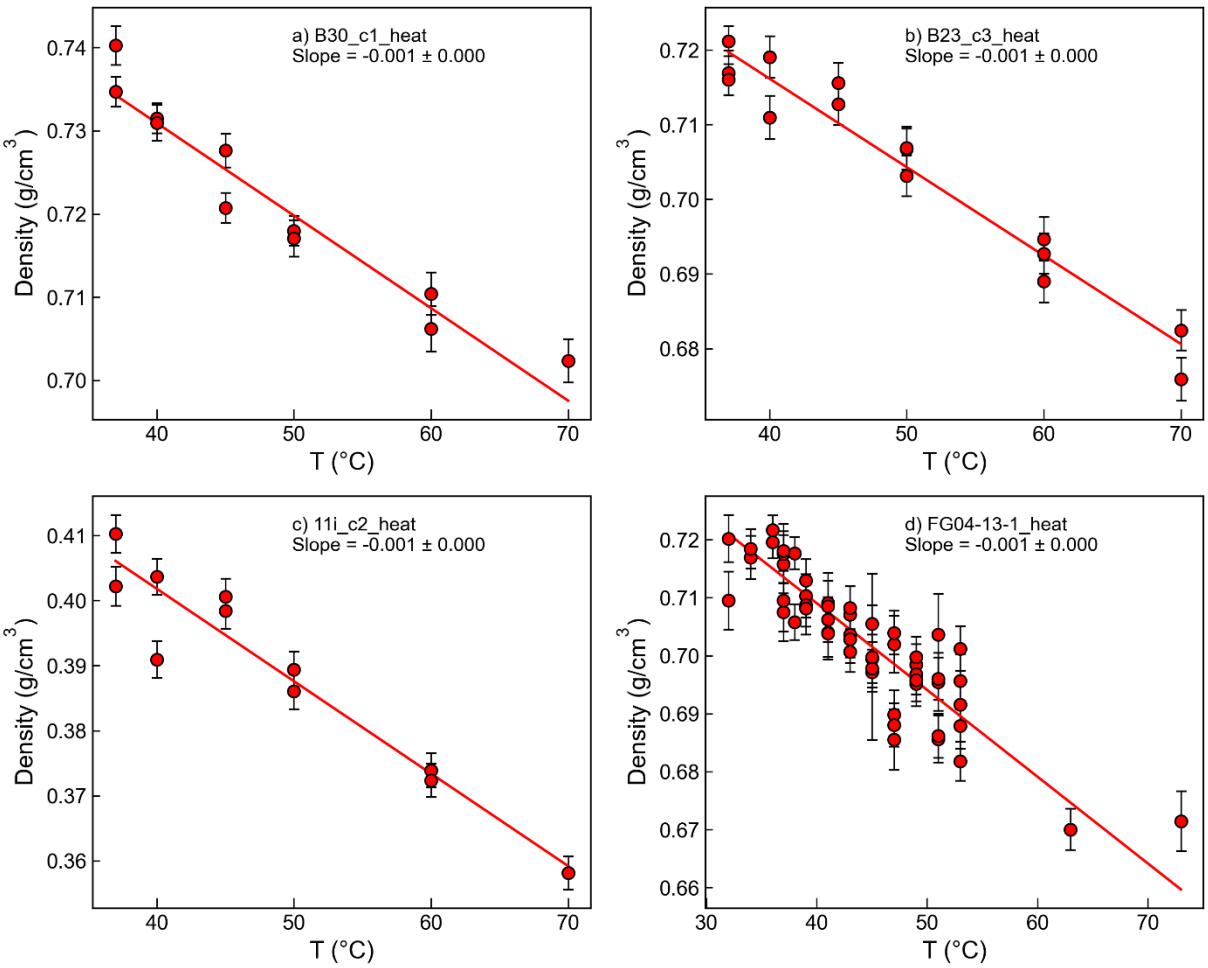
a) B30_c1_heat
Slope = -0.001 ± 0.000
b) B23_c3_heat
Slope = -0.001 ± 0.000
c) 11i_c2_heat
Slope = -0.001 ± 0.000
d) FG04-13-1_heat
Slope = -0.001 ± 0.000
Density (g/cm3)
T (°C)

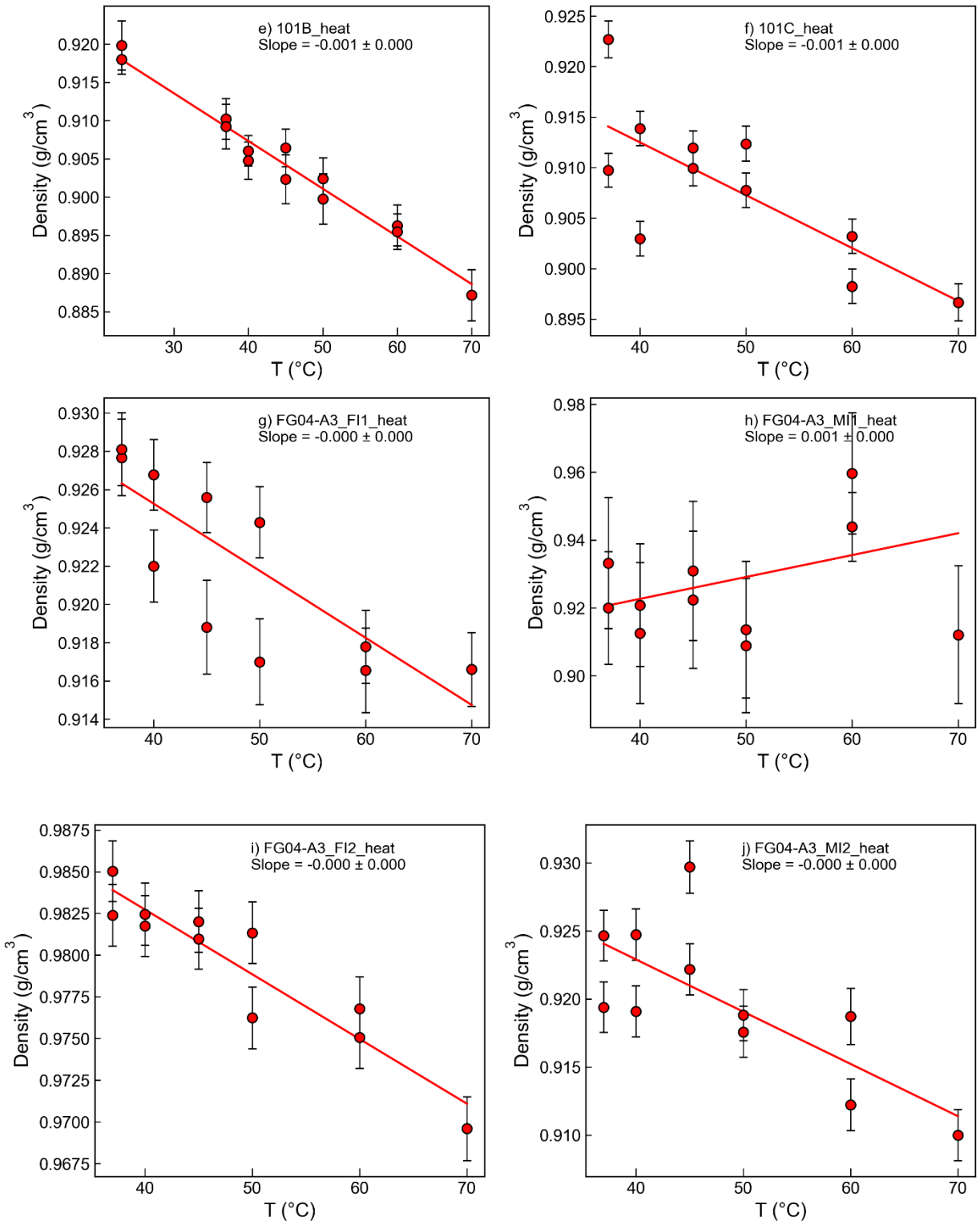

Supporting Figure 7 – Heating series for 10 FI/MI, 4 of which are shown in Fig. 13 of the main text. The gradient and error on the slope is shown.

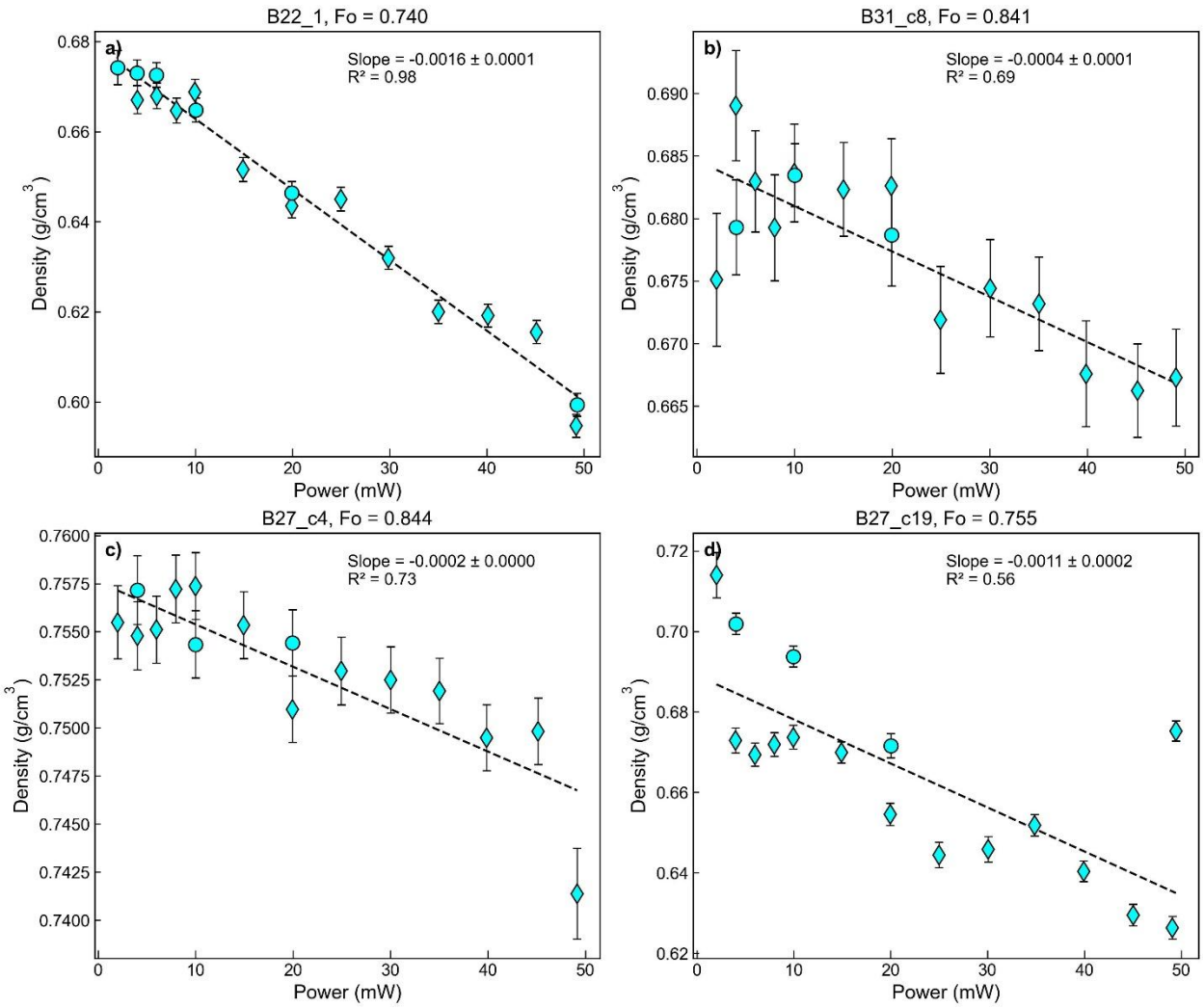
B22_1, Fo = 0.740
a)
Slope = -0.0016 ± 0.0001
R² = 0.98
Density (g/cm 3)
Power (mW)
B31_c8, Fo = 0.841
b)
Slope = -0.0004 ± 0.0001
R² = 0.69
Density (g/cm 3)
Power (mW)
B27_c4, Fo = 0.844
c)
Slope = -0.0002 ± 0.0000
R² = 0.73
Density (g/cm 3)
Power (mW)
B27_c19, Fo = 0.755
d)
Slope = -0.0011 ± 0.0002
R² = 0.56
Density (g/cm 3)
Power (mW)

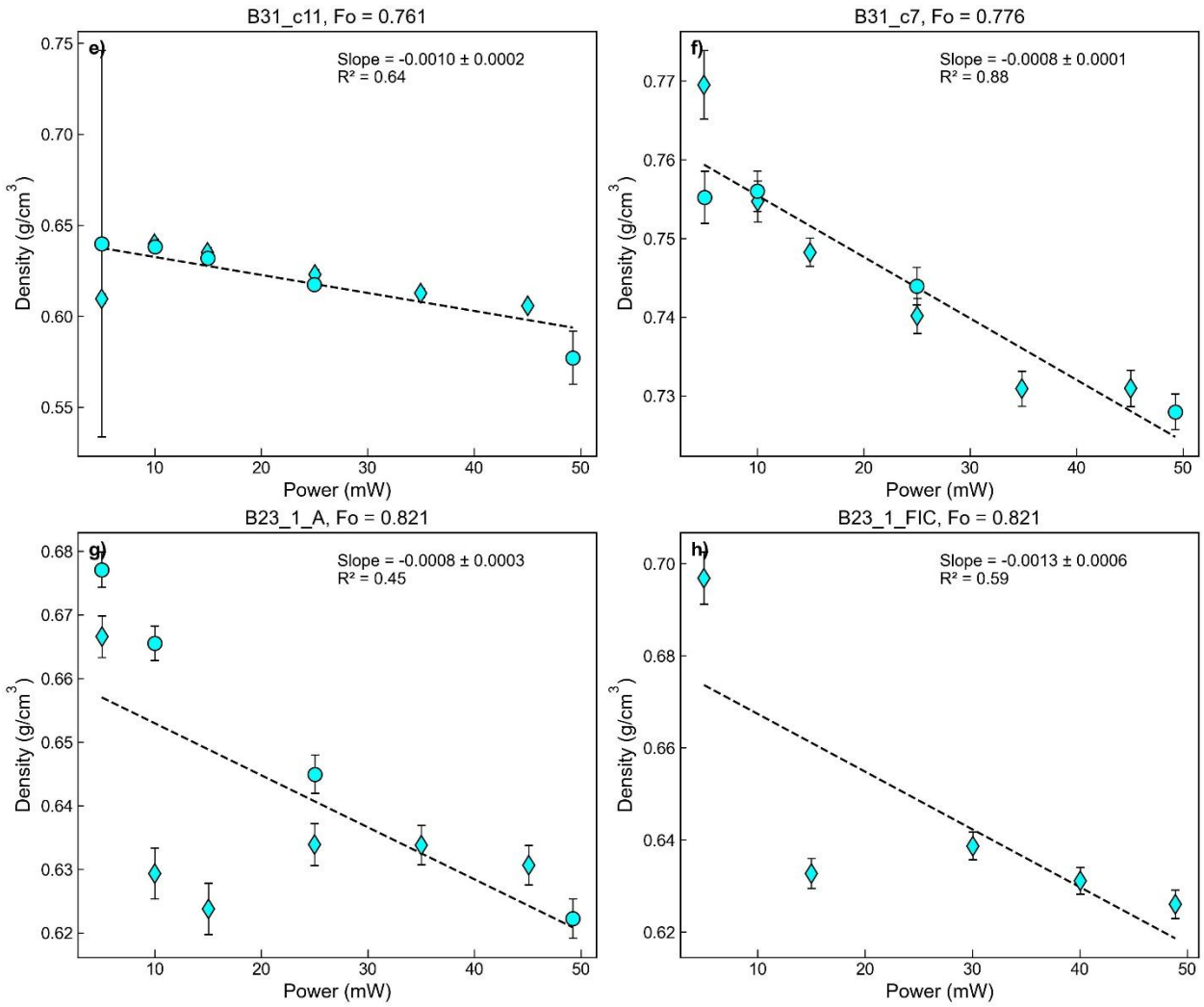

Supporting Figure 8 – Power series for Icelandic fluid inclusions with known Fo contents. The gradient, Fo content, and R^2 value is shown.

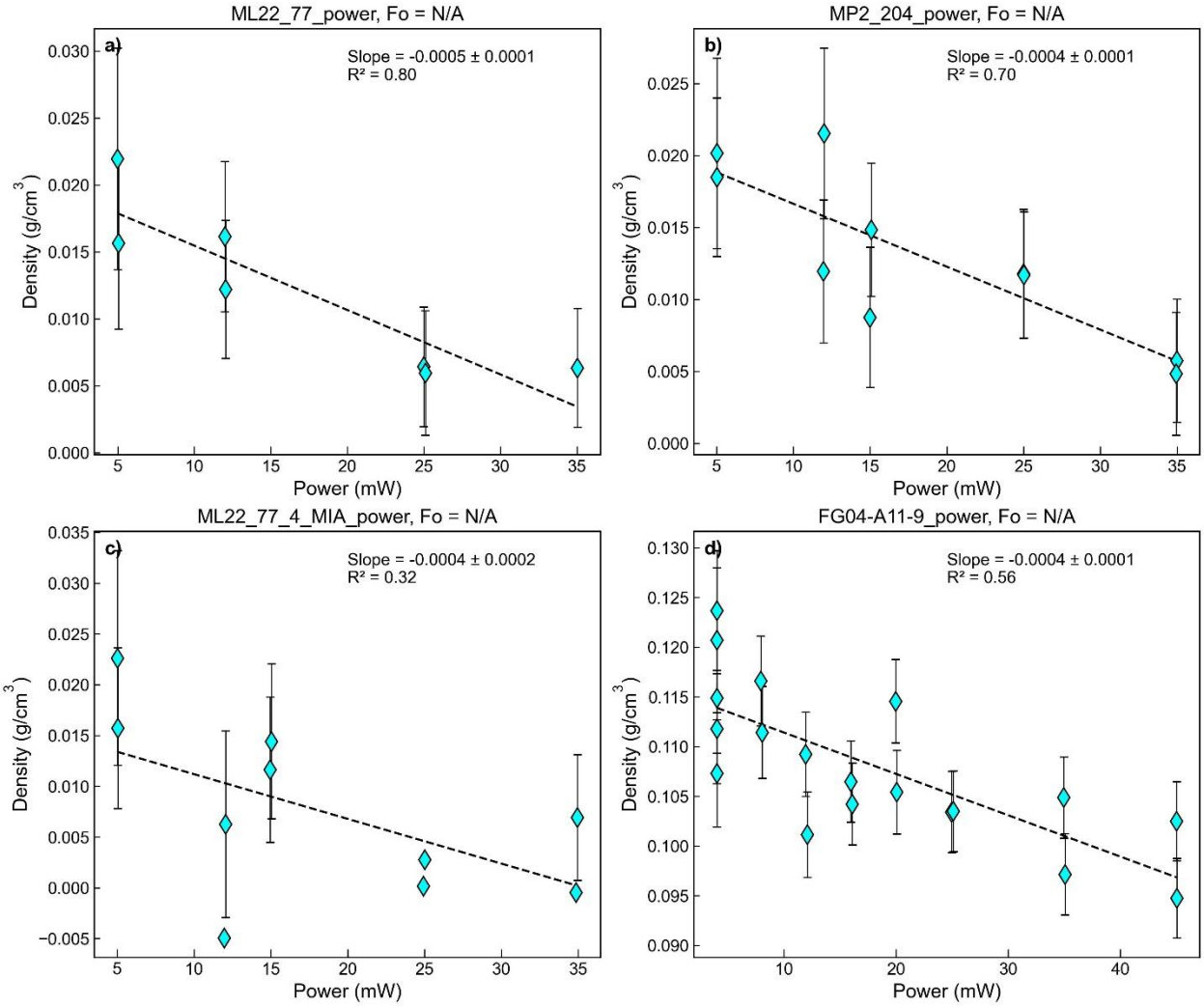
ML22_77_power, Fo = N/A
a)
Slope = -0.0005 ± 0.0001
R² = 0.80
Density (g/cm 3)
Power (mW)
MP2_204_power, Fo = N/A
b)
Slope = -0.0004 ± 0.0001
R² = 0.70
Density (g/cm 3)
Power (mW)
ML22_77_4_MIA_power, Fo = N/A
c)
Slope = -0.0004 ± 0.0002
R² = 0.32
Density (g/cm 3)
Power (mW)
FG04-A11-9_power, Fo = N/A
d)
Slope = -0.0004 ± 0.0001
R² = 0.56
Density (g/cm 3)
Power (mW)

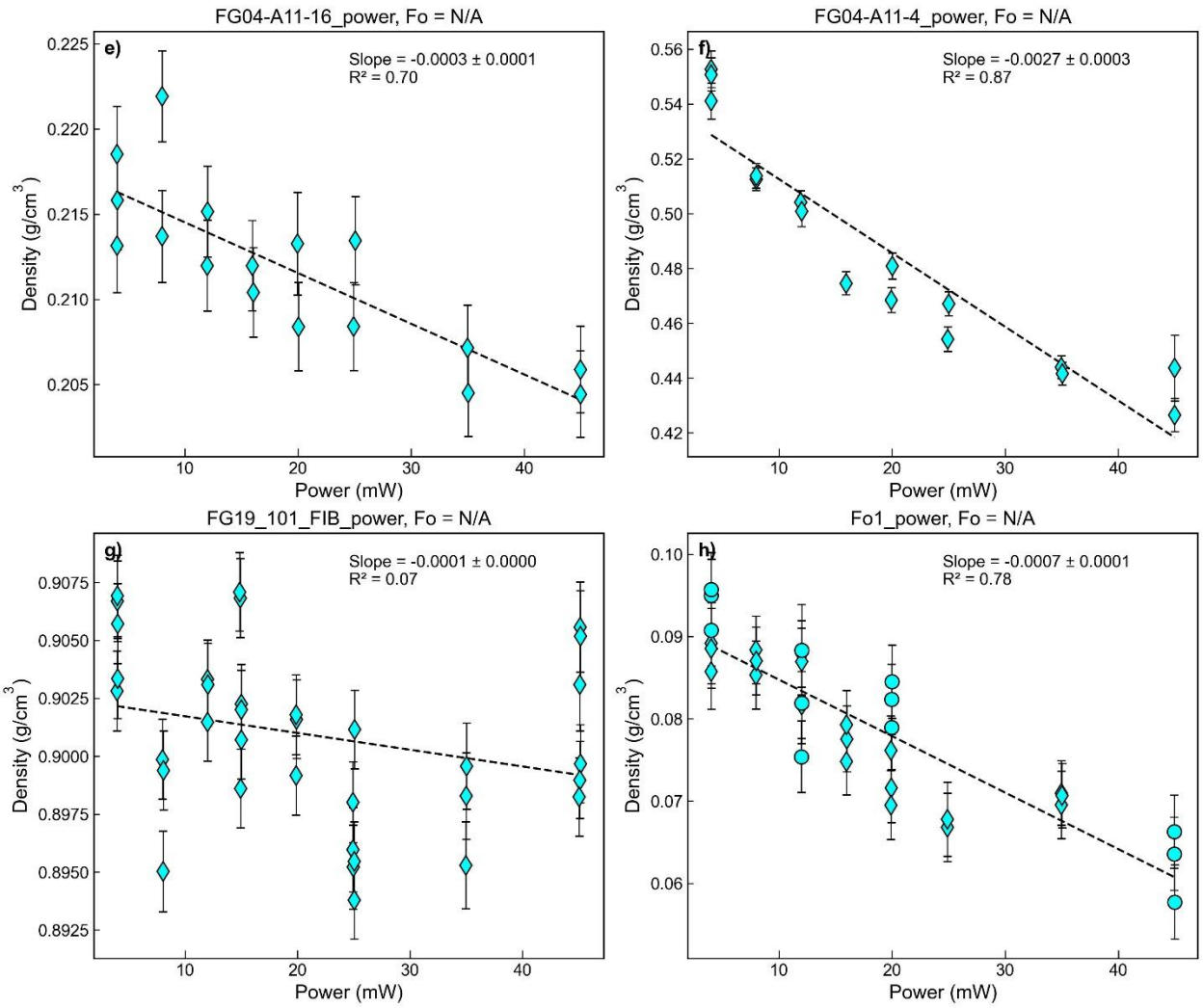
FG04-A11-16_power, Fo = N/A
e)
Slope = -0.0003 ± 0.0001
R² = 0.70
Density (g/cm³)
Power (mW)
FG04-A11-4_power, Fo = N/A
f)
Slope = -0.0027 ± 0.0003
R² = 0.87
Density (g/cm³)
Power (mW)
FG19_101_FIB_power, Fo = N/A
g)
Slope = -0.0001 ± 0.0000
R² = 0.07
Density (g/cm³)
Power (mW)
Fo1_power, Fo = N/A
h)
Slope = -0.0007 ± 0.0001
R² = 0.78
Density (g/cm³)
Power (mW)

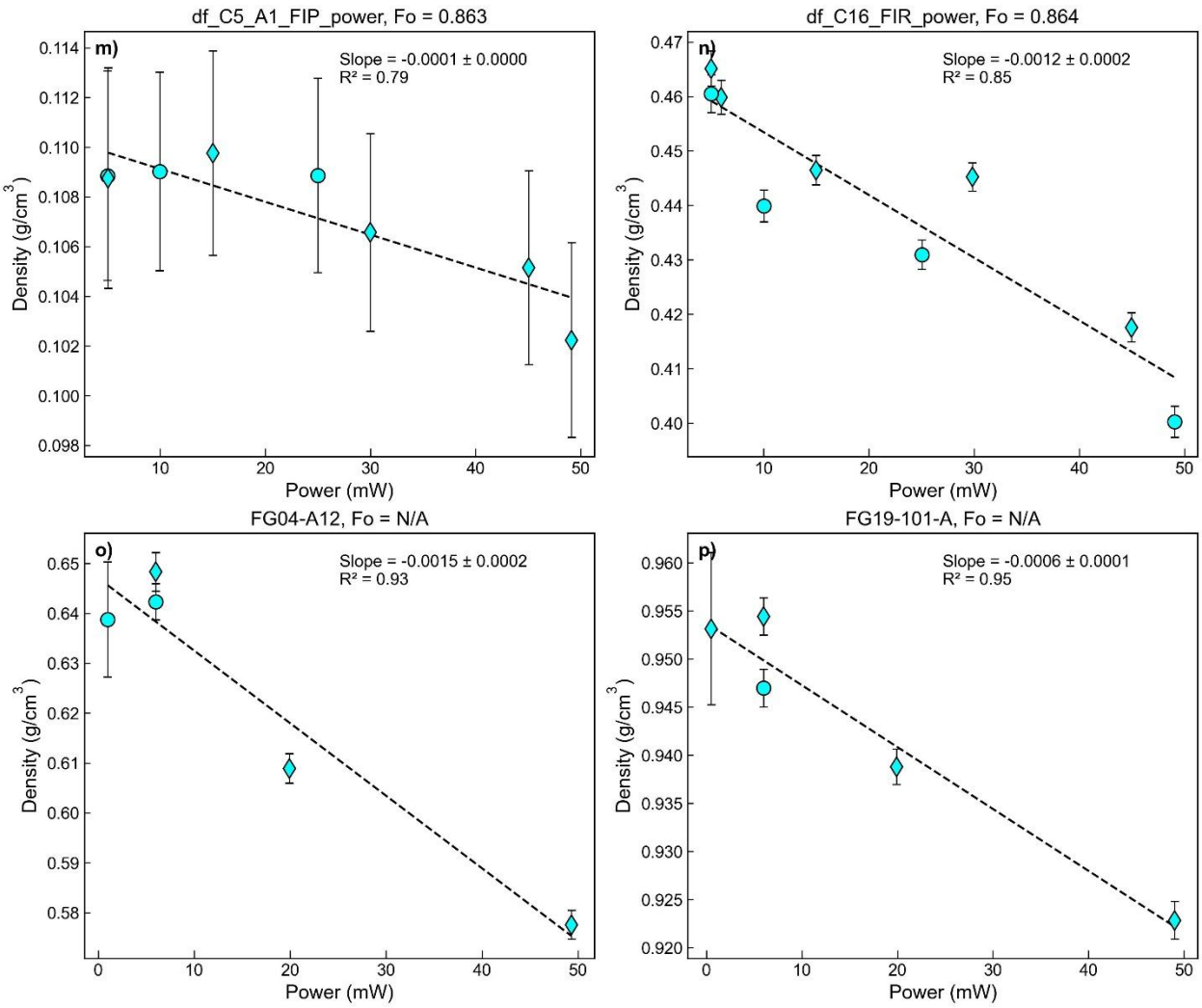
df_C5_A1_FIP_power, Fo = 0.863
m)
Slope = -0.0001 ± 0.0000
R² = 0.79
Density (g/cm 3)
Power (mW)
df_C16_FIR_power, Fo = 0.864
n)
Slope = -0.0012 ± 0.0002
R² = 0.85
Density (g/cm 3)
Power (mW)
FG04-A12, Fo = N/A
o)
Slope = -0.0015 ± 0.0002
R² = 0.93
Density (g/cm 3)
Power (mW)
FG19-101-A, Fo = N/A
p)
Slope = -0.0006 ± 0.0001
R² = 0.95
Density (g/cm 3)
Power (mW)

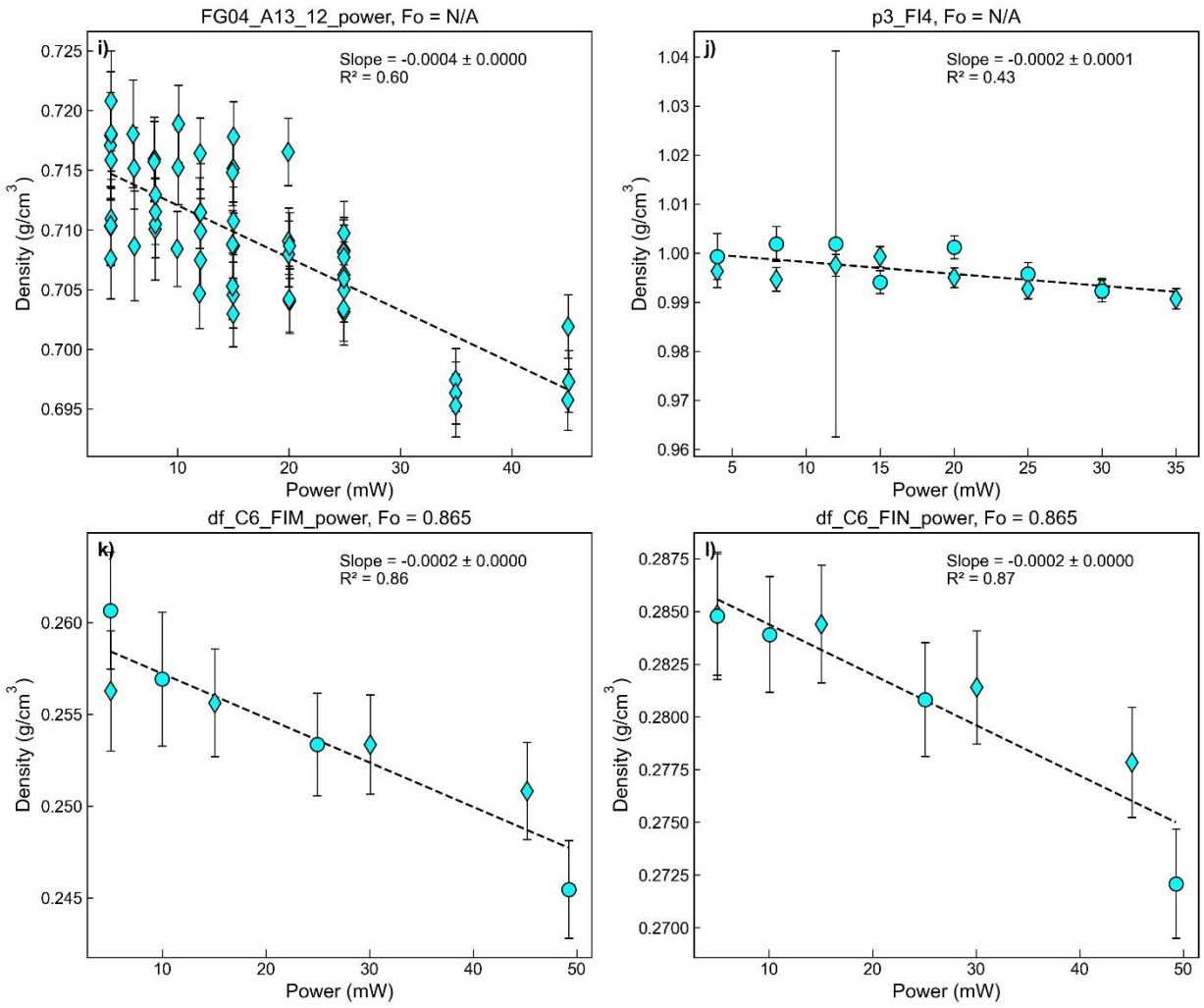

Supporting Figure 9 – Power series for all other fluid inclusions, and melt inclusions (a, b, c, h) shown in Fig. 12a of the main text.

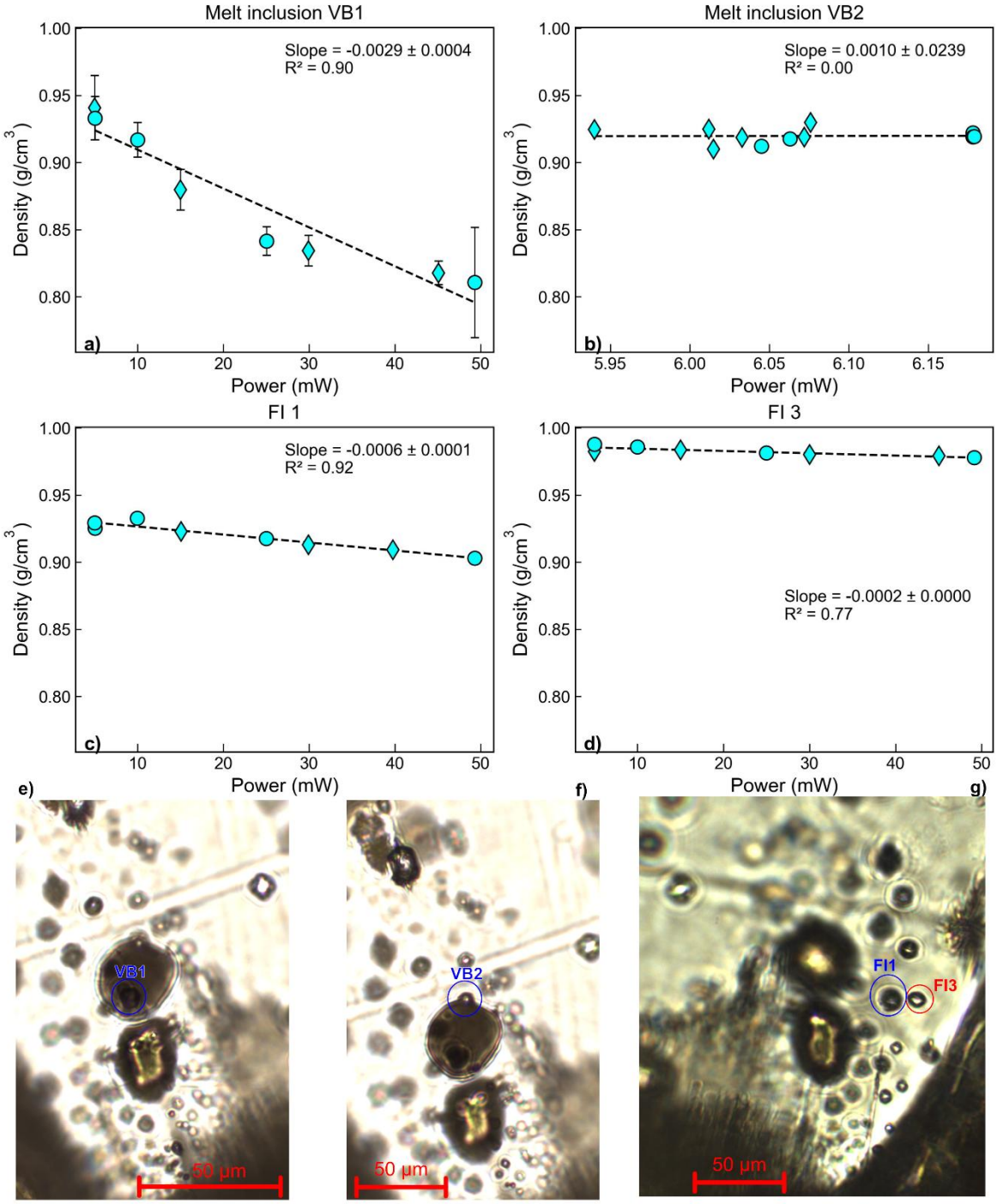

Supporting Figure 10 – Comparison of change in density as a function of laser power for two melt inclusion vapour bubbles and two fluid inclusions within the same crystal. VB1 is surrounded by melt (e) while VB2 is partially touching melt and partially touching olivine (f, see Supporting Fig. 11). The fact that VB2 is surrounded by olivine and melt accounts for its lower heating rate compared to VB1. It is noteworthy that the two FI, despite being in close proximity, show gradients that differ by a factor of 3.

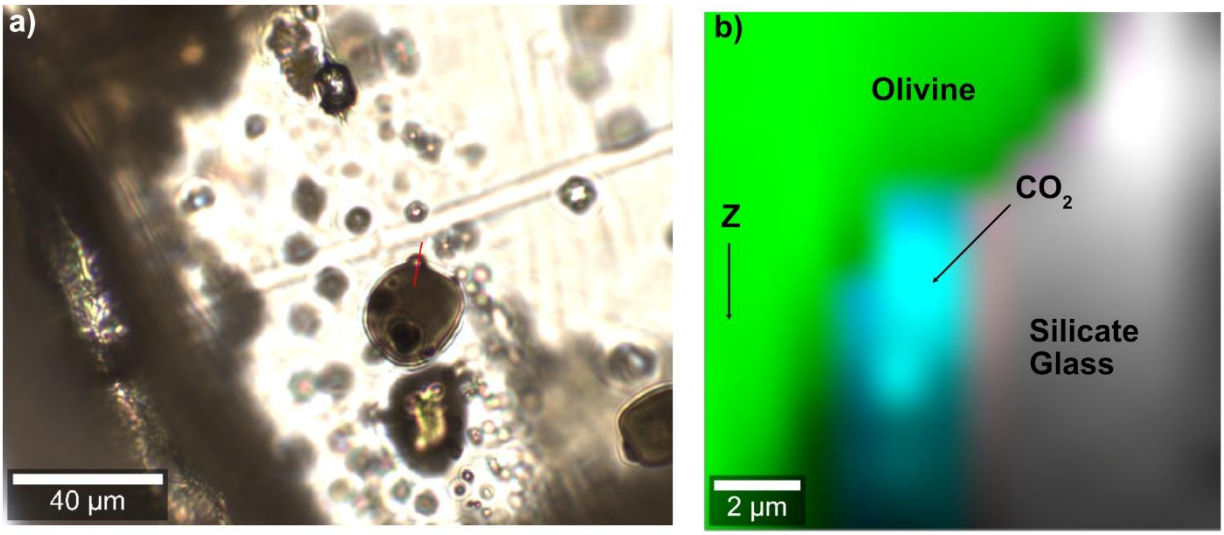

Supporting Figure 11 – a) Transmitted light image of Bub2, with the red line showing the location of a vertical Raman map. b) Processed Raman map, showing that the bubble is partially touching the silicate glass of the melt inclusion (grey colors), partially touching the olivine (green). Map processed using the WITec software.

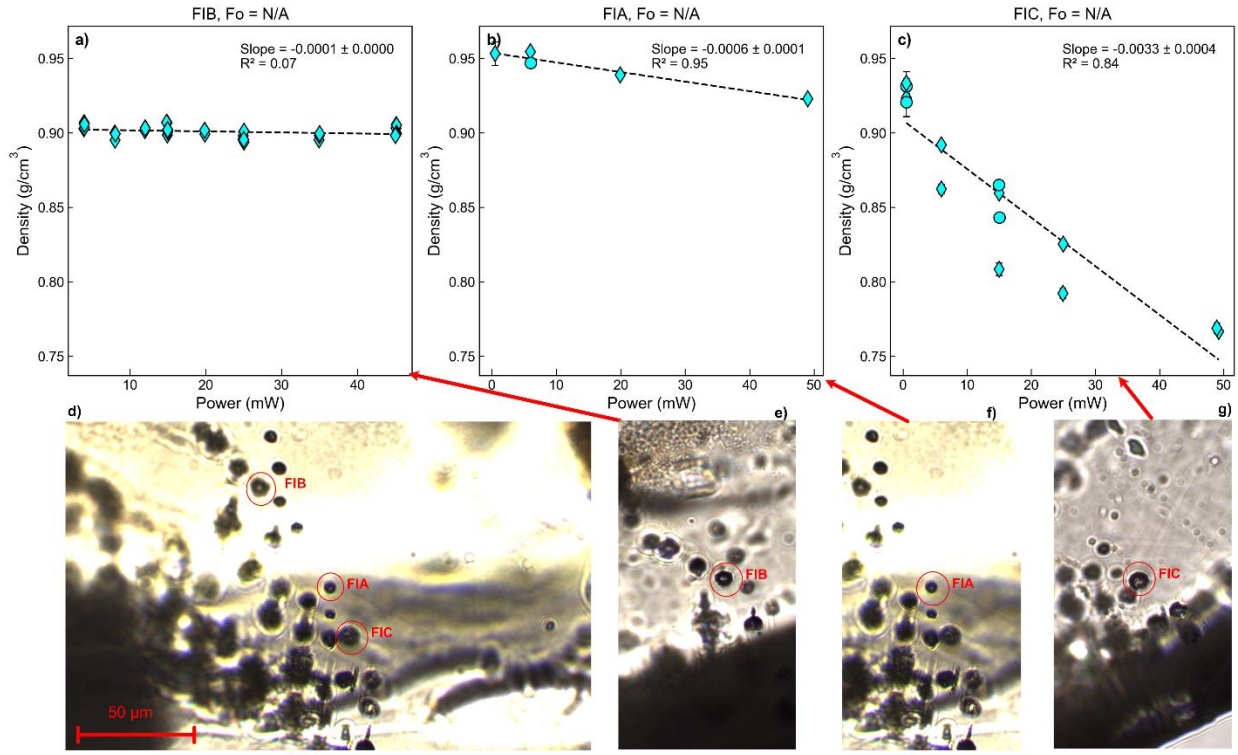

Supporting Figure 12. Comparison of change in density with increasing laser power (a-c) for 3 FI hosted within a single olivine crystal (FG19_101). d) Transmittted light image of the fluid

inclusion trail and the location of each FI. e-g) shows a focused picture of each FI. The scale is the same for all pictures. Raman maps of A and C are shown in Supporting Figure 14.

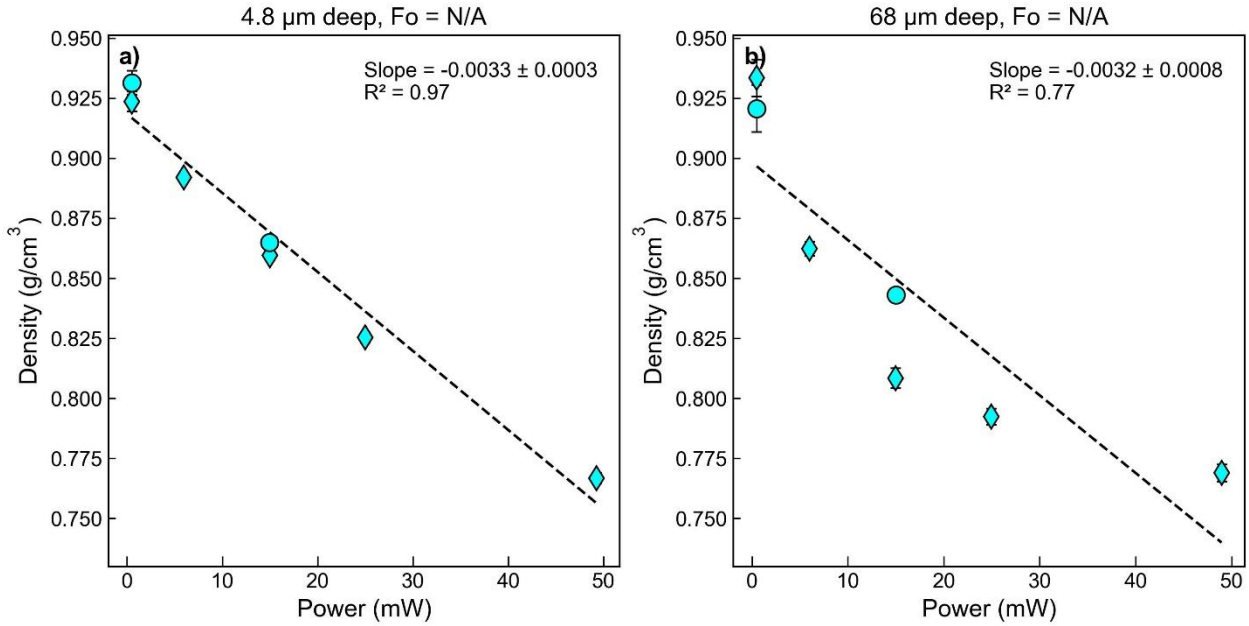

Supporting Figure 13 – Comparison of change in density with increasing laser power for FI FG19-101C at two different depths below the surface a) Collected when the FI was ~4.8 µm below the surface. The crystal was then flipped over, and a second power series conducted (The FI was ~68 µm below the top surface). The gradients of these series are within error of each other. This supports the modelling work of Hagiwara et al. (2021) suggesting that depth in the sample doesn't strongly affect heating rate.

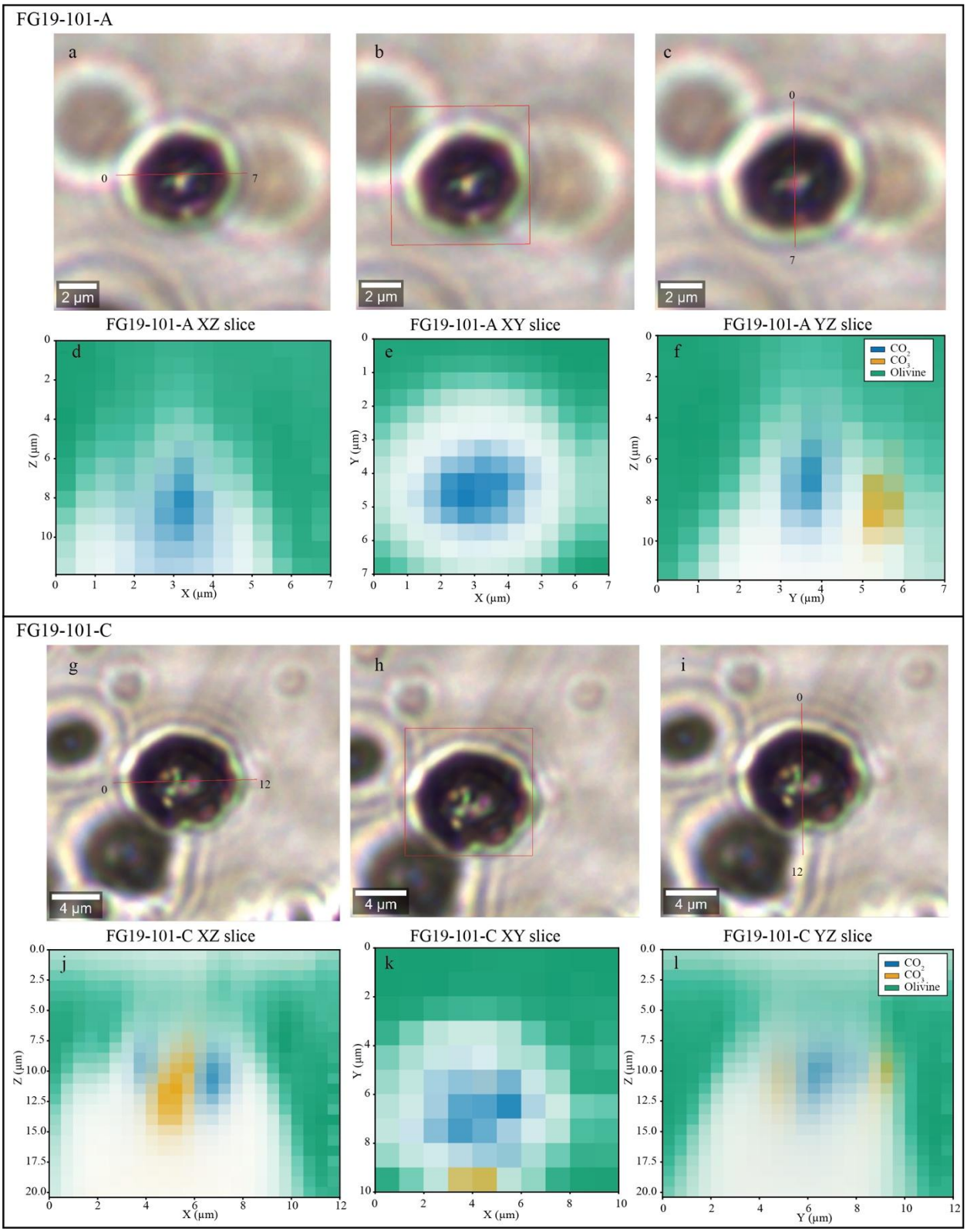

Supporting Fig. 14. Two dimensional Raman maps of FIA and FIc show the presence of CO_2 and carbonate a-c) Transmitted light images of FG19-101-A. The red lines and rectangles show the plane along which Raman mapping was conducted (shown in panels d-f). g-i) Transmitted

light images of FG19-101-A and corresponding 2D slice (red line) . It is evident that carbonate is much more abundant in 101-C than 101-A, though they are only ~20 um apart from each other (Supporting Fig. 11). Both sets of Raman maps were collected using 50X objective, with a laser power of 49 mW, an integration time of 0.5 s, a 300 grooves/mm grating, and a 2350 cm-1 spectral center. Z dimension was recalculated accounting for the refraction index of olivine (1.7). In the Z slices, the bottom under the inclusions is white (very low intensity) due to loss of confocality at depth. Other white pixels are areas of highly mixed spectra which are difficult to reliably extract components from. Maps were processed using Ramanspy 0.2.10 (Georgiev et al., 2024). To produce the maps, we first denoise using savitzky golay filter with a window length of 4, and a polynomial of 3rd order, then apply ASLS baseline routine in Ramanspy and normalize each spectrum to using Min-Max normalization. We apply the whole preprocessing routine to all the maps. We extract “pure” endmember spectra for CO_2, CO_3 and Olivine from the map spectra and use Non-negative Constrained Least Squares (NNLS) abundance method in RamanSpy to extract abundance maps for each component at every pixel. These maps are not quantitative, but an approximation of the distribution of each component

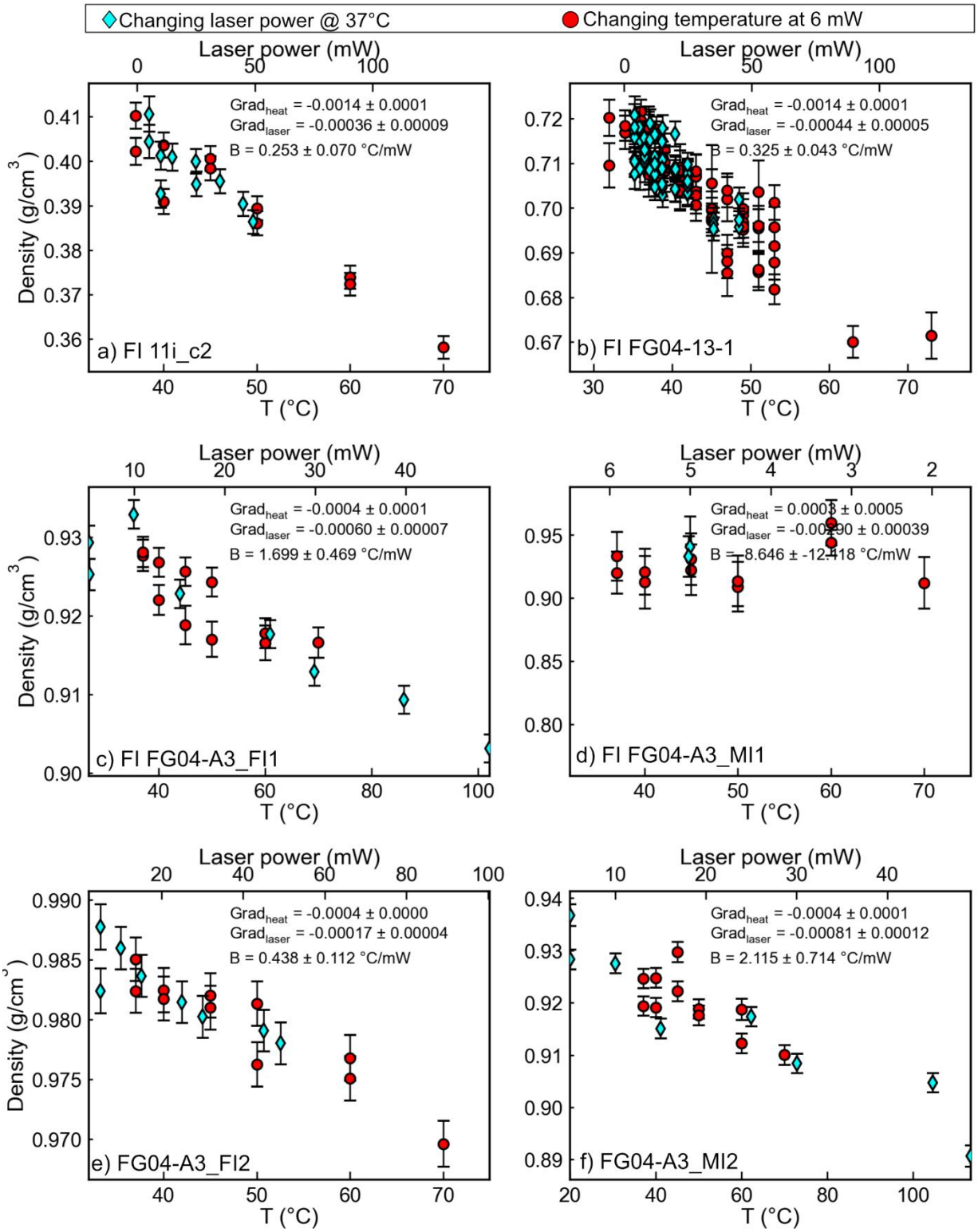

Supporting Figure 15 – Comparison of heating and power series for additional samples to those shown in Fig. 13 of the main text.

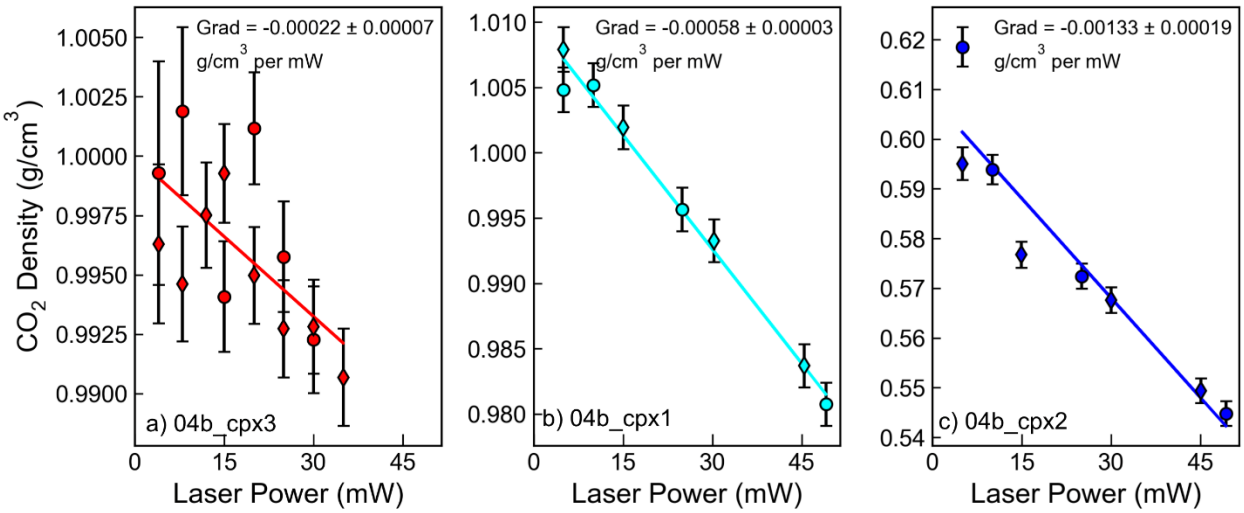

Supporting Figure 16 – Laser power series for ~Mg_{79}# clinopyroxenes for fluid inclusions from Gleeson et al. (2025). The gradient varies by a factor of ~3.8, despite the fact these samples are very chemically homogenous and there are no obvious color differences between the different crystals.

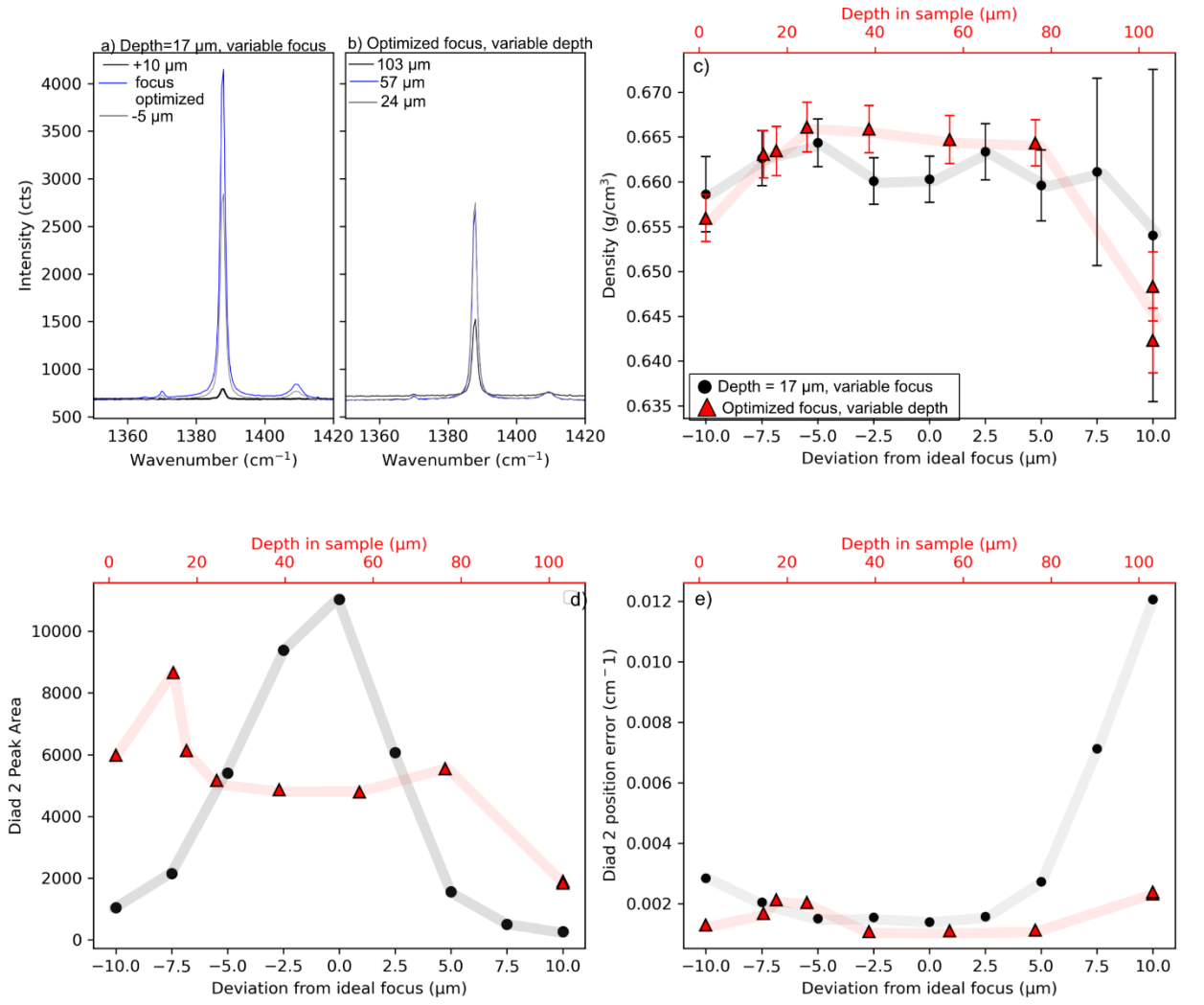

Supporting Figure 17 – Comparison of peak intensity and peak fitting errors with increasing depth in sample vs. a change in focus for FG04_A12. a) Spectra centered around diad2 showing the difference in intensity for the optimized focus (blue) vs. -5 µm deeper in the sample (grey) and 10 µm shallower (black). The fluid inclusion has a radius of ~7 µm. b) Change in intensity with depth of the fluid inclusion optimal focus below the sample. At 24 µm and 57 µm depth, the intensities are very similar, although they drop to above half for 103 µm depth. c) Change in density as a function of depth and ideal focus. Red triangles show variation in depth in sample (top red axis) and black circles show deviation from the ideal focus (black). Apart from the very worst focus and deepest depth, there is no change outside of uncertainty. Points are joined up with lines to help separate the two series. d) Peak area of diad 2 (a measure of intensity) as a function of depth and focus. e) Error on the position of diad 2.

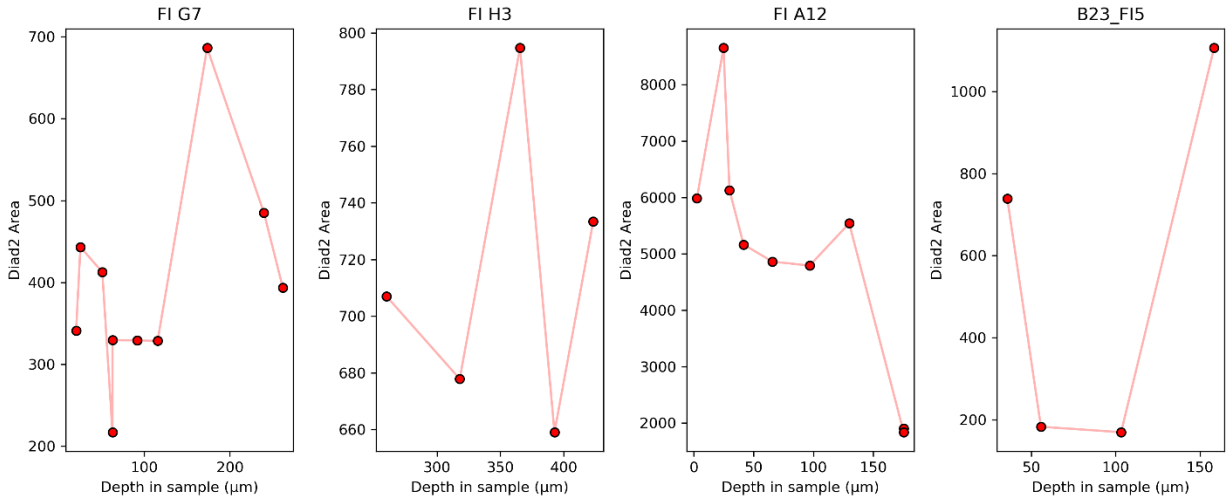

Supporting Figure 18 – Changes in signal intensity as a function of depth of the FI below the sample for 4 different olivine-hosted FI. FI H3 was lost during serial sectioning, hence the shorter range of depths.

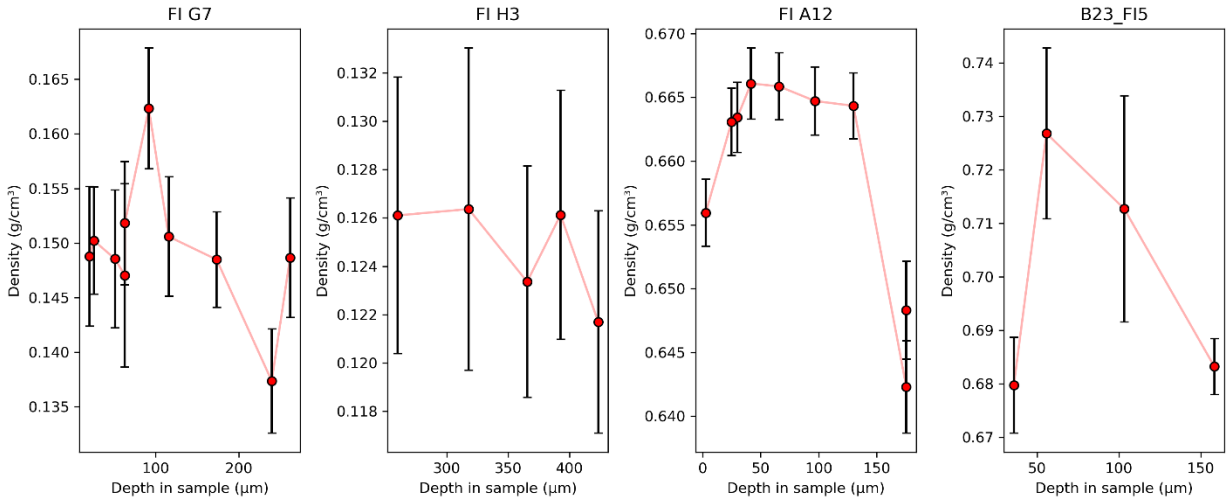

Supporting Figure 19- Density (and error) as a function of depth. The highly variable densities in B23_FI5 likely result from the very poor surface polish, resulting in backgrounds which were tricky to fit.

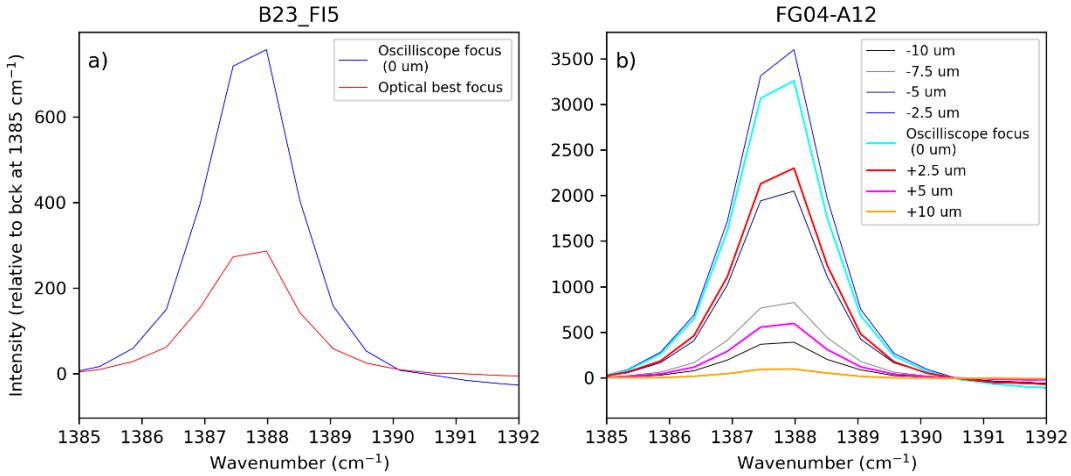

Supporting Figure 20 – Example of the effect of small focus changes on the intensity of diad 2. a) Compares the user-selected optical focus based on sharpness of the FI edges to the optimal focus position found by the oscilloscope. b) Compares the optimal focus position found by the oscilloscope to small perturbations from this position.

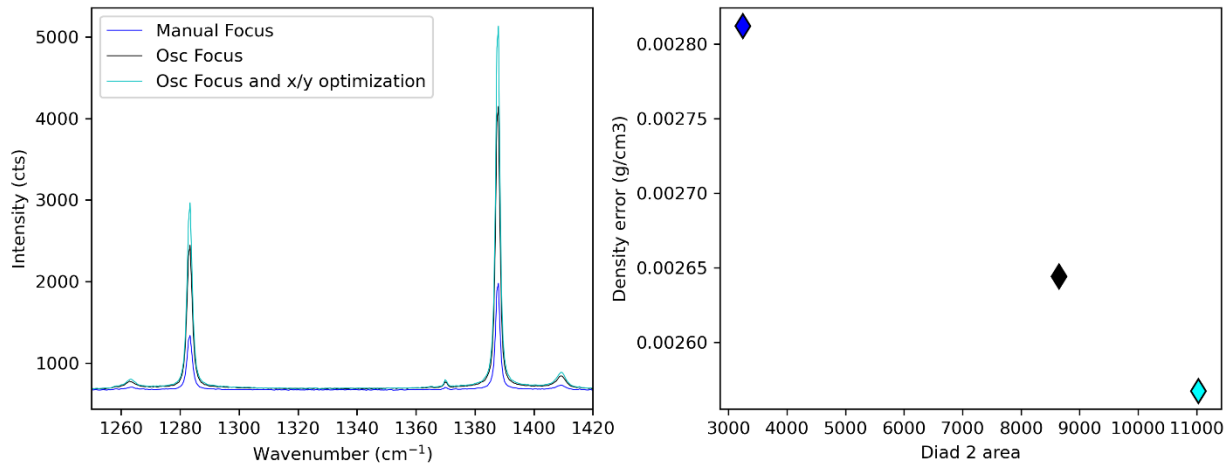

Supporting Fig. 21– Compares the user-selected optical focus based on sharpness of the FI edges to the optimal focus position found by the oscilloscope (dark blue), to the optimum Z position found by the oscilloscope (black), and the optimum Z and x-y position determined by Raman mapping for FG04-A12.

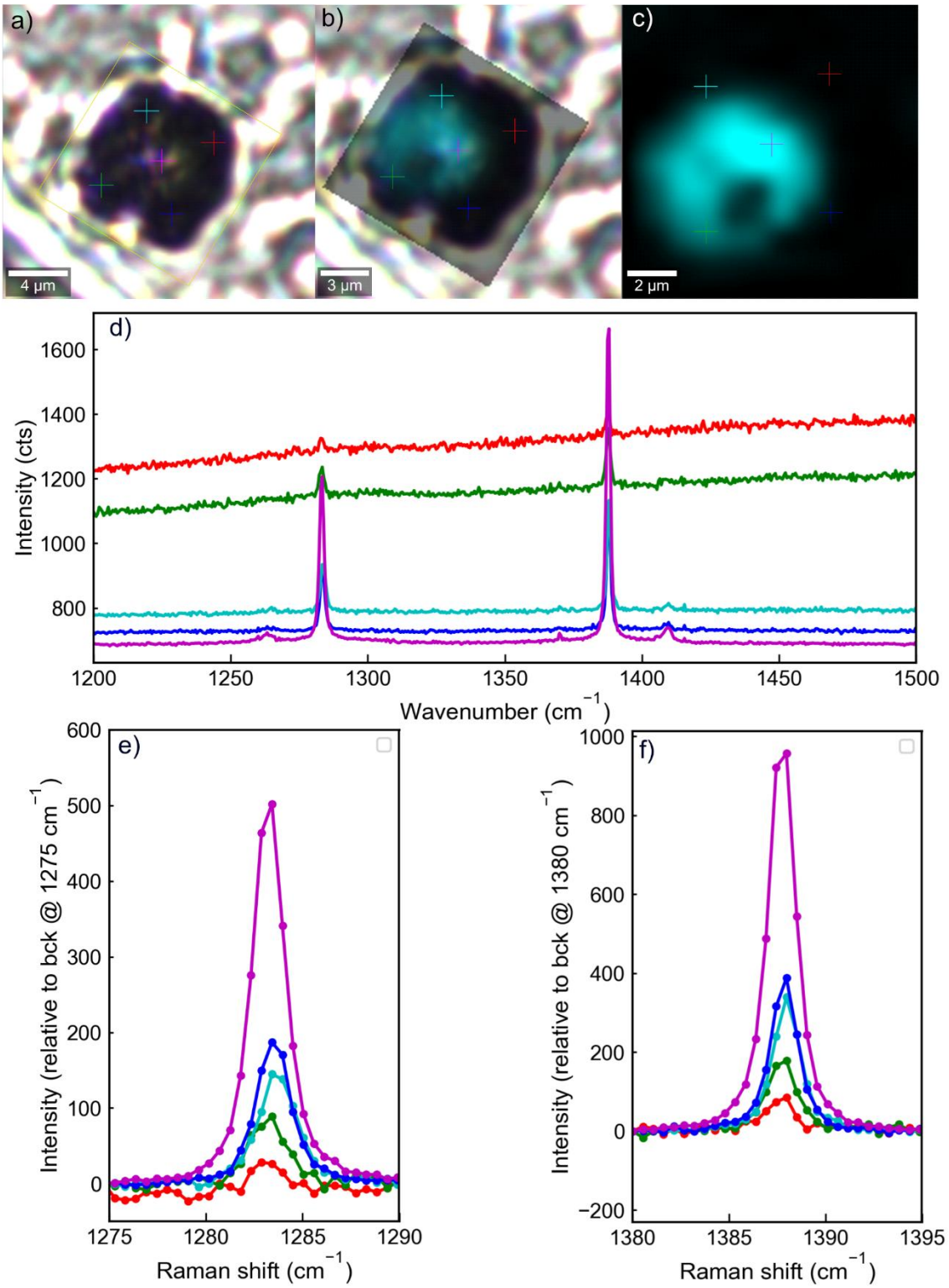

Supporting Figure 22 – Variation in signal intensity as a function of X-Y position within the fluid inclusion. a) Transmitted light image of fluid inclusion B23_FI5. The 5 colored crosses show the position of different spectral acquisitions shown in d-f. b) An 1800 g grating Raman map with the

intensity of the CO_2 signal shown as cyan colors overlain on this transmitted light image. c) shows the map with no underlay. d-f) Comparing the intensity of different acquisitions. While it is not surprising that the strongest signal is obtained from the center of the inclusion, it is surprising that despite the cyan, red, green and blue cross being equidistance from the center, they yield vastly different intensities.

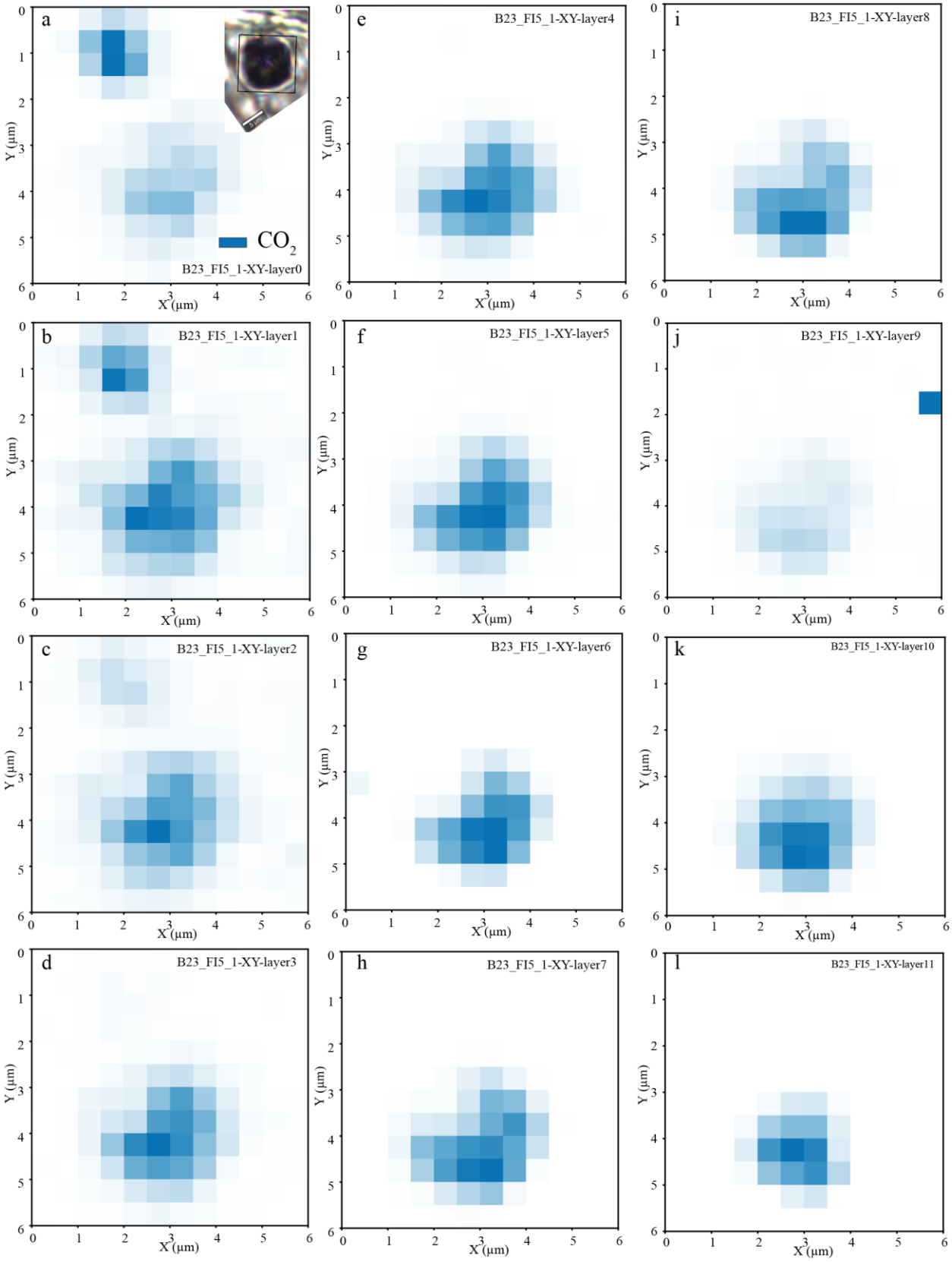
a
B23_FI5_1-XY-layer0
CO2
b
B23_FI5_1-XY-layer1
c
B23_FI5_1-XY-layer2
d
B23_FI5_1-XY-layer3
e
B23_FI5_1-XY-layer4
f
B23_FI5_1-XY-layer5
g
B23_FI5_1-XY-layer6
h
B23_FI5_1-XY-layer7
i
B23_FI5_1-XY-layer8
j
B23_FI5_1-XY-layer9
k
B23_FI5_1-XY-layer10
l
B23_FI5_1-XY-layer11
X (μm)
Y (μm)

Supporting Figure 23 – Raman map of CO_2 abundance in B23_FI5_1. The inset in a) shows the geometry of the map relative to the fluid inclusion. Each X-Y graph shows a different Z slice through the inclusion, with the stronger blue colors showing stronger CO_2 intensities. It is clear that the x-y positoin of max intensity varies with depth. The map geometry in the WITec software was set as 12x12x12 um, so each slice was separated by 1 um of stage movement. With the refractive index of olivine being 1.7 and CO_2 being 1, there is some vertical distortion. Maps were collected using 50X objective, with a laser power of 49 mW, an integration time of 1 s, the 1800 grooves/mm grating (so olivine is not visible), and a 1325 cm-1 spectral center. Processing was performed using Ramanspy 0.2.10 (Georgiev et al., 2024). To produce the maps, we first denoise using savitzky golay filter with a window length of 4, and a polynomial of 3rd order, then apply ASLS baseline routine and normalize each spectrum to using Min-Max normalization. We apply the whole preprocessing routine to all the maps. We extract "pure" endmember spectra for CO_2 from the map spectra and use Non-negative Constrained Least Squares (NNLS) abundance method in RamanSpy to extract abundance maps for CO_2 at every pixel. These maps are not quantitative, but an approximation of the distribution of CO_2. Each individual map is normalized to the strongest pixel within that slice.

References

Bearden, A.T., Wieser, P.E., Rangel, B., DeVitre, C.L., Gleeson, M.L.M., Monteleone, B.D., Lynn, K.J., 2025. Volatile systematics and magma storage depths at Mauna Loa: a melt inclusion perspective., in: In Chapman Conference on Caldera-Forming Eruptions at Basaltic Volcanoes: Insights and Puzzles from Kīlauea and Beyond. AGU.

Georgiev, D., Pedersen, S.V., Xie, R., Fernández-Galiana, Á., Stevens, M.M., Barahona, M., 2024. RamanSPy: An Open-Source Python Package for Integrative Raman Spectroscopy Data Analysis. Anal. Chem. 96, 8492–8500. https://doi.org/10.1021/acs.analchem.4c00383

Gleeson, M., Wieser, P.E., DeVitre, C.L., Shi, S.C., Millet, M.-A., Muir, D.D., Stock, M.J., Lissenberg, J., 2025. Persistent High-Pressure Magma Storage beneath a Near-Ridge Ocean Island Volcano (Isla Floreana, Galápagos). Journal of Petrology 66, egaf031. https://doi.org/10.1093/petrology/egaf031

Hagiwara, Y., Yoshida, K., Yoneda, A., Torimoto, J., Yamamoto, J., 2021. Experimental variable effects on laser heating of inclusions during Raman spectroscopic analysis. Chemical Geology 559, 119928. https://doi.org/10.1016/j.chemgeo.2020.119928